2016

Building a novel nanofabrication system using MEMS

https://hdl.handle.net/2144/19737

BOSTON UNIVERSITY

GRADUATE SCHOOL OF ARTS AND SCIENCES

Dissertation

BUILDING A NOVEL NANOFABRICATION SYSTEM USING MEMS

by

HAN HAN

B.S., Zhejiang University, 2010
M.A., Boston University, 2012

Submitted in partial fulfillment of the
requirements for the degree of
Doctor of Philosophy

2016

Approved by

First Reader

David J. Bishop, PhD
Professor of Physics
Professor of Electrical and Computer Engineering

Second Reader

David Campbell, PhD
Professor of Physics

Third Reader

Steve Ahlen, PhD
Professor of Physics

Acknowledgments

A PhD degree is not only an acknowledgement of one's knowledge or research achievement, but a milestone of one's personal growth in both academic and life experience. For me, I have learned a lot from people who have helped and supported me during the past six years. This is the most precious and invaluable treasure I got from the PhD journey.

First of all, I would like to thank my advisor Dr. David Bishop. He is a smart and knowledgeable physicist who can always give me professional suggestions every time when I face a challenge in my research. Good experiment results do not come out every time but he was always able to guide me through difficulties with workarounds and new ideas. As an advisor, he encouraged me to present my work in top conferences which increased the visibility of my research and offered me great opportunities to communicate with other researchers. I am grateful that Dr. David Bishop taught me a lot, not only the knowledge, but also how to become a successful researcher. I would like to thank Matthias Imboden, who was a senior colleague in Bishop's lab. He offered a lot of help when I joined the lab and taught me tons of experiment skills and techniques. We had collaborations throughout my PhD research and he helped me with many novel ideas for both device design and experiments. I also would like to thank other lab colleagues Pablo Del Corro, Jackson Chang, Tom Stark, Richard Lally, Jessica Morrison and Corey Pollock for helpful discussions and support they gave to me. I would like to thank Mirtha Cabello who helped me in administrating my PhD procedure and offered suggestions for the study and life in Boston. Finally I would like to thank my dissertation committee members: Shyamsunder Erramilli, Steven Ahlen, David Campbell and Pankaj Mehta for their advises. A special thank goes to Steven Ahlen who offered me many supports and research opportunities during the early stage of my PhD study.

There were difficult moments during the past six years but I was able to overcome them with the love and encouragement from my parents and my girlfriend, Lijun Peng. They gave me endless emotional support. Thanks also go to my friends Junwei Zhang, Zheyin Zhao, Shuai Shao, Kun Geng, Jiang Li and Xin Yuan. I am grateful to have them in my life.

BUILDING A NOVEL NANOFABRICATION SYSTEM USING MEMS

HAN HAN

Boston University Graduate School of Arts and Sciences, 2016

Major Professor: David J. Bishop, PhD
Professor of Physics
Professor of Electrical and Computer Engineering

ABSTRACT

Micro-electromechanical systems (MEMS) are electrically controlled micro-machines which have been widely used in both industrial applications and scientific research. This technology allows us to use macro-machines to build micro-machines (MEMS) and then use micro-machines to fabricate even smaller structures, namely nanostructures. In this thesis, the concept of Fab on a Chip will be discussed where we construct a palette of MEMS-based micron scale tools including lithography tools, novel atomic deposition sources, atomic mass sensors, thermometers, heaters, shutters and interconnect technologies that allow us to precisely fabricate nanoscale structures and conduct *in-situ* measurements using these micron scale devices. Such MEMS devices form a novel microscopic nanofabrication system that can be integrated into a single silicon chip. Due to the small dimension of MEMS, fabrication specifications including heat generation, patterning resolution and film deposition precision outperform traditional fabrication in many ways. It will be shown that one gains many advantages by doing nano-lithography and physical vapor deposition at the micron scale. As an application, I will showcase the power of the technique by discussing

how we use Fab on a Chip to conduct quench condensation of superconducting Pb thin films where we are able to gently place atoms upon a surface, creating a uniform, disordered amorphous film and precisely tune the superconducting properties. This shows how the new set of techniques for nanofabrication will open up an unexplored regime for the study of the physics of devices and structures with small numbers of atoms.

Contents

List of Tables

List of Figures

List of Abbreviations

AFM	....	Atomic Force Microscopy
ALD	....	Atomic Layer Deposition
CPD	....	Critical Point Drying
DIC	....	Digital Imaging Correlation
DIP	....	Dual In-line Package
DRIE	....	Deep Reactive-Ion Etching
FIB	....	Focused Ion Beam
HF	....	Hydrofluoric Acid
HOPG	....	Highly Oriented Pyrolytic Graphite
LCC	....	Leadless Chip Carrier
LPCVD	....	Low Pressure Chemical Vapor Deposition
MEMS	....	Micro-electromechanical Systems
NEMS	....	Nano-electromechanical Systems
PVD	....	Physical Vapor Deposition
PWM	....	Pulse Width Modulation
SEM	....	Scanning Electron Microscopy
STM	....	Scanning Tunneling Microscopy
TEM	....	Transmission Electron Microscopy

Chapter 1

Introduction and Motivation

1.1 MEMS and PolyMUMPs process

Micro-electromechanical systems (MEMS) are electrically controlled micro-machines which have been widely used in both industrial applications and scientific research(Bishop et al., 2012). As the name suggests, MEMS usually have mechanical components which can interact with the physical world, so that they are commonly used as sensors and actuators. This interaction usually involves the conversion of energy among different forms. Generally, MEMS are operated in one or more actuation modes, including electrostatic, piezoelectric, thermal, and magnetic actuation(Bell et al., 2005). Their applications range from sensors including MEMS pressure sensors(Eaton and Smith, 1997) and MEMS accelerometers(Tanaka, 2007) in automobiles and smartphones, to lab-on-a-chip devices in biological applications, and digital light projection systems in new display technologies(Bogue, 2007). Due to the miniature sizes, MEMS exhibit very high sensitivity and resolution when acting as sensors, and very high precision of control when acting as actuators. This makes MEMS powerful tools for researching and investigating microscale and nanoscale systems, which are usually difficult to probe and operate using macroscopic devices. For example, MEMS torsional resonator has been used to probe Casimir force which is too weak to be sensed at macroscopic scale(Chan et al., 2001), and MEMS mass sensors have been developed for mass detection down to the femtogram range(Villarroya et al., 2006), demonstrating how MEMS can help physicists to conduct research on microscopic systems.

The manufacturing of MEMS devices takes advantages of typical semiconductor fabrication techniques. The most important process of fabricating MEMS devices is photolithography(Judy, 2001), which is illustrated in Figure 1·1. In this process, typically, a polymer called photoresist that is sensitive to light exposure is used for patterning the micro-structure. At the beginning, the photoresist is uniformly spun onto the wafer to form a thin layer, as shown in Figure 1·1 a) and b). Then a transparent mask with pre-defined opaque pattern covers the photoresist so that the opaque pattern shelters the photoresist from being exposed to the light (Figure 1·1 c)). In Figure 1·1 d), the wafer with the mask is then exposed to ultraviolet light which can alter the properties of the photoresist. Therefore, the chemical properties of the photoresist that has been exposed to the ultraviolet light under the transparent mask will be very different to the region underneath the opaque pattern (Figure 1·1 e)). Next, the wafer is immersed into a chemical solution called developer, which can selectively dissolve the exposed region or the unexposed region, depending on which photoresist-developer combination is used (Figure 1·1 f)). After this process, a photoresist pattern is obtained and can be further used to pattern layers of other material for actual interests. Desired material is deposited on the patterned photoresist (Figure 1·1 g)). The material and the substrate will make direct contact along the pattern, but are separated by the photoresist outside the pattern. A final photoresist removal step will leave the material intact inside the pre-defined pattern and strip off the photoresist as well as the material on top of it (Figure 1·1 h)). More complex and multi-layer structures can be fabricated using the same idea but more step and repeat, in which photoresist is usually used as the sacrificial layer. Using photolithography, one can fabricate structures with a resolution down to tens of nanometers(Grigorescu and Hagen, 2009)(Sundaramurthy et al., 2006). For higher resolution, electron-beam lithography is a common choice(Liu et al., 2002). Micro-fabrication techniques including evaporation, sputtering, wet etching, reactive-ion etching and deep reactive-ion etching (DRIE), etc(Judy, 2001), are commonly found in the manufacturing process of MEMS.

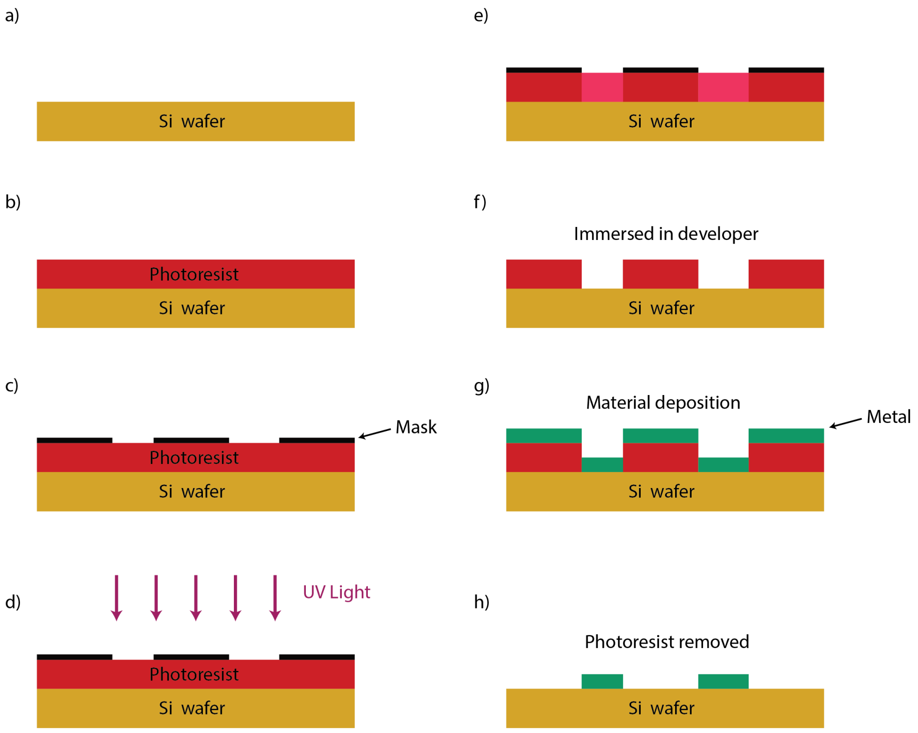

Figure 1·1: Steps of the photolithography process. a) A wafer is used as the substrate for fabrication. b) Photoresist is spun onto the substrate to form a uniform thin layer. The thickness is controlled by adjusting the spin speed of the spinner. c) A mask with desired pattern is put on top of the photoresist. d) The wafer is exposed to UV light. e) The region of photoresist which has been exposed to UV light will have altered chemical properties. f) The mask is removed and the developer dissolves the photoresist that has been exposed. g) Further material deposition follows a same pattern as the developed photoresist. h) A final photoresist removal procedure leaves the desired material in the desired pattern.

Traditionally, design, manufacturing, characterization and application of MEMS devices are carried out sequentially in the same lab or facility, while the recent development of MEMS industry has seen a trend of going fabless. This is a concept that the manufacturing of MEMS devices is separated and outsourced to a specialized manufacturer called a foundry. The fabless manufacturing has several advantages. First of all, the manufacturing of MEMS usually involves many processes and equipment which require extensive labor for operation and maintenance. A high end semiconductor production line is very expensive that small companies and research labs can hardly afford. Outsourcing the manufacturing to a foundry can solve this problem. Secondly, the nature of MEMS fabrication indicates that volume production can effectively reduce the cost. Therefore fabricating multiple users' designs altogether is very economic. Last but not least, by outsourcing the manufacturing, researchers can concentrate on design and characterization, but do not need to worry about the production of the MEMS device itself. The foundry will concentrate on ensuring the quality and reproducibility of the MEMS device and deliver very robust devices to the customer. The disadvantage of having a foundry to manufacture MEMS is that the specific process and technology to apply is not very flexible, especially for multi-user MEMS process. But for researchers, this problem can be somehow overcome by designing carefully and conducting additional post-processing.

PolyMUMPs by MEMSCAP is a widely used MEMS foundry service(Cowen et al., 2011). MUMPs stands for Multi-User MEMS Processes. This service is a surface micromachining process consisting of three layers of polysilicon separated by two sacrificial layers of silicon oxide, on a n-type (100) silicon wafer. An additional metal layer is also available as the final layer. Customers design the pattern of each layer in a layout designing software for a 1 cm by 1 cm area and submit the design file to MEMSCAP for manufacturing. Multiple 1 cm^2 squares from different customers are put together and manufactured on the same wafer, undergoing same processes. Each layer is patterned using photolithography and fabricated layer by layer to compose the complete device. Multiple identical copies of wafers are manufactured together so that each customer gets multiple identical copies of their devices, to accommodate the needs for prototyping and testing. PolyMUMPs is a highly reliable process that specifications and physical properties of a same micro-structure design see very little variation among different runs of the process, ensuring customers to characterize their devices and improve their designs run by run without the interference of manufacturing quality fluctuation. This process allows for rapid cycle times (∼2 months), and because multiple users share the same wafer, the process is very cost-effective.(Imboden et al., 2014a) This means that it is feasible for researchers to submit multiple devices for each consecutive run, to actively improve their devices and conduct new experiments at a fast pace using trial-and-error methods.

The PolyMUMPs process starts with 150 mm n-type (100) silicon wafers which has a heavily phosphorus doped surface. A 600 nm silicon nitride layer is deposited on the wafer as an electrical isolation layer before the subsequent functional layers. The first layer of polysilicon (POLY0) is then patterned and deposited with a thickness of 500 nm. This is a static layer because it is directly attached to the silicon nitride substrate. One oxide sacrificial layer (OXIDE1, 2000 nm), one polysilicon layer (POLY1, 2000 nm), another oxide sacrificial layer (OXIDE2, 750 nm) and another polysilicon layer (POLY2, 1500 nm) are then deposited subsequently. A final metal layer (METAL) consisting of gold and a thin adhesion layer is then deposited for bonding, electrical connection, thermal actuation, etc. Several abstract layers are used at the design time, for defining the pattern of the additional layer modification steps on the actual layers. For example, ANCHOR1 and ANCHOR2 are used to create openings on OXIDE1 and OXIDE2 all the way down to POLY0 or the nitride layer, so that POLY1 and POLY2 can come down and make direct contact to the substrate at the

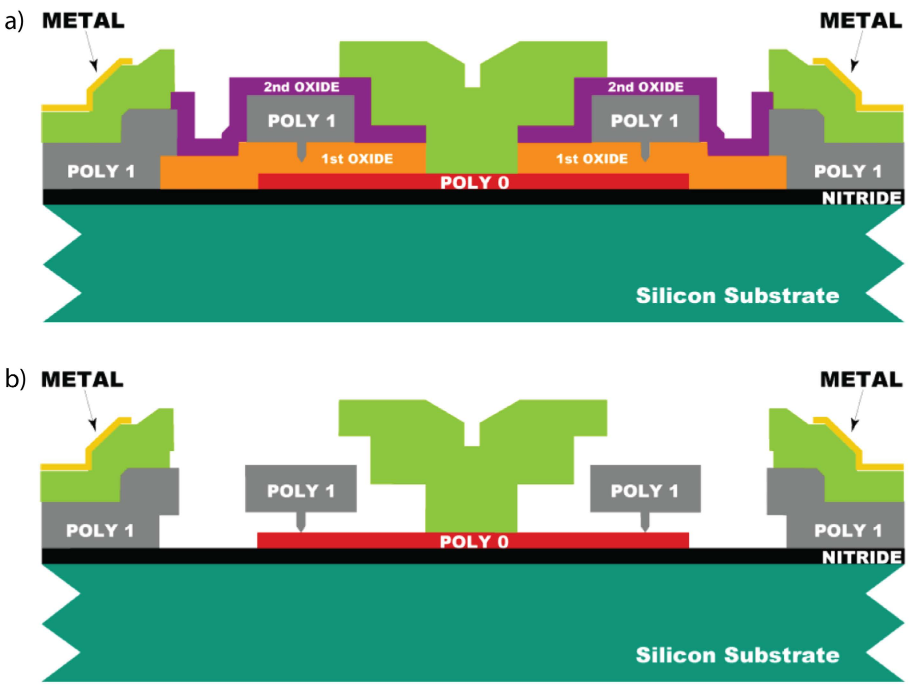

Figure 1·2: Excerpted from the PolyMUMPs design handbook(Cowen et al., 2011), the diagram showing a cross-section view of a MEMS rotor before and after the HF release illustrates layers of the PolyMUMPs process. After the HF release, in b), the movable rotor structure is fully suspended with small post to prevent stiction. This figure is not drawn to scale.

desired location. DIMPLE is used to thin OXIDE1 750 nm so that the POLY1 or POLY2 can have a small 750 nm deep dent within the DIMPLE area to act as a standoff. P1_P2_VIA is used to etch away OXIDE2 so that POLY2 can make contact to POLY1. With the help of these additional steps, many device designs are made possible. After the manufacturing is done, a protective photoresist layer is spun onto the device before shipping out to the customer, to protect it from scratch and other possible damages. The customer conducts a final wet etch step using hydrofluoric acid (HF) to dissolve the oxide sacrificial layer so that the device gets released and the movable polysilicon layers are completely freed and suspended. A critical point drying (CPD) process after HF release is usually necessary to reduce the stiction between surfaces. Such a surface micromachining process has a minimum feature size of around 2 µm. More details of the PolyMUMPs process can be found in the design handbook(Cowen et al., 2011). Figure 1·2 shows a diagram of a MEMS rotor before and after the HF release step. The cross-section view gives an idea of how the entire structure is organized using the layers and steps described above. The HF release step removes oxide in the device to set free the suspended structures as shown in Figure 1·2 b).

As the foundry process provides an affordable way for fast development of highly reproducible devices, we chose to use this process to manufacture the MEMS device for our research and experiments, on which this thesis focuses. Therefore we can concentrate on implementing the functionality of the device and conducting experiments using the device, but not bothered by the subtle and complicated manufacturing process. It will be shown throughout this thesis that we gain a lot of advantages by having a foundry to perform the fabrication.

1.2 Fab on a Chip: a new approach for nanofabrication

MEMS being manufactured in a macroscopic fab inspires the idea of getting the process further down to fabricate even smaller structures, namely nanostructures or nano-electromechanical systems (NEMS), using MEMS. Typically, several essential components form a conventional fab, including the material source, the deposition target, the patterning tool and sensing techniques to monitor the progress of the deposition. For example, a common way to fabricate metal micro-structures is to use the thermal evaporator, in which metal is heated and evaporated from a coil by Joule heating and condenses on the target wafer which stays cool. Photolithography is the typical patterning tool in this case hence the wafer is covered with patterned photoresist. The thermal evaporator has a crystal thickness monitor beside the wafer holder to measure the thickness of the film being deposited, so that the rate and thickness of the deposition is controlled. Such technologies can provide a high resolution and precision for fabricating structures in the micron and sub-micron regime. However, as the desired structure dimensions continue to shrink from the deep sub-micron regime into the nanometer regime, standard techniques to manufacture the devices are becoming increasingly challenging(Grigorescu and Hagen, 2009)(Ito and Okazaki, 2000). Another problem of traditional fabrication techniques is that they usually requires a final lift-off step that removes the sacrificial photoresist layer to complete the desired structure. This imposes difficulties for *in-situ* fabrication, which is required when the experiments on the nanostructure has to be performed while the fabrication is in progress or right after the fabrication is done. This is important for superconducting thin film experiments when the resistivity of the thin film needs to be measured as the film thickness increases gradually at a low temperature(Ekinci and Valles, 1999). However there are ways including stencil lithography(Vazquez-Mena et al., 2014)(Deshmukh et al., 1999) which uses a stencil mask as the patterning tool to get rid of the final lift-off step so that the evaporated material passes through the mask to deposit on the target in the designed pattern. Hence, a high precision, final step fabrication system is of great interest for nanoscale systems research.

The principle and limitation of conventional fabs inspired a different approach, Fab on a Chip, a technique of directly depositing structures with atomic flux using small numbers of atoms under the control of several MEMS devices.(Imboden et al., 2014a) The idea behind Fab on a Chip is to use a system of systems approach where we take all of the elements of an evaporation system and ultimately integrate them onto a single silicon chip. In other words, we use macro machines to build micro machines and then use these micro machines to further manufacture nanostructures.

Due to the small dimension of MEMS, fabrication specifications including patterning resolution and film deposition precision outperform the traditional fab in many ways. Integrating the fab into a chip also means fabrication, characterization and experiment can be performed together *in-situ*, which is crucial for many condensed matter physics experiments. To achieve that, the MEMS version of those essential fab components have been developed. We've built patterning tools, novel atomic deposition sources, atomic mass sensors, thermometers, heaters, shutters and interconnect technologies. By assembling these micromachines together into a single chip or two, one can build a Fab on a Chip that can fabricate nanostructures for a variety of applications with unprecedented versatility, precision and convenience.

For the patterning tool, we developed a MEMS device for resist-free nanostructure patterning. The idea was inspired by stencil lithography in which atoms pass through openings in a shadow mask to form a pattern. In our design, a polysilicon plate with through holes was positioned and controlled precisely on a 2D plane by MEMS linear motors and suspension springs.(Imboden et al., 2013) This device called a MEMS writer implements the principle of dynamic stencil lithography. The writer plate acts as an ink-jet printing head — evaporated atoms pass through apertures on the plate and deposit on the substrate to form patterned structures by having the writer plate move in a pre-defined trace. The line width resolution of the nanostructure is determined by the size of the aperture, which is drilled using Focused Ion Beam (FIB). The MEMS linear motor covers a long working range of tens of micrometers, but still offers a resolution of sub-nanometers, thanks to the voltage square dependency of actuation. The writer provides a way to fabricate nanostructure precisely using just one deposition step without the need of a lift-off step, enabling measurements and experiments on the structure to be performed right *in-situ*.

A central component of any fabrication setup is the deposition control of the materials to be used. In Fab on a Chip, we designed a MEMS based, multi-material evaporation source array with each source element consisting of a polysilicon plate suspended by two electrical constriction leads.(Han et al., 2015) When resistively heating the plate, the pre-loaded material is thermally evaporated off of the plate. By arranging many of these devices into an array, one has a multi-material, digitally programmable evaporation source. Pulsing the source with precisely controlled peak voltage and timing can emit atom fluxes with an unprecedented level of control in terms of what, when and how many atoms get deposited. By varying their dimensions and arrangement, the source array can provide controllable atom fluxes ranging over ten orders of magnitude, on a target roughly 1 mm away from the surface. Such a material source can provide precise control and flexibility when conducting nanofabrication, either with or without the patterning using MEMS writer. We also show that because of the miniature size of the source, the power consumption and heat generation of the source is greatly depressed so that it is fully compatible with cryostation to conduct nanoscale quench condensation at cryogenic temperatures.

Other MEMS components of Fab on a Chip have been developed to better support the fabrication process and accommodate experiment needs. A MEMS mass sensor which is essentially a parallel plate oscillator with one suspended plate has been implemented. When incident atoms deposit on the suspended plate, the mass change of the plate can be measured by detecting the resonant frequency shift.(Imboden et al., 2014a) Such a mass sensor has a resolution of sub-femtograms and can be used as a high-precision thickness monitor when conducting nanofabrication. Because it is manufactured using the same PolyMUMPs process as other components of Fab on a Chip, it can be integrated right beside the writer to monitor the fabrication, or used solely with the MEMS evaporation source when a writer is not needed. We have also developed a MEMS shutter which is typically placed above the writer plate to selectively open and close the apertures used for patterning. Thermometers, heaters, interconnect technologies and deposition target geometries for different applications have been designed and tested to offer a great flexibility for a large range of fabrication requirements.

This thesis will demonstrate all of the functioning elements needed to allow us to create microscale factories for producing single or arrays of nanoscale devices. Parts of the work and results discussed in this thesis have been published in (Imboden et al., 2013), (Imboden et al., 2014b), (Imboden et al., 2014a) and (Han et al., 2015). By having all fab components in a single silicon chip, one can conveniently conduct final-step *in-situ* nanofabrication with high resolution. Due to the nature of how the deposition is performed, each Fab on a Chip is disposable, requiring high reproducibility and cost efficiency which are achieved by having the PolyMUMPs foundry process manufacture the entire micro fab. Fab on a Chip provides an all-in-one solution for nanofabrication without the requirement for users to have profound experience with lithography. The nanostructure is designed with the aid of a computer which controls the whole process and even the subsequent experiments automatically, making the fabrication process easily accessible by general researchers. We believe that such Fabs on a Chip may be a viable technique for both prototyping and large scale nanomanufacturing.

1.3 Quench-condensation of superconducting thin films

Quench-condensed systems are of great interest for condensed matter physics research. Materials being quench condensed usually exhibit different properties than conventionally deposited materials. This is because that when the material particles reach the deposition substrate, thermal energy plays an important role in the formation of the film. Besides the substrate temperature, the material of the substrate can also affect the morphology of the deposited film, thus the transport properties. For example, lead quench condensed on a passivated substrate usually forms disconnected islands with diameters of $10\,\mathrm{nm} - 20\,\mathrm{nm}$ (Ekinci and Valles, 1999) (Frydman and Dynes, 2001). Electrons travel inside each metallic grain and tunnel among different grains. For such a film, the measured resistance of the film is correlated to the quantum tunneling effect which is greatly influenced by the average gap size among grains. Therefore when more material is getting deposited, the average distance between nearby grains will decrease, resulting in a transition from insulating state to superconducting state if the temperature stays below the critical temperature. It has been shown (Frydman, 2003) that the use of a germanium (Ge) under-layer can cause an increased uniformity of the film. However, without the use of a special under-layer, quench-condensation of metal on common passivated substrates usually yields granular films (Ekinci and Valles, 1999), which is not desired for superconducting thin film research.

The traditional deposition methods for such a quench-condensation involves the use of liquid helium (He) bath to maintain the ultra-low temperature (Frydman et al., 2002)(Strongin et al., 1970). A He dewar is usually used to hold the liquid He and the deposition chamber is inserted into the dewar so that it can be cooled down to only a few Kelvins. Thermal evaporation is conducted inside the chamber. Material is evaporated from a heated metal coil and get quench condensed onto the cold target, which usually has pre-deposited electrodes for resistivity measurement. Basically a smaller version of the thermal evaporator is built inside the He dewar. However, such a setup usually uses a macroscopic material source which has several disadvantages. The first one is the heating issue. In order to evaporate metal, a very high temperature is often required. Such a high temperature obtained on the macroscopic source means that a large amount of heat has to be generated inside a He dewar, requiring a careful design for heat dissipation and precautions when operating the evaporator. Otherwise an explosion may occur if too much heat is absorbed by the liquid helium and the vaporization of helium causes over-pressure in the dewar. Besides the safety concern, another disadvantage of using the traditional source is that the evaporation flux cannot be precisely controlled and timed. I will show in this thesis that a MEMS-based micro evaporation source is developed for quench condensing ultra-thin superconducting film and it outperforms the traditional deposition methods in many aspects.

Using the concept of Fab on a Chip, we built a MEMS-based micro evaporation system that is compatible with a cryogenic environment to conduct quench condensation, for superconducting thin film fabrication and *in-situ* measurement. Such a system has both material sources and deposition target integrated together as a single device. Its miniature size enables it to work inside a cryostation with little heat generation. I will show in chapter 4 that the micro sources can emit precisely controllable atomic flux which is detected by mass sensors discussed in chapter 3. Hence the thickness of the superconducting thin film is precisely determined. The detail of such a quench-condensation process, as well as the *in-situ* resistivity measurement done on the thin film for in-depth investigation of its superconducting properties, is presented in chapter 5. It is shown that due to the ultra-small amount of atoms emitted from the micro source each time, the thermal power of the incident atomic flux is significantly depressed so that the atom tends to stay still on the substrate. Therefore even without a special under-layer, a very uniform superconducting thin film is still obtained on the passivated substrate.

Chapter 2

Atomic Calligraphy: The Direct Writing of Nanostructures

2.1 Overview: A MEMS-based patterning tool

Conventional lithography usually adopts a top-down approach for patterning structures.(Biswas et al., 2012) In a top-down approach, material is deposited all over the substrate at the beginning and the patterned structure is obtained by etching away the undesired region with the help of a sacrificial substance. This approach has the difficulty when the number of atoms wanted in a device is reduced to the level of single or few atoms, that accurately leaving those atoms in the right location and removing the rest majority of atoms is becoming very challenging, especially for lithography.(Grigorescu and Hagen, 2009)(Ito and Okazaki, 2000) Another disadvantage of the top-down approach is that since etching is usually required before the final structure is completed, *in-situ* growth of the structure is always not feasible. *In-situ* addition and modification of nanostructures are often desired for research purposes when the physics involving growth progress itself is of interest(Puretzky et al., 2005).

Bottom-up fabrication approaches have been developed to overcome these difficulties, including Dip-Pen nanolithography which is based on using an atomic force microscopy (AFM) probe to flow liquid inks onto a substrate(Piner et al., 1999), and stencil lithography which allows patterned geometry to be imprinted through the stencil opening(Vazquez-Mena et al., 2014)(Deshmukh et al., 1999). Both of them are resist-free and do not need etchants to remove unwanted material. However the stencil method can not be used to pattern topologically complex structures such as rings or closed circuits with holes in it, because the stencil does not allow isolated islands, while the Dip-Pen method is limited by the types of compatible deposition materials and operation environments. The workaround is to place apertures or stencils on an AFM cantilever or another micropositioner and pattern by guiding the stencil like an ink-jet printing head during the deposition.(Champagne et al., 2003)(Savu et al., 2011) Hence a micro version of a 3D printer is built for resist-free construction of nanoscale 3D structures. As one can see, such a setup is always complex and requires supporting equipment such as an AFM, resulting in reduced feasibility and compatibility.

MEMS devices have shown their great robustness and reliability in many applications.(Tanner, 2009) They can operate in a wide range of conditions and their miniature size offers a high precision in control. MEMS based XY stages have been developed and investigated to provide a way to precisely position an object on the 2D plane(Sun et al., 2008)(Gorman et al., 2007), inspiring the idea of using this device to implement dynamic stencil printing, which allows for full patterning control of the amount and location of a desired material. Such a device called a MEMS writer is based on the MEMS XY stage with a central plate as the writing plate which has milled apertures on it, as shown in Figure 2·1.(Imboden et al., 2013) By putting the device in the rain of evaporated atoms inside an evaporator, atoms pass through the apertures and deposit on the cool substrate underneath the plate. Moving the writing plate in a controlled trace while maintaining the atomic flux will then “draw” a nanostructure on the canvas. The positioning of the writing plate is realized by having four MEMS linear motors to pull it in each direction. The four linear motors configuration provides balanced and well-controlled positioning of the plate on a 2D plane. Using a relatively simple control circuit, electrostatic actuation allows for high displacement resolution and negligible power consumption. In order to make the plate move freely and controllably above the canvas, micro suspension springs suspend the plate and connect it with the motors. The size of the aperture which is fabricated using FIB defines the line width of the patterned nanostructure. With the help of FIB, we can easily make such apertures with a diameter as small as 50 nm. A MEMS shutter can also be integrated on the chip above the writing plate, so that only selected apertures are exposed to the atom flux when the shutter is carefully actuated. This is useful for multi-step deposition that some apertures can be saved for future steps. Featuring an open-closed cycle of $\sim 100\,\mu s$ period, the shutter is also able to control stochastically very small amount of atoms, down to of order one, to be deposited through the aperture. This technology called Atomic Calligraphy encapsulates the entire patterning tool and deposition target into single silicon chip, making nanofabrication achievable and compatible with various environments and requirements. This single use device is manufactured at low cost using the PolyMUMPs foundry process in a scalable way, enabling high flexibility and turnover. Since the writer device is simple to operate and inexpensive, nonexperts can rapidly fabricate their nanoscale devices to study novel materials or NEMS structures. Using an industry standard foundry also means that different MEMS sensors and actuators can be assembled to the MEMS writer seamlessly, providing a flexible way to extend the functionality of this fabrication tool.

In this chapter, I will discuss the development and characterization of each component of Atomic Calligraphy in detail, including the MEMS linear motor, the writing plate and the shutter. The functionality of each part is carefully investigated to assemble the MEMS writer. To demonstrate its versatility and flexibility, various nanostructures have been fabricated. It will be shown that the writer is capable

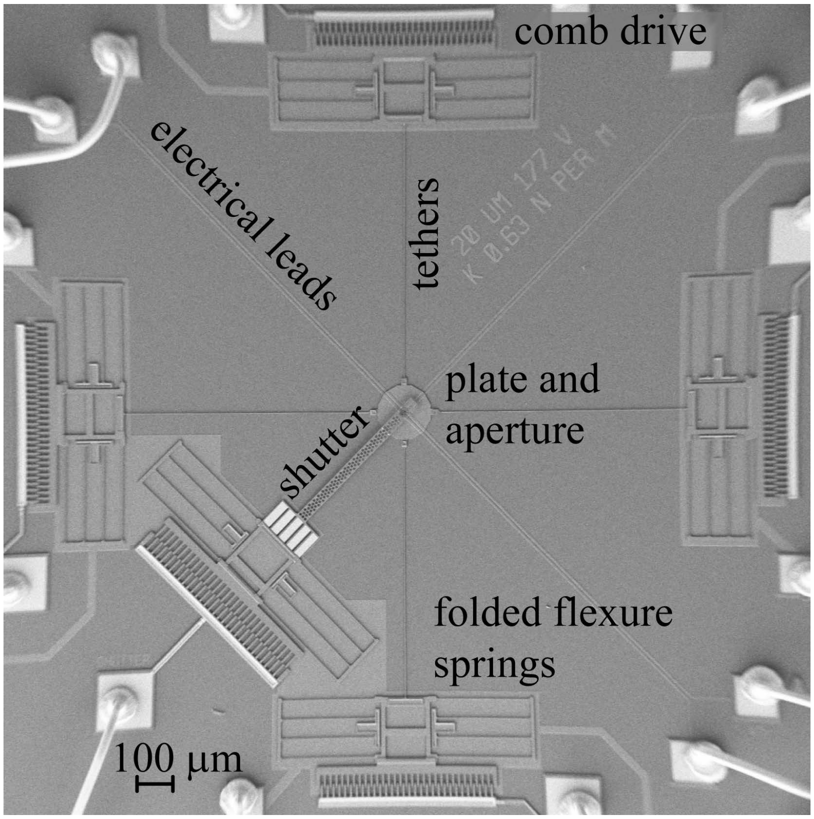

Figure 2·1: The scanning electron microscopic (SEM) image of an Atomic Calligraphy writer device. The core component of this device is a thin silicon plate suspended by four tethers connected to four MEMS linear motors based on comb drive actuator, which can position the plate precisely above the substrate surface. Evaporated atoms pass through the aperture on the plate and deposit on the substrate to form a designed pattern. A shutter to select apertures is an optional component. Electrical leads provide access to the fabricated structure for electrical measurement purposes.

to directly write very fine NEMS with precise control and minimum post-processing requirement.

2.2 Device components

2.2.1 The linear motor: Comb drive actuator and folded spring

The MEMS linear motor used in Atomic Calligraphy is based on capacitive comb drive, which is actuated using electrostatic force. This comb actuator has been widely used in various applications including gyroscopes(Leland, 2005), accelerometers(Lu et al., 1995)(Lakdawala and Fedder, 2004), magnetometers(Thompson et al., 2011), etc, due to its long actuation range, low power consumption and simple structure for fabrication a basic comb drive design only needs one movable layer of polysilicon to build. Capacitive electrostatic actuation means that it has a large linear response with the mechanical displacement and its power consumption is very low, because nearly zero current is flowing to dissipate energy. Sensing the displacement is also possible via measuring the capacity change of the device. Such a comb drive provides the driving force on the central writing plate of a MEMS writer.(Imboden et al., 2014b)

Figure 2·2 depicts the typical comb drive we use in the MEMS writer. It has two combs with the fingers inserting into each other alternatively with a small gap. The static comb is anchored to the substrate while the moving comb is suspended by a folded spring so that it can move towards or away from the static comb when a force is applied. The spring also helps to balance the pulling force to position the moving comb. Two combs form a capacitor and the finger design provides a nearly linear capacitance - displacement dependency. By applying a voltage across two combs, through the electrical leads, the electrostatic force will attract the moving comb towards the static comb. Hence anything attached to the moving comb can be positioned in the axis.

Micro polysilicon wires with the METAL layer run from the static comb to the

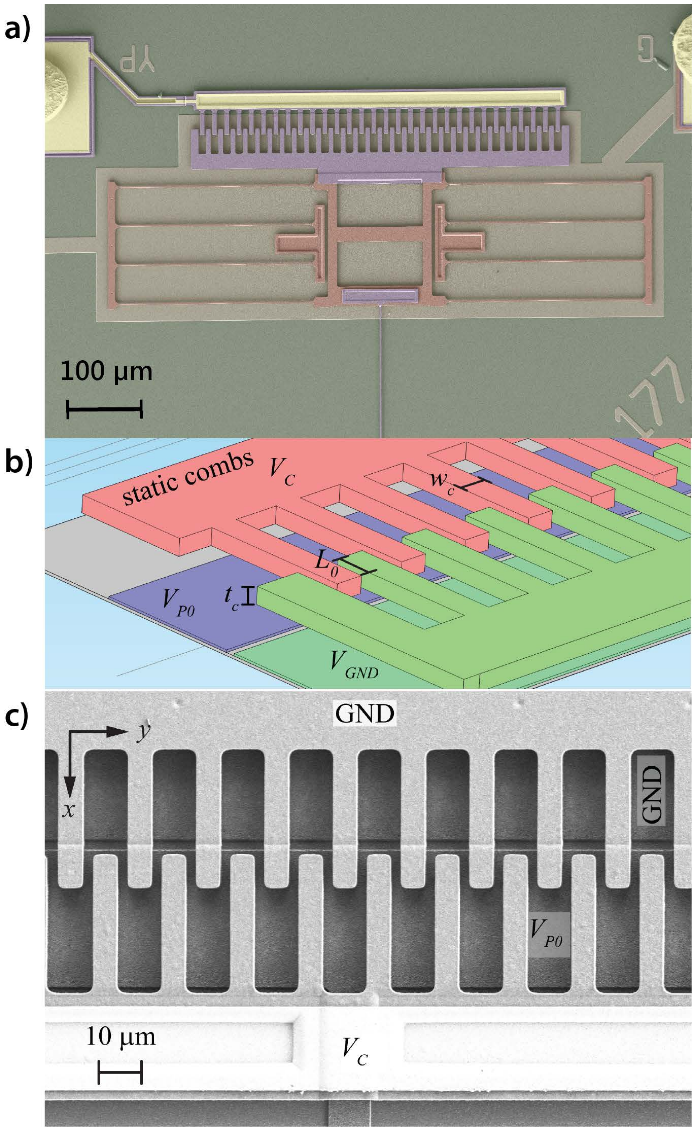

Figure 2·2: Shown is a typical comb drive actuator design for the MEMS writer. a) The false color SEM image shows the assembly of the comb drive, the suspension spring and tether. The comb structure and tether are built with POLY2 layer in PolyMUMPs process while the spring is made of POLY1 layer. b) The model of the comb fingers illustrates the configuration and how voltages are applied to different parts of the comb drive to actuate the device. c) A close-up SEM image of the comb fingers. It should be pointed out that the comb drive in a) has a slightly different design than the one in b) and c). The latter has an additional POLY0 charging plate underlying the static comb to compensate the levitation force on the moving comb.

bonding pad, while POLY0 wires connect the POLY0 underlay to another bonding pad, as shown in Figure 2·2 a). The POLY0 underlay is connected to the folded spring and then the moving comb through the anchor of the spring. This configuration provides electrical access to the comb drive actuator so that the actuation voltage can be applied through the bonding pads. We use a ball bonder to bond a thin gold wire from the pad to the ceramic package so that connections to external equipment are made.

The electrostatic energy stored in a capacitor can be expressed as $E = \frac{1}{2}C \cdot V^2$, where C is the capacitance of the capacitor and V is the voltage difference between the two electrodes of the capacitor. By taking the derivative, the electrostatic force between two electrodes can be expressed as

$$\overrightarrow{F} = \frac{1}{2}\overrightarrow{\nabla} C \cdot V^2. \tag{2.1}$$

For our comb drive as shown in Figure 2·3, the capacitance between two combs increases as the combs come closer. For now we only consider the motion along the x-axis, so the force can be expressed as

$$F_x = \frac{1}{2}\frac{\mathrm{d}C}{\mathrm{d}x}V^2 \approx \frac{\eta}{2}\frac{N\varepsilon_0 t_c}{g} \cdot V_c^2, \tag{2.2}$$

where η is a numerical factor characterizing the strength of the fringe capacitance and N is the number of combs. The representations of other symbols can be found in Figure 2·2 b) and Figure 2·3. For an ideal parallel plate capacitor where t and $L_0 \gg g$, η approaches 1. Here, $g \sim t$, and for this particular comb drive geometry $\eta \approx 2$.

This force will pull the moving comb towards the static comb along the x-axis and distort the folded spring. It is balanced by the restoration force from the spring as

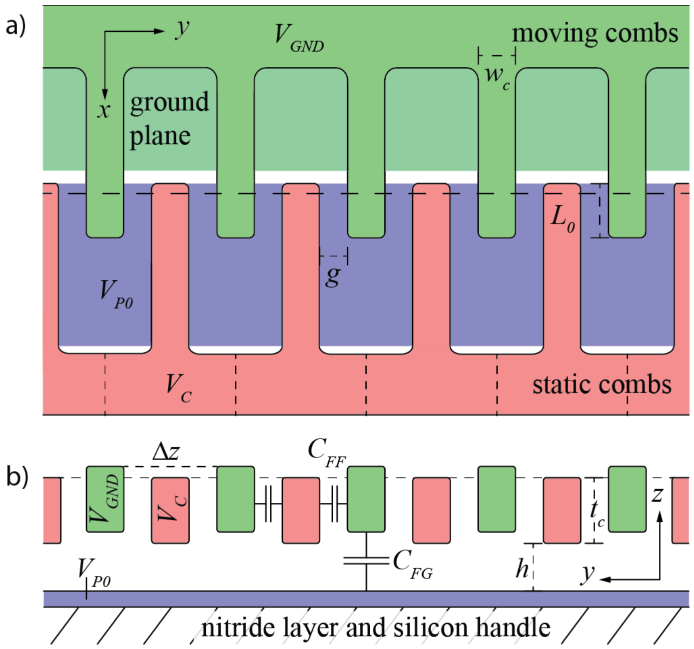

Figure 2·3: Diagram of the comb drive actuator. a) Top view of the static and moving combs. b) Slice of the cross section along the dotted line in a).

described by Hooke's law:

$$F_i = -k_i x_i, \tag{2.3}$$

where k_i is the spring constant of the spring system along the i^{th}-axis. Details on the calculation for the spring constant will be discussed later. Therefore, the ultimate comb displacement function is derived to be

$$x = \frac{1}{2k_x}\frac{\mathrm{d}C}{\mathrm{d}x}V^2 \approx \frac{\eta}{2k_x}\frac{N\varepsilon_0 t_c}{g} \cdot V_c^2. \tag{2.4}$$

Due to the geometry of the comb, the capacitance of the comb drive has a nearly linear relationship with the displacement, so that the derivative of the capacitance is constant. This ensures the V^2 dependency of the displacement. As we will elaborate in subsection 2.3.2, experiments have confirmed this assumption.

So far only in-plane motion of the comb has been discussed. However, it has been studied in (Tang et al., 1992) that the moving comb also experiences an out-of-plane motion in the z-axis, namely comb levitation, which is due to the induced charge on the giant substrate surface. As shown in Figure 2·3 b), the moving finger will be lifted a bit when a voltage is applied. By having an independent bottom electrode (the POLY0 electrode with a voltage V_{P0} shown in Figure 2·2 b)) to pull down the comb, one can control the levitation effect. Such configuration allows for controlled out-of-plane motion and can effectively repel a MEMS structure away from the substrate. However, since the moving comb moves out of the plane, the levitation will also weaken the electromagnetic coupling between the two combs, resulting in a reduced working range and stability. Applying a voltage on the pull down electrode depresses the levitation and increases the lateral operational range of the device. The detail about this technique is discussed in (Imboden et al., 2014b).

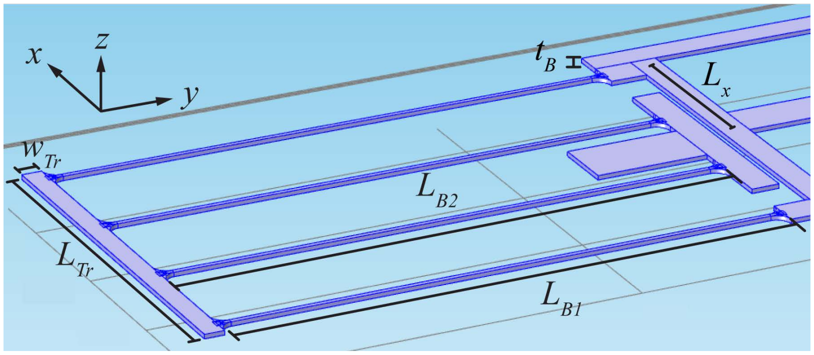

Figure 2·4: Diagram of half side of the doubly folded flexure spring with annotations.

The spring systems used to balance the driving force and suspend the writer plate are doubly folded flexure springs, as shown in Figure 2·4. The spring constant along x-axis for this device has been studied by Gary K. Fedder in his dissertation (Fedder, 1994). For our specific folded spring, the spring constant can be calculated as:

$$k_{foldedspring,x} = 2\frac{Et_B w_B^3}{L_B^3}\frac{L_{Tr}^2 + 14\alpha_m L_{Tr} L_B + 36\alpha_m L_B^2}{4L_{Tr}^2 + 41\alpha_m L_{Tr} L_B + 36\alpha_m L_B^2} \quad (2.5)$$

where w_B is the width of the long beam, $\alpha_m = (w_{Tr}/w_B)^3$ is the cube of the truss-beam width ratio, and $L_{B1} = L_{B2} = L_B$. Here we also assume that for small displacement the beam and truss length will stay constant. $E = 158$ GPa is the Young's modulus of polysilicon(Cowen et al., 2011). We have conducted finite element simulation for the x-axis deformation of this spring using COMSOL Multiphysics®Modeling Software and the result is shown in Figure 2·5.

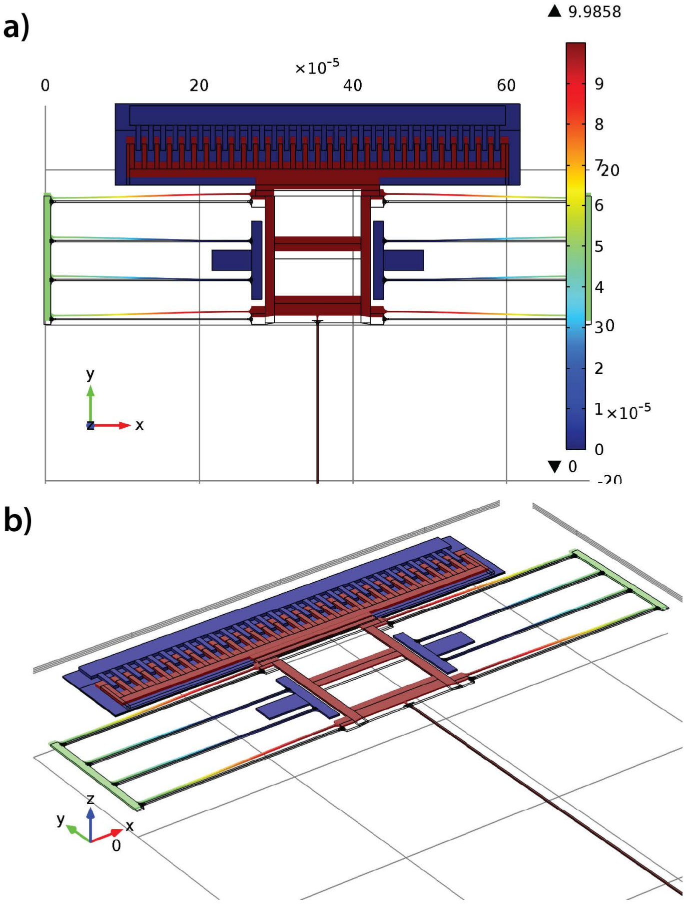

Figure 2·5: Simulation of the mechanical movement of the linear motor shows how the spring is deformed along x-axis during the actuation of the comb drive.

When a comb drive is actuated for a displacement of Δx, the direct adjacent spring will be deformed along x-axis by Δx, and the opposite spring across the writer plate will be deformed by $-\Delta x$. Two lateral tethers connected to the other two springs will also bend, contributing to the overall spring constant as well. Their tip will move laterally by Δx. The configuration is shown in Figure 2·6. Theoretically, other parts of the system including the writing plate, two tethers along the direction of motion and two lateral springs may also contribute to the overall spring constant. However, since they are extremely stiff along the direction of the assumed displacement, their contribution can be safely ignored. The overall spring constant can then be expressed as:

$$k_{total,x} = 2\left(k_{foldedspring,x} + k_{tether,x}\right) \tag{2.6}$$

where $k_{tether,x}$ is the spring constant for the tether to bend in order to accommodate the perpendicular displacement on one end. The spring constant for such a beam is given by:

$$k_{tether,x} = 12\frac{EI_{t,x}}{L_t^3} = \frac{Et_t w_t^3}{L_t^3} \tag{2.7}$$

where $I_{t,x}$ is the area moment of inertia of the cross section along x-axis, w_t and t_t are the width and thickness of the tether, respectively.

Table 2.1 lists the parameters of a typical writer device. By plugging in the number into the above formulas, we can obtain that:

$$k_{foldedspring,x} = 0.22\,\mathrm{N/m} \tag{2.8}$$

$$k_{tether,x} = 0.015\,\mathrm{N/m} \tag{2.9}$$

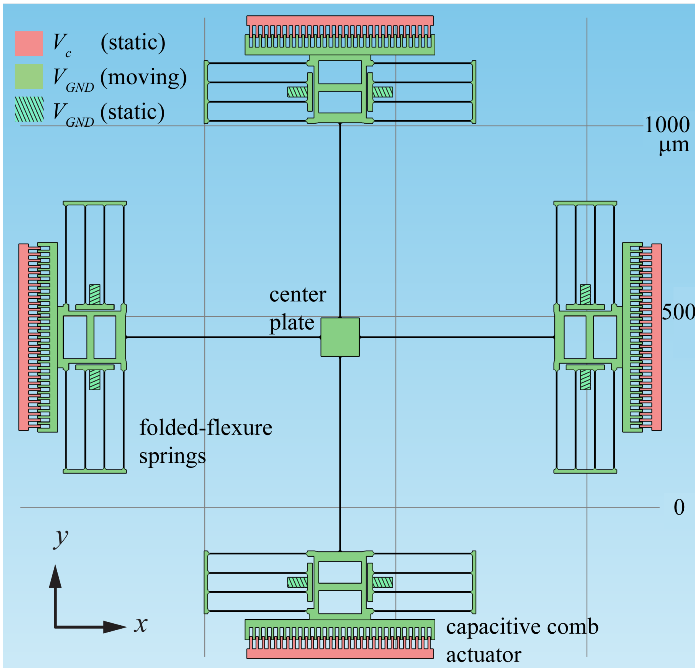

Figure 2·6: Diagram of the entire writer device. One direction of movement deforms two folded springs and two tethers.

$$k_{total,x} = 0.47\,\mathrm{N/m} \tag{2.10}$$

We found such numbers well in agreement with the simulation results.

The working range of the linear motor depends on several factors. The comb drive may collapse when two combs are inserting into each other too closely, due to the electrostatic pull-in effect. (Nadal-Guardia et al., 2002) The anchor of the folded spring will also block the spring from further deformation at some point. While longer working range usually requires more careful design and higher driving voltages which raise other problems, we found that $\sim 10\,\mu\mathrm{m}$ is easy to achieve but still covers ample area for nanofabrication.

2.2.2 The writing nib: Central writing plate

Suspended above the silicon nitride substrate, the writing plate made from either POLY1 or POLY2 layer is the central component of the device. The plate is pulled

Measure	Value	Unit
L_B	255	µm
L_{Tr}	164	µm
t_B	2	µm
w_B	2	µm
w_{Tr}	9	µm
L_t	508	µm
w_t	2	µm
t_t	1.5	µm

Table 2.1: Mechanical parameters of the folded spring and tether

by linear motors through tethers in four directions on the 2D plane, so that it can be precisely positioned. The similar design has been implemented as micro-positioner stages in other research (Sun et al., 2008) (Ji et al., 2010). For Atomic Calligraphy, the central writing plate works like an ink-jet printer head through apertures are milled on the plate and nanoscale pattern is obtained by continuously depositing atoms through the apertures, while moving the plate in a designed trace. The plate by design covers an area in the order of $\sim 100\,\mu\text{m}$ by $100\,\mu\text{m}$, so that any spot within this area is protected from the incident atomic flux for the majority of the time except when the aperture hovers over. Hence the characteristics of the deposited pattern depend greatly on the size and shape of the aperture. For example, the line width of the nano-pattern is determined by the diameter of the aperture. The PolyMUMPs process has a minimum feature size of 2 µm, meaning that PolyMUMPs native apertures can not be smaller than 2 µm, which is not adequate for fabricating fine structures in the nanometer scale.

To resolve this problem, we use a FIB to mill the aperture for nanopatterning, due to its flexibility and much higher resolution. The writer device design submitted to PolyMUMPs process has no holes on the plate and the apertures are milled after the protective photoresist has been removed, prior to the wet etch. Conducting the FIB process before wet etch has three major advantages: 1) Because silicon and silicon oxide have different electrical properties, the detected sample current when ion beams hit on them can be quite different, hence the sample current can be used as an indicator of when the silicon writing plate is cut through. 2) The silicon oxide layer keeps the writing plate from collapse and snap-in onto the substrate during the FIB process. In the meantime, when the writing plate is milled through, the silicon oxide can prevent damage on the silicon nitride substrate. 3) The ion beam usually induces small amounts of dust and impurities around the targeted area, which could be a problem if one needs a very clean substrate to fabricate fine nanostructures and conduct measurements on them. For example, as will be discussed in the last part of this thesis, nanoscale superconducting thin films have been deposited using this approach. The superconducting properties of such films are extremely sensitive to impurities and film uniformity. The silicon oxide layer protects the silicon nitride substrate from being contaminated. After the wet etch step all unwanted material will be washed away.

The aperture milling is accomplished by a two-step process in FIB. As shown in Figure 2·7 a), assuming we have a POLY2 writing plate, a square region of 4 µm × 4 µm is milled 1.0 µm to 1.3 µm deep through the 1.5 µm plate, to leave a thin membrane as the bottom of the square well. The second FIB step will then focus the ion beam onto a much smaller area to poke through a pinhole as the writing aperture. Figure 2·7 b) shows the SEM image of the resulting structure. The pre-thinning is necessary because a high aspect ratio will reduce the milling resolution. The typical trench aspect ratio for FIB milling without an etch-enhancing gas is approximately four (Yao, 2007). Therefore by pre-thinning the polysilicon plate, it is possible to poke an aperture smaller than 50 nm through the remaining 200-300 nm thick silicon. Theoretically even smaller apertures could be made if the plate can be further thinned, as the width limit of the gallium ion beam can reach ∼5-10 nm (Watt et al., 2005).

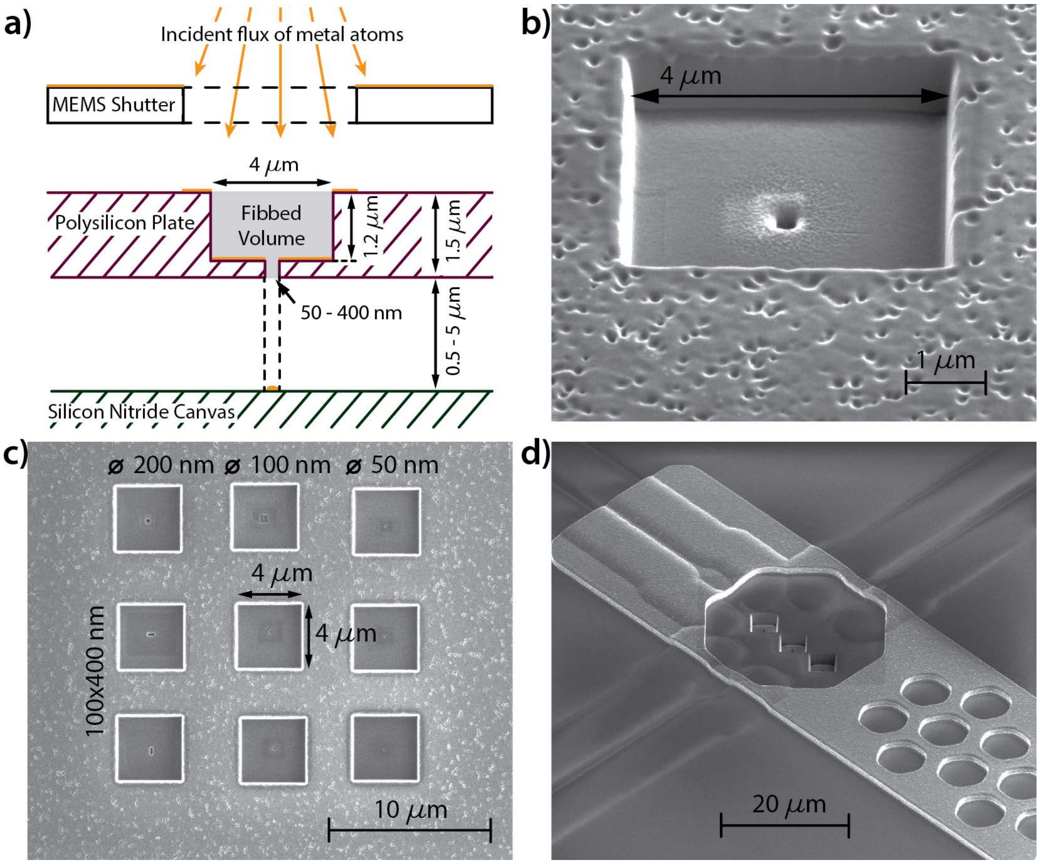

Figure 2·7: The two-step FIB process mills the aperture on the writing plate. a) The diagram shows that the polysilicon writing plate has been pre-thinned before drilling a small aperture. Atoms pass through the aperture to deposit on the canvas. b) An SEM image of the pre-thinned square region and the poked pinhole. c) A 3 × 3 array of apertures with various shapes and sizes. The lower-left and mid-left apertures are 100 nm × 400 nm rectangular apertures. d) An overview of the apertures on the plate and the shutter device. (before release)

However, further thinning the plate is very challenging for the remaining 200-300 nm thickness. The main problem is that the thickness of the thinned square membrane is not uniform the area around the corner and edge is slightly thinner than the central area, as can be seen in Figure 2·7 b). This might be caused by the wall that when hitting the corner, ions may bounce around near the wall to enhance the milling there, resulting in a deeper etch. Hence when aiming at making a thin membrane, the corner may have already been cut through before the desired membrane thickness is achieved. Though not tested, theoretically this problem could be solved by continuously shrinking the focused area during the milling, instead of the two-step milling. This will end up with a bowl-shape well with sloped walls, so that it has a smooth transition from the edge of the well to the central area which is the thinnest, instead of a vertical wall and a sharp bottom edge for the two-step milling process. The smooth transition will significantly reduce the ion bouncing effect to ensure that the central area is the thinnest part with a controllable thickness. Though precisely controlling the milling thickness is still challenging, this provides a potential approach for making apertures much smaller than 50 nm. A transmission electron microscope (TEM) can also be used to poke smaller apertures, however it requires a through wafer etch process which means that the native PolyMUMPs substrate has to be etched beforehand. Another approach for making smaller aperture will be discussed in subsection 2.4.2, focusing on using deposition material to pre-clog apertures.

With the aperture milling technique discussed above, one can make more than one aperture on the same writing plate. Figure 2·7 c) shows a 3 × 3 array of apertures with various shapes and sizes, on the same writing plate. Due to the flexibility of FIB milling, one can put an arbitrary number of apertures with an arbitrary layout on the writing plate, depending on the specific fabrication need. Each aperture can have different dimensions and shapes. This offers an efficient way to make arrays of nanostructures with only one pass of patterning. The topological effect on the fabricated pattern through these apertures will be discussed later.

2.2.3 Timing the fabrication: Ultra-fast shutter

While the writing plate actuated by linear motors is adequate for nanopatterning, the integration of a high-speed shutter brings in more control and flexibility, and even makes single atom deposition possible. The image of such a micro shutter can be found in Figure 2·8. The shutter is basically another polysilicon plate suspended above the writing plate and actuated by a MEMS linear motor of the same type as the writer plate has. Because the PolyMUMPs process only has two movable polysilicon layers, having a shutter integrated means that the writing plate has to be on POLY1, while the shutter plate has to be on POLY2. Such a shutter can only move in one direction as only one linear motor is attached. More complex shutter designs supporting two-dimensional positioning can be implemented by having an extra diagonal linear motor, or even a full set of four motors just as what the writing plate has. Such a design is essentially equivalent to having two independent parallel writing plates, supporting more complicated functionalities for nanofabrication. However, here we will focus on the 1D shutter, as it can be simply operated, and yet offers a lot of new fabrication possibilities. There are several advantages for having an integrated shutter instead of a macroscopic shutter or a micro shutter on a separate die. First of all, an on-chip shutter can greatly reduce the complexity of the setup. Having a separate shutter means that one have to build a "sandwich" setup that the shutter is inserted between the material source and the writer device. This is extremely difficult for a micro evaporation setup with two MEMS chips packaged facing each other, which will be described later in this thesis. The on-chip shutter can solve this problem flawlessly. Second, due to its miniature size, a micro shutter outperforms a macro shutter in terms of the operating speed, which is important for fine control of the deposition amount, especially for single atom deposition. Third, this approach encapsulates two components together to reduce dependency, making a forward step to build a Fab on a Chip. Last but not least, manufacturing an on-chip shutter using the same process is very economic because it imposes no additional cost.

As the gap between POLY1 and POLY2 is only 0.75 µm, having a planar shutter

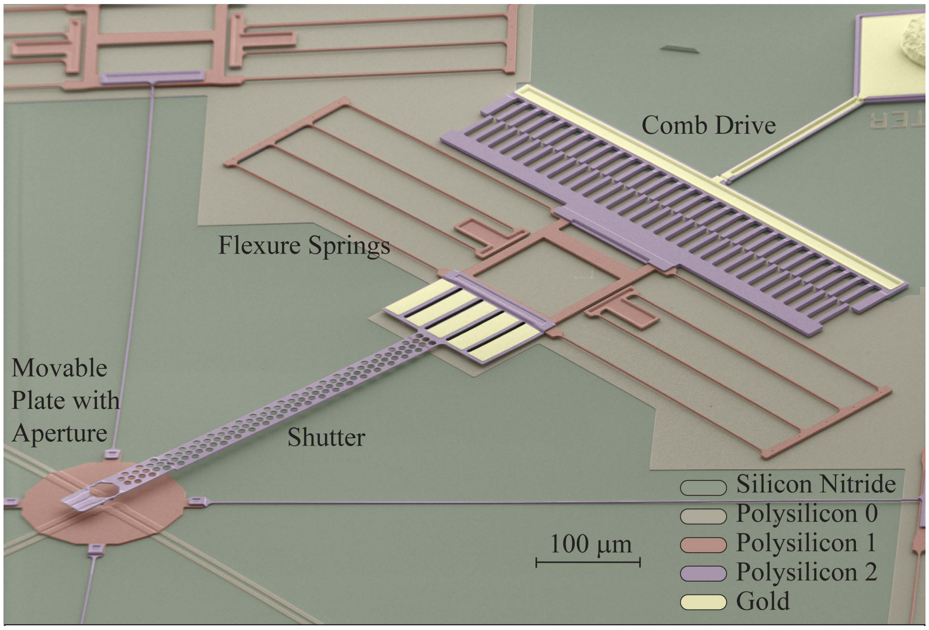

Figure 2·8: A false color SEM image showing the integrated shutter over the writing plate.

plate is very risky because the shutter may collapse onto the writing plate and get stuck. A more serious problem is that as the PolyMUMPs process deposits and patterns each layer one by one consecutively, the bottom of the POLY2 layer with no underlying POLY1 can be even lower than the top of the adjacent POLY1 structure. Therefore a POLY2 structure runs across the edge of a underlying POLY1 plate will form a step on that edge, as can be seen on the shutter near the writing plate edge in Figure 2·8. If the shutter is planar, the step will hit the writing plate when they move towards each other, making the writer stuck. To solve this problem, the shutter has to be lifted to give enough vertical clearance between the shutter and the writing plate. Here we use a bimorph structure, which essentially consists of the native PolyMUMPs gold layer and a polysilicon layer, as can be seen in Figure 2·8. Because of the different residual tensile stresses of gold and polysilicon during deposition, the bimorph structure will curl out of the plane after release, resulting in a slightly inclined tip, so that the other end of the shutter moves up at a position much higher than original. This will offer an additional vertical clearance from a few micrometers to tens of micrometers, depending on the bimorph design. The detail about bimorphs manufactured with PolyMUMPs process can be found in (Morrison et al., 2015).

The shutter is actuated using the similar linear motor found in the writer device. By applying a voltage on the comb drive, the shutter can act as an "on-off" switch for the incident atomic flux. We are interested in the response time because it determines the smallest atomic flux pulse and how precise one can time the deposition. The shutter response time is on the order of the transient time of the resonant mode, given by

$$\tau = \frac{Q}{2\pi f_0} \tag{2.11}$$

where Q is the quality factor of the shutter system and f_0 is the resonance frequency. For a typical shutter device, Q is on the range of $10^2 - 10^4$, while f_0 is on the order of 5 kHz, resulting in a transient time of τ = 2-200 ms. However, given that the aperture is very small and one can place the shutter close to the aperture edge, the actual "on-off" transition time can be shortened to the order of 10 µs (Imboden et al., 2013). Due to the miniature size of the writing aperture and the high speed of the shutter, the deposition of single atoms is possible. Assuming that the aperture measures 100 nm on each side and the deposition rate is about one monolayer per second, roughly 10^5 atoms per second are transmitted on average through the aperture. The 10 µs response time of the shutter is fast enough to stochastically allow only one or a few atoms to pass. It should be noted that the number of atoms can be of order one, but the placement accuracy is defined by the area of the aperture and the position control of the writers.

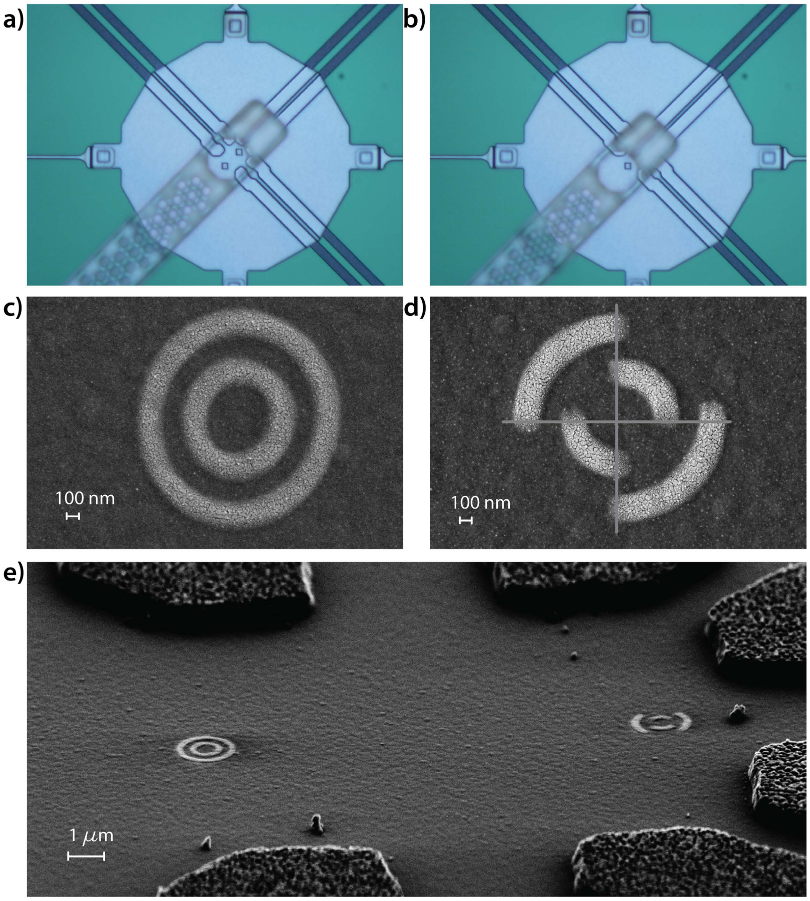

Figure 2·9: The operation of the integrated shutter and the resulting nanopattern. a) The shutter opens one aperture while keeps the other one closed. b) The shutter exposes both apertures. c) The concentric nano-rings fabricated through the always-open aperture. d) The incomplete nano-rings fabricated through the periodically opening and closing aperture. e) An overview of the canvas after the deposition is done.

The basic function of the shutter is to selectively open and close apertures during the evaporation, so that some of the apertures can be saved for the next step in a multi-step deposition process. The shutter has to dynamically follow the motion of the writing plate to make sure that the right aperture is open or closed at the desired time. Figure 2·9 illustrates the effect of such an “on-off” shutter. In this example, two apertures were milled on the writing plate and a shutter is used to periodically open and close one aperture, while keep the other one always open. Figure 2·9 a) and b) show the optical microscopic photos of the actuation of the shutter at 40 V and 70 V on the comb drive, respectively. In Figure 2·9 a), both apertures are open for the incident atomic flux, while in Figure 2·9 b) one of the aperture is covered by the shutter. Periodically varying the driving voltage on the shutter will turn one aperture on and off periodically. During the deposition, we actuated the writer to move in a trace of two concentric circles and the fabricated nanostructures in such a setup can be found in Figure 2·9 c) and d). Shown in Figure 2·9 c) is the SEM image of the complete concentric nano-rings fabricated through the always-on aperture, while Figure 2·9 d) is the SEM image of broken nano-rings truncated into four quadrants fabricated through the periodically opening and closing aperture. Both structures are patterned simultaneously by only one writing pass. The different outcomes are obtained purely by controlling the shutter. This experiment illustrates that with the help of the shutter, one can choose which aperture to use and when to use it based on the specific fabrication need, especially when conducting the multi-step fabrication process.

2.3 Atomic calligraphy setup, calibration and dynamics

2.3.1 Device packaging and fabrication setup

The writer die is packaged inside an 8 pin or 16 pin dual in-line package (DIP) ceramic socket for use. Electrical access to the device is achieved by ball bonding from the contact pads (shown in Figure 2·1) to the socket pins. Each contact pad has the native PolyMUMPs gold layer to provide adhesion to the ball and reduce contact resistance. After attached to the DIP socket, the top surface of the MEMS die is slightly lower than the edge of the socket so that a thin mask can be placed above the device without touching the MEMS. The thin mask, made of copper, has a hole in the center that is around 75 µm, slightly smaller than the writing plate. Hence, the incident atomic flux can only reach the writing plate. This guarantees that only the patterned nanostructure is deposited on the substrate. There are three major reasons why it is necessary to keep the deposited material off of other writer components: 1) Many commonly used materials like metals are conductive. If deposited everywhere on the surface of the die, it will electrically short out the micro circuits of the device, including the electrodes of comb drives and the contact wires. 2) Materials deposited on the comb drives or folded springs will alter their electrical and mechanical properties, therefore affect the accuracy of writer plate positioning. 3) The excessive material nearby the fabricated nanostructures may impact the experiment. For example, if one fabricated iron nanostructures and tried to measure the magnetic properties, the excessive iron around the writing area may interfere with the measurement thus making the results invalid.

The atomic flux is provided by conventional directional physical vapor deposition (PVD) techniques, such as thermal evaporators or e-beam evaporators. In a thermal evaporator, evaporant placed in a metal boat or coil is joule heated by passing a current through the boat or coil. Thus some hot atoms near the material surface may have enough kinetic energy to overcome the interaction among other atoms and escape from the surface. When inside a high vacuum environment, those atoms can have a very long mean free path so that they will fly in a straight trajectory with a very small chance to collide with the background gaseous molecule, until they hit a cold object and condense on it. The direction of the evaporated atom is random, however, if the evaporation source and the deposition target are relatively small compared to the distance between them, then the target will see a highly directional atomic flux coming from the source. It is desired for Atomic Calligraphy to work with directional atomic flux because it results in a well-defined line width for the nanostructure.

The DIP socket with the writer device packaged is inserted onto a sample stage inside a thermal evaporator, as shown in Figure 2·10. Electrical access to the socket is obtained through an electrical feedthrough. A multi-channel voltage source controlled by a computer is used to actuate the comb drive of the writer. The sample stage can be cooled by running liquid nitrogen through, enabling the quench condensation of nanostructures down to 77 K. A thermal baffle is installed to prevent excessive hot atoms to land on the sample stage because the thermal radiation from the source and the thermal energy brought by hot atoms may suppress the cooling power of liquid nitrogen. The atomic flux is provided by an evaporation source. Depending on the evaporant, the specific evaporation source has to be chosen carefully so that no chemical reaction or other incompatibilities could occur between the evaporant and the source. For gold evaporation, a tungsten coil coated with aluminum oxide is used. The current for heating the source is manually controlled and a thickness monitor is used to monitor the deposition process so that one can tune the deposition rate during patterning. The thickness monitor exploits a quartz crystal resonator for sensing the deposited mass. A shutter (not to be confused with the integrated

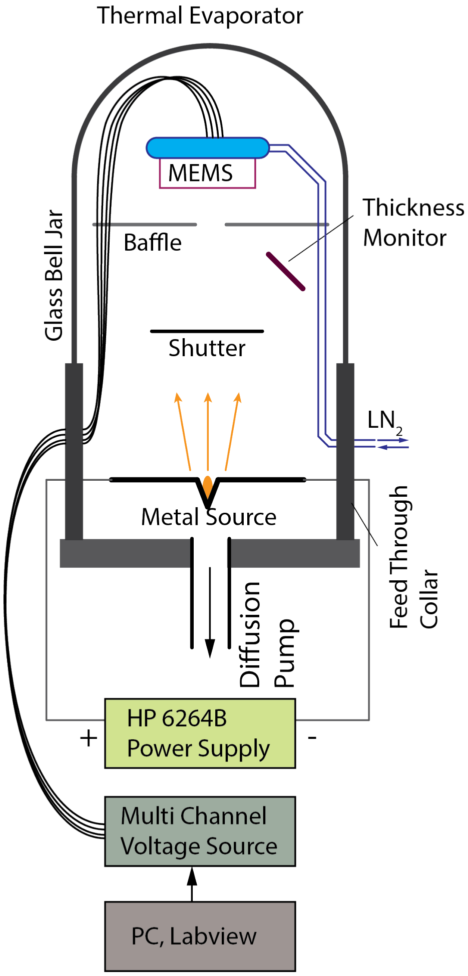

Figure 2·10: The evaporator setup for Atomic Calligraphy. The writer device is mounted on a sample stage which can be cooled by liquid nitrogen. Electrical feedthroughs provide access from the outside in order to actuate the device during deposition, which is monitored by a conventional thickness monitor.

MEMS shutter) opens and closes the incident atomic flux so that one can tune the deposition rate before actually opening the shutter to ensure the delivery of a steady and constant flux to the writer.

2.3.2 Calibration of writer plate positioning

In order to accurately position the writer plate for patterning, it is necessary to experimentally determine the coefficient in Equation 2.4. Device characteristics including comb drive geometry and layer thicknesses may vary among different device designs and PolyMUMPs runs, so that the device has to be calibrated if the design changes or when the new run arrives. To achieve that, we deposited nanoscale dots through the writing apertures, under several discrete driving voltages on the comb drive. It needs to be pointed out that the shutter is closed when the driving voltage changes and is open again after the plate stabilizes at the equilibrium position to ensure that the deposited dot accurately reflects the equilibrium position of the plate. Such a calibration result is illustrated in Figure 2·11. At the beginning, a dot was deposited at the origin when there is no actuation voltages on any comb drives. Then the writing plate was actuated along x-axis for ten different voltages with equal V^2 spacing and a dot was deposited for each voltage. Ten similar dots were deposited with two axis actuation. The SEM image of the resulting pattern is shown in Figure 2·11 a). Positions of these dots were measured in an SEM to plot displacement versus V^2 data as shown in Figure 2·11 b). According to Equation 2.4, a linear fit was performed on the data, and the residuals between the fitting line and the experimental data were plotted in Figure 2·11 c).

According to the fitting, the displacement of the writer plate can be expressed as:

$$x = (1.270 \pm 0.001)\,\frac{\mathrm{nm}}{\mathrm{V}^2} \times V_x^2 \tag{2.12}$$

$$y = (1.357 \pm 0.003)\,\frac{\mathrm{nm}}{\mathrm{V}^2} \times V_y^2 \tag{2.13}$$

Because of the high linearity, the uncertainty of the fitting parameter is small. This

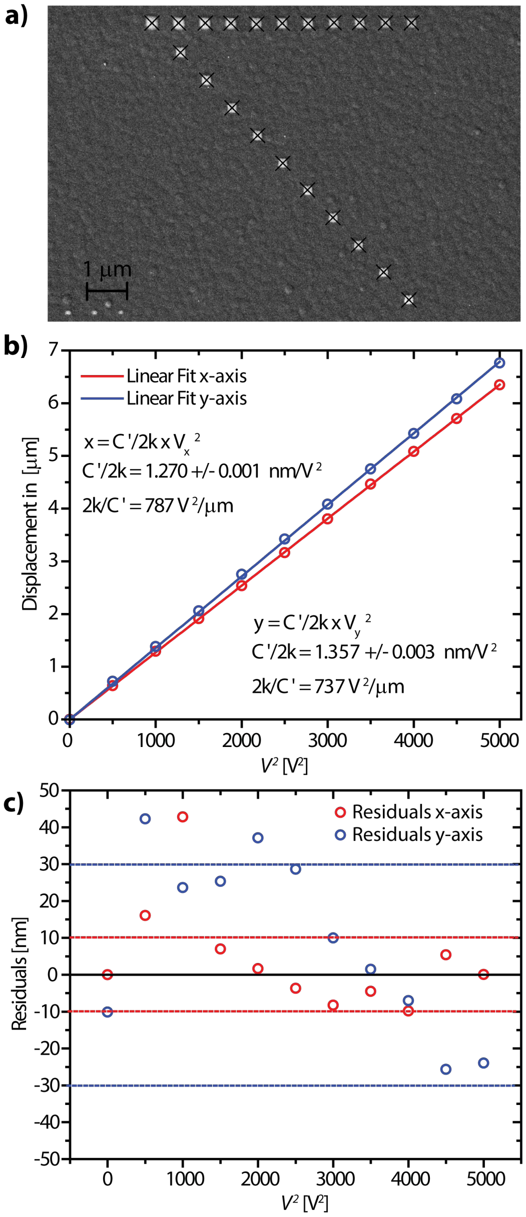

Figure 2·11: The calibration of the writer device. Multiple nanoscale dots were deposited at different driving voltages. By measuring the displacement of each dots with respect to the original points, one can get a relationship between writing plate displacements and driving voltages. a) The SEM images of the deposited calibration dots. b) A linear fit shows that the V^2 dependence model works very well in this case. c) The residual between the fitting line and the experimental data.

calibration result is from a specific device and devices from other runs with other designs generally have slightly different parameters. Our experiments show that devices with identical design from the same run exhibit very similar behavior though, so that the calibration data can be used for the same batch of devices.

The V^2 dependence is desired for nanostructure writing because it provides a long working range using reasonable voltages, as well as the precision needed for sub-nanometer positioning. As an example, for the calibrated device presented above, it only needs $\sim 90\,\mathrm{V}$ to move the plate for $10\,\mu\mathrm{m}$ along x-axis. On the other hand, we gain a high precision around the origin. $1\,\mathrm{V}$ only moves the plate by $1.27\,\mathrm{nm}$ while $0.1\,\mathrm{V}$ corresponds to only $0.127\,\text{Å}$. This means that one can create micron scale patterns up to tens of micrometers, while still have the ability to write fine sub-nanometer structures on the same canvas.

Digital Imaging Correlation (DIC) technique is another method to calibrate the device. The idea is to take optical microscopic images of the device and use digital image processing algorithm to calculate the displacement of the plate. The device is placed under an optical microscope and images of the plate are taken at different actuation voltages. The camera, lens and the sample stage have to be fixed and the entire microscope has to be installed on a vibration isolation table in order to minimize the mechanical noise. By comparing the differences among images, the algorithm can calculate how many pixels the target structure has moved. Since it averages over the entire image, sub-pixel precision is achievable. The detail of performing this technique on the writing plate has been discussed in the supplementary material of (Imboden et al., 2014a). Similar applications on MEMS can be found in (Liu et al., 2007). The algorithm and fitting method are described in (Hung and Voloshin, 2003).

2.3.3 In-plane oscillation and smearing effect of the writer

Since the writer plate is connected to four folded springs, the plate is subject to in-plane oscillation during actuation. This oscillation reduces the response time of the plate and also introduces ring-down effect that when the plate is abruptly displaced to a new position, it will undergo small damped oscillation around the new position. Such ring-down effect will lower the deposition precision when the patterning trace is not continuous. To evaluate the ring-down effect, we first calculated the resonance frequency of the writer's in-plane lateral oscillation. The spring constant of the system for in-plane lateral movement is given by Equation 2.10. The total effective mass can be estimated by summing up the mass of the writer plate, tethers, two sets of the movable combs and springs. For a rough estimate, considering that parts of the springs will only move by half of the displacement, the total effective mass for such a writer is 5.23×10^{-10} kg. Therefore, the resonance frequency of the system is given by:

$$f_0 = \frac{1}{2\pi}\sqrt{\frac{k}{m}} \approx 4.77\text{kHz} \tag{2.14}$$

The quality factor of the writer under vacuum is in the range of $10^2 - 10^4$. The ring-down time is on the order of the transient time of the resonant mode, which is 2-200 ms, according to Equation 2.11.

To visualize the ring-down effect, we conducted depositions by alternatively turning on and off the driving voltages on two perpendicular comb drives. During gold deposition, a voltage on x-axis comb drive was applied for a few seconds and then turned off, followed by a similar actuation on y-axis. Then the same procedure was repeated over and over again. At each position, we paused for a few seconds to wait for the writer to ring down and stabilize. The resulting pattern can be seen in Figure 2·12. At position (II) and (III), the deposited dot was elongated along the axis of actuation, because the plate was pulled abruptly by the voltage pulse so that it oscillated around the equilibrium point along that axis. The evaporated gold then deposited along the trace of oscillation. At the origin (I), the dot has a cross shape because the plate has been released from distant points along either x or y-axis, so that the plate bounced back and forth along both axis.

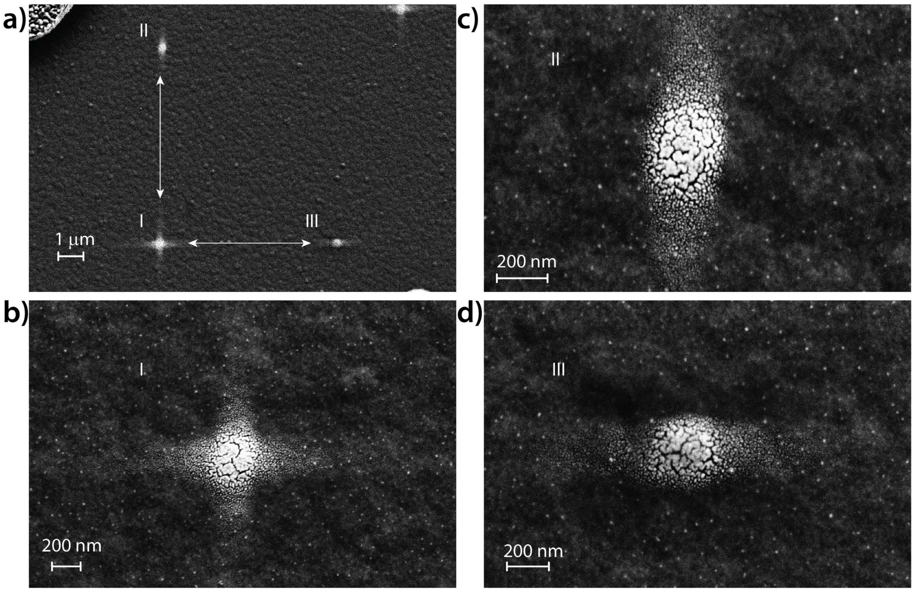

Figure 2·12: The deposited structures show ring-down effect of the writer. a) The overview of three deposited dots. b) The dot deposited at origin (I) exhibits a cross shape due to the ring-down. c) The dot deposited with a displacement along y-axis (II). d) The dot deposited with a displacement along x-axis (III).

Traditionally such a ring-down effect can be suppressed to improve the response speed by building a feedback loop, as elaborated in (Maithripala et al., 2005). However, the feedback loop requires additional sensing mechanism to detect the real-time position of the writer plate. Though it has not been implemented, theoretically the position sensing can be done by using the comb drive on the other side as a capacitance sensor, so that one can measure how far the writer has moved by detecting the capacitance change. Additional equipment or circuits are also required to support the sensing mechanism. Another approach for minimizing the ring-down is actuating with a multi-step voltage pulse, in which one tune the shape of the voltage pulse, instead of using the simple square waveform. Such techniques with applications on MEMS electrostatic actuation have been discussed in (Chen and Ou, 2007).

The writing plate being suspended a few microns above the substrate induces the smearing effect of the deposited pattern, as shown in Figure 2·13. This is mainly due to the fact that the source has finite dimensions (the diameter of the evaporant in the thermal evaporation coil is 2-4 mm) so that it does not behave like a point source. Figure 2·13 b) illustrated how such effect results from the finite-sized evaporation source. With a 200 nm diameter aperture, theoretical calculations on the smearing effect for 5 µm and 0.5 µm plate height are presented in Figure 2·13 a), respectively. The inner circle in Figure 2·13 a) defines the umbra area which receives full deposition from the source, while the area between the inner and outer circle is the penumbra which only sees part of the source. It can be seen that the smearing can be minimized when the plate is brought close to the substrate. Experiments also show this effect and the SEM images of the deposited dots can be found in Figure 2·13 c). For such depositions, a smeared dot was deposited when the writing plate was suspended about 5 µm high above the substrate. The plate was then moved by a few microns along y-axis and pulled down to the substrate by applying a voltage between the plate and the wafer base. By depositing through the pulled-down writer, a clear dot with well-defined edge was then obtained.

In order to control the smearing effect of the deposited pattern, one has to be able to control the height of the plate above the substrate. By applying a voltage between the plate and the silicon base of the die, the plate can be pulled towards the substrate. However, due to the 1/3 pull-in effect that has been discussed before

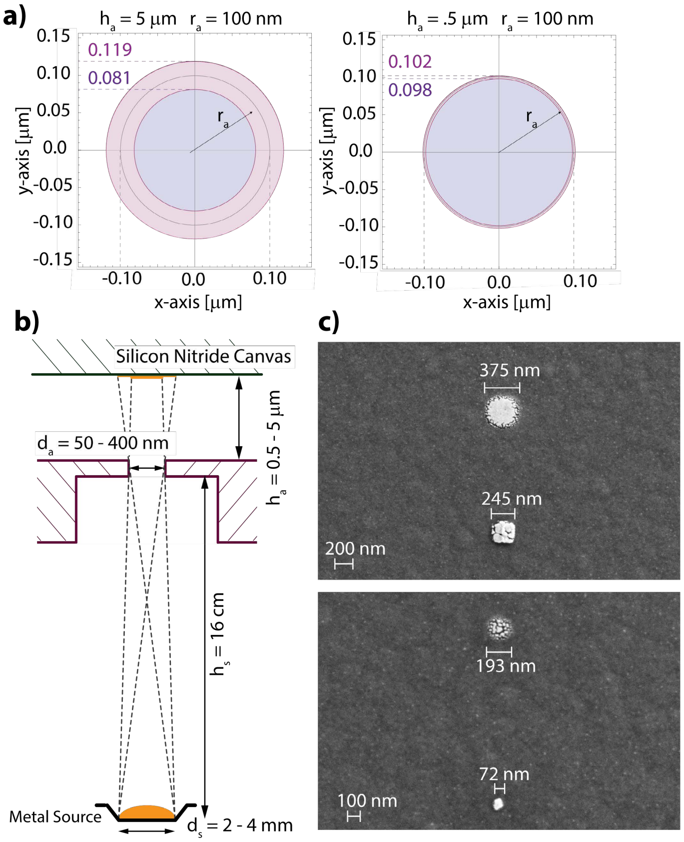

Figure 2·13: The smearing effect of the deposited pattern through the writing aperture. a) Simulation results of the deposited dots given that the radius of the aperture is 100 nm and the distances between the plate and the substrate are 5 μm and 0.5 μm, respectively. b) A diagram showing how atomic flux passes through the aperture and how the smearing is resulted. c) SEM images of the deposited dots before and after the writing plate pull-down.

(Nadal-Guardia et al., 2002), theoretically one can only control the height of the plate for the first one third of the total clearance. A better way to control the plate along z-axis might be to take the advantage of the comb levitation effect as we have discussed in subsection 2.2.1. However, this requires a more complicated comb design illustrated in (Imboden et al., 2014b).

2.4 The direct writing of nanostructures

2.4.1 Calligraphy effect of the aperture

Because the writer actually “writes” material on the canvas, its aperture behaves just like a pen nib — due to the shape of the aperture and its orientation with respect to the plate moving direction, it produces a calligraphy effect that the stroke of the pattern stays conformal to the aperture shape. To showcase various calligraphy effects, we prepared a writer plate with nine different apertures arranged in a 3 × 3 array. Gold deposition was conducted on the writer with one writing pass to get nine structures with the same pattern, but different line strokes, due to the different sizes and shapes of the apertures. The SEM images of the deposited patterns can be found in Figure 2·14. For instance, as shown in Figure 2·14 b), a rectangular slot aperture draws narrow and thick lines when it moves along the length, but wide and thin lines when it moves along the width. By taking advantage of this effect, one gains even more flexibility in fulfilling fabrication requirements, since one can define any aperture shapes using a FIB.

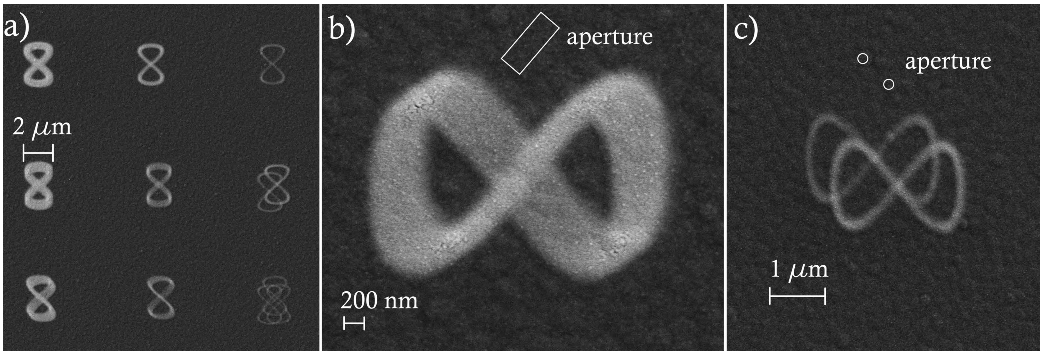

Figure 2·14: Calligraphy effect of the apertures in a 3 × 3 array. The patterns were obtained with one writing pass. Each pattern has a different stroke resulted from the aperture variation. a) SEM images of nine patterns fabricated through the aperture array. b) The infinity pattern deposited through a rotated rectangular slot. c) The infinity pattern deposited through the dual-hole aperture.

2.4.2 Line sharpening and aperture filling-in

Another phenomenon happening during nanostructure writing is the filling-in effect of the aperture that the material accumulated on the side wall of the aperture shrinks the opening of the aperture. This process gradually proceeds during the deposition until the aperture gets completely clogged. The thickness of material one can deposit through the aperture before it fully closes is on the same order of the aperture size. However, the line width of the written structure keeps decreasing during the deposition. To visualize this process, three lines were drawn through three apertures with constant plate moving speed and deposition rate. The SEM images of the deposition can be seen in Figure 2·15. For different aperture sizes, two edges of each trace form the same angle, implying that the decreasing speed of the aperture diameter stays the same, independent of the original aperture size. While in general this effect impairs the consistency of the line width throughout the entire deposition process, it can be exploited on the other hand to fabricate structures smaller than the original aperture dimensions. As we have discussed in subsection 2.2.2 that making apertures smaller than 50 nm may be challenging, one can use a larger aperture and pre-clog the aperture to make it small. This also enables run-time aperture shrinking which means that one can use a regular aperture to fabricate some structures, then move the plate away and deposit some material to close up parts of the aperture to make it smaller and finish the deposition with this tapered aperture. This might be extremely useful when one needs to build a relatively large nanocircuit and then deposit a few atoms of impurities on the circuit for quantumn transport experiments.

To overcome the clogging problem, a cleaning mechanism which cleans the material accumulation around the aperture has to be implemented. A possible way might be to heat the writing plate so that the material gets evaporated off of the writer plate

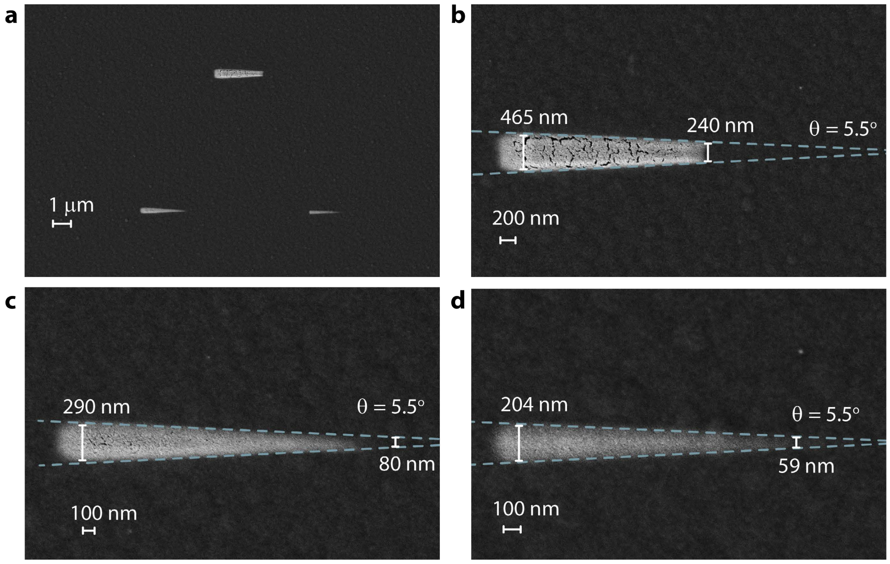

Figure 2·15: Line sharpening due to the filling-in effect of the aperture. Three apertures with different diameters were milled on the writing plate. The writer was then actuated to move from left to right slowly during gold deposition with a constant rate. Three lines with varying width were drawn through the apertures, showing the effect of aperture closing up.

and the aperture opens up again. The tethers can be used as heaters by running a current through. Because the tether is long and narrow, it has a relatively large resistance thus the current induces joule heating on the tether. The writing plate is suspended only by the tether, so that when in vacuum the thermal conduction through the tether will dominate the transfer of heat. Hence the plate stays isothermal and its temperature is controlled by the heating on the tether. This technique uses the similar idea of our micro evaporation sources which will be discussed in later chapters. Preliminary experiments has been carried out, showing that it is feasible to keep materials off of the aperture during deposition by heating the plate. However, the heat also changed the mechanical properties of the tether and the thermal stress inside the tether even deformed it so that the tether touched the substrate. This significantly affected the positioning of the writing plate and has to be solved before one can use plate heating to clean the aperture.

2.4.3 Nanostructure array printing

Due to the fast response speed of the writer, the writer can actually "print" nanostructures. The major difference between printing and writing is that for writing, the writer moves relatively slowly to deposit continuous pattern defined by the trace of the movement, while for printing the writer deposits a dot at each pixel of the structure and jumps among pixels to finish the deposition so that all dots will eventually form a pattern. In the printing mode the writer works just like a macroscopic ink-jet printer, which scans through a bitmap line by line and sprays ink for each pixel. However, for our writer device, the atomic flux is usually kept constant throughout the deposition process. Therefore the discontinuity of deposition when jumping form one pixel to another is realized by making the transition very fast, so that very few atoms can reach the canvas along the route of plate moving. The plate will then stay static at the pixel for material deposition until a desired thickness is reached, before jumping to the next pixel. As has been discussed in subsection 2.3.3, ring-down effect could be a problem for printing especially when the pixels of the designed structure are too sparse. To overcome this difficulty, multi-step voltage pulse actuation could be an option, but a more practical way is adopting a combination of slower deposition rate and longer waiting time for each pixel, so that the leakage during plate moving is minimized.

When there is an aperture array on the plate, multiple identical structures can be printed simultaneously with one printing pass. To demonstrate this technique, a 4 × 4 array of words "BU" was printed with gold being the deposition material, as shown in Figure 2·16. The bitmap of the designed structure, "BU" in this case, was loaded into

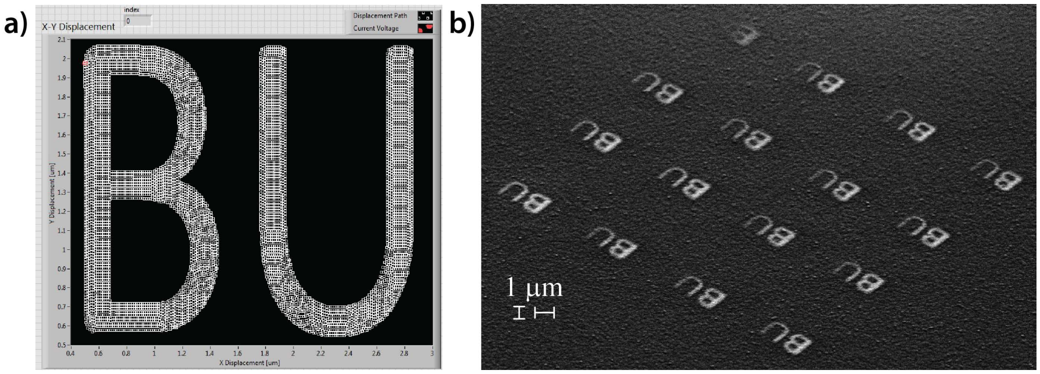

Figure 2·16: A 4 × 4 array of words "BU" was printed by the writer using gold. a) The screenshot of the LabVIEW program used to control the writer actuation shows the bitmap of the word "BU". b) The SEM image of the deposited nanostructure array.

the LabVIEW program which controls the writer by controlling the voltage sources for each individual linear motor. The screenshot of the program in Figure 2·16 a) shows the bitmap data of the structure. During the deposition, the program scanned each pixel of the bitmap line by line. If the current pixel has a non-zero thickness value, the program will move the writer to the corresponding position and wait for a certain length of time, which is calculated from the thickness setting and current deposition rate. This ensures that every dot can reach the desired thickness. The SEM image of the nanostructure array is shown in Figure 2·16 b). All 16 patterns are fabricated altogether with one printing pass.

2.4.4 Nanoscale 3D printing

So far all structures fabricated using the writer are single layer structures. However the writer is even able to fabricate structures with higher topological complexity, by depositing and patterning another material as a sacrificial layer. In this case, suspended structures are made possible by patterning the sacrificial layer beforehand underneath the structure material. A release step removes the sacrificial material to set free the 3D structure. This process is similar to the conventional lithography technique for building multi-layer structures, but the major difference is that all patterning work is done by the writer instead of lithography.

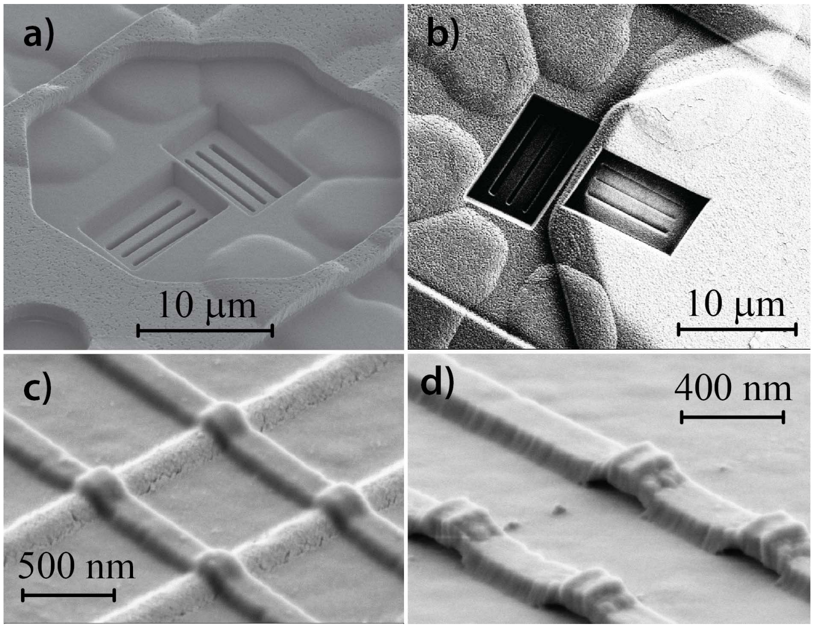

Figure 2·17: SEM images shows the procedure of nanoscale 3D printing. a) Two sets of slot apertures were milled using FIB for sacrificial layer and bridge layer deposition, respectively. b) After the deposition of the gold sacrificial layer, the imprint of shutter opening is visible on the writer plate as it is used to protect the other set of apertures for future bridge deposition. c) The chromium bridges are deposited on top of the gold ridges. d) After gold etching, the underlying gold was removed to release the suspended chromium structure.

Figure 2·17 highlights several steps of such a 3D printing process. In this example, we used chromium as the structure material and gold as the sacrificial material. The deposition was conducted in an evaporator where one can switch between two different evaporants for deposition. Apertures for both sacrificial layer patterning and structure layer patterning were milled on the same writer plate using FIB, but separated by a distance so that a shutter could be used to selectively expose designated apertures. In this case, two sets of slot apertures with perpendicular orientations were prepared. Each set consists of three long parallel slots, as shown in Figure 2·17 a). we used one set of slot apertures to deposit gold strips on the substrate as sacrificial structure. During gold deposition, the writer stayed static and the other set of apertures were saved by the shutter for future fabrication of bridges. The gold imprint that can be seen in Figure 2·17 b) shows how the shutter was used to only expose one set of apertures at a time. The thickness of gold layer determines the height of the nanobridge suspended above the substrate. After gold deposition, the writer moved to bring the unused perpendicular slot apertures over those pre-deposited gold strips. Chromium evaporation was then conducted to fabricate chromium strips across gold ones so that bridge structures were formed on top of gold ridges, as can be found in Figure 2·17 c). Then the die was taken out of the evaporator and the writer plate was removed carefully by a probe. A final release step was carried out by immersing the die into gold etchant to dissolve gold strips but keep the chromium intact. The chromium bridge was then suspended as shown in Figure 2·17 d).

In principle, multi-layer 3D nanostructures can be manufactured by repeating the similar procedure multiple times. However, the release step must be the final step and can only be executed once. This is because that in order to dissolve the sacrificial material the whole die has to undergo the chemical etching process which usually alters the electromechanical properties of the device and even destroys the functionality of the writer. It has been proposed that some material like water or carbon dioxide may be used as the sacrificial material.(Han et al., 2010)(Gardener and Golovchenko, 2012) Molecules of these materials condense when they hit the cold substrate and sublime once the temperature is raised up again, leaving no residual. This self-release property provides a way to fabricate multi-layer 3D nanostructures without the need of breaking the vacuum and removing the die for release, enabling experiments and measurements to be done *in-situ*. While for traditional lithography patterning ice can be a real challenge, the direct writing of material with our writer is a physical process which doesn't require the deposition material to have specific chemical properties for patterning. Hence the Atomic Calligraphy approach is naturally compatible with such material. However, the evaporator does need special apparatus to spray molecular flux into vacuum with a controllable rate.

2.5 Conclusion

In this chapter, a new approach of fabricating nanostructures using MEMS, namely Atomic Calligraphy, is introduced. The writer device consists of a writing plate and four MEMS linear motors so that the plate can be precisely positioned on a 2D plane. Atomic flux emitted from the source of an evaporator passes through the apertures on a moving writer plate to form nanoscale patterns. The apertures are milled using a FIB to achieve nanoscale structure line width. Due to the miniature size of the device and V^2 dependency actuation of the comb drive, the writer plate can be positioned with sub-nanometer precision. A micro shutter is integrated for aperture selection and fabrication timing control, which has the potential to further enable single atom deposition. Various nanostructures have been fabricated using this writer device to characterize the functionality and versatility of this technology. Since the patterning process described here is a final step process which does not require chemical developing and etching steps, a broader selection of material is available and *in-situ* experiments are made possible. It has also been shown that with the introduction of a secondary material as the sacrificial layer, one can even build 3D nanostuctures using such a device. Integrating the writer with other MEMS based counterparts of a fab will eventually enable the build of a Fab on a Chip which brings the entire nanofabrication system down to the microscopic scale.

Chapter 3

MEMS Mass Sensor: Film Thickness Monitoring

3.1 Overview: MEMS resonators as mass sensors

A crucial element for any fabrication or deposition system is a film thickness monitor/mass sensor, so that one knows how the process is going. While the writer device consists of actuators, which are devices that can manipulate the environment to produce a desired outcome, MEMS technology has also been extensively used for sensing. Examples include magnetometers,(Aksyuk et al., 1998) chemical sensors,(Waggoner and Craighead, 2007)(Laconte et al., 2004) inertial sensors, and pressure sensors.(Judy, 2001) In this chapter, I will demonstrate using MEMS for mass sensing so that high resolution thickness monitoring for nanofabrication is achieved. The speed, sensitivity, and ability to be integrated on chip makes this an attractive approach. MEMS mass sensors have already been realized; examples include arrays of CMOS integrated sensors with femtogram resolution(Villarroya et al., 2006) as well as functionalized resonators for biological sensing with pg/fg resolution.(Ismail et al., 2008)(Lee et al., 2011) As will be shown in Chapter 4, the resonator has a working range of deposition amounts over eight orders of magnitude. The sensitivity levels are ideally suited for Fab on a Chip applications considered. Since it is manufactured using the same PolyMUMPs fabrication process as the writers, the sensor can be integrated on chip with micron alignment accuracy.

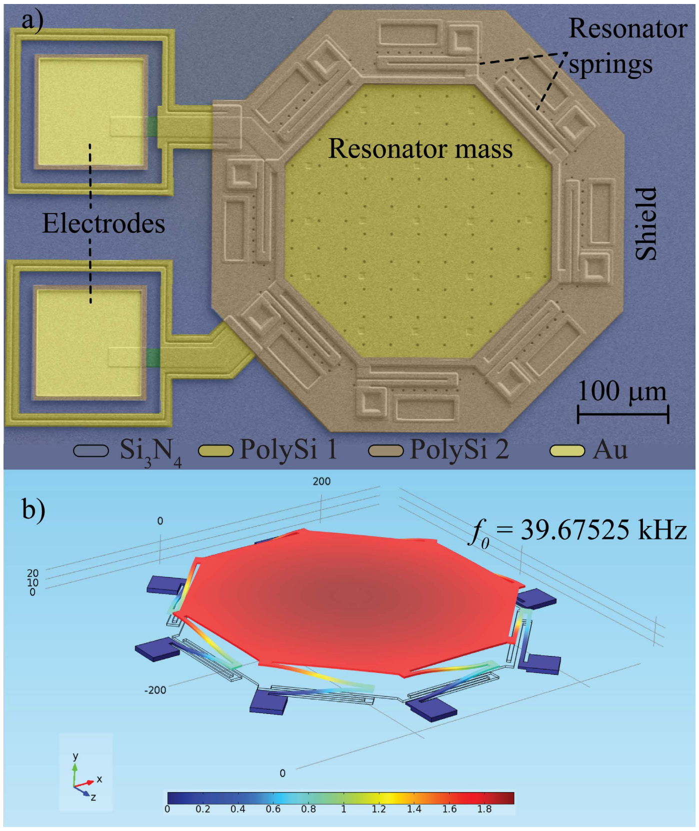

Figure 3·1: a) Colored SEM image of the integrated mass sensor. b) Finite element simulation showing the amplitude of vibration of the fundamental resonance mode.

An example of such a mass sensor we have built based on MEMS principles is shown in Figure 3·1 a). Figure 3·1 b) visualizes a finite element simulation of the fundamental mode occurring just below 40 kHz. The mass is dominated by the octagonal plate in the center. Eight springs are arranged around the edges and covered by the tan structure around the perimeter. The print-through from the manufacturing process makes the underlying springs visible. Similar square plate designs with four springs and resonance frequencies ranging from 40 kHz to 200 kHz have been manufactured and tested as well. The cover is needed to protect the springs from the atomic flux. This ensures that the deposited atoms only add mass to the resonator and do not affect the restoring force. As a result the change in the resonance frequency is purely due to the added mass and not dependent on other properties, such as elasticity, of the deposited material. The frequency can be monitored in a closed loop setup with an accuracy better than 1 part in 10^8. As will be discussed next, mass weighing is achieved by monitoring the resonance frequency shift.

3.2 Modeling the mass sensor

The mass sensor was modeled in 3D using CAD software with the same design parameters as the MEMS design. The 3D model was then imported into COMSOL Multiphysics Modeling Software for eigenfrequency simulation. To mimic material deposition, a mass loading boundary condition was applied to the upper surface of the center plate, within the same area as the shield opening. When using a mass loading boundary condition, mass is added without changing the stiffness of the structure. This approximation is only valid if the added material does not contribute significantly to the spring constant of the device. The assumption holds for three reasons: 1) many metals used for deposition, such as gold, have much higher densities and lower Youngs moduli than silicon, making the mass contribution to the resonance shift dominate the mechanical contribution; 2) the spring constant of the device is determined predominantly by the folded spring, while all the added mass is confined on the plate which is much stiffer than the spring; 3) very little tension can exist in the deposited film because, for the thickness range of interest, the deposited film is not continuous due to the fact that the surface roughness of the polysilicon is on the order of 10 nm.

Though most of the spring constant is provided by the folded spring, the oscillating plate itself may also bend on resonance, causing the plate to curve. The concept of effective mass is exploited to better model the spring-mass system. For any real resonator, the mass along the length of the spring has a distribution in amplitude. The effective mass is a measure of the relative displacement of each infinitesimal mass unit, and can be defined as followed:

$$\iiint \frac{1}{2}v^2 \,\mathrm{d}m = \iiint \frac{1}{2}\rho v^2 \,\mathrm{d}V = \frac{1}{2}m_{eff}v_{\max}^2 \tag{3.1}$$

The left-hand side (LHS) is the total kinetic energy of the oscillation system. The right-hand side (RHS) is the kinetic energy of a point mass with a velocity the same as the maximum velocity for all points of the oscillating system. The effective mass is mode dependent and always smaller or equal to the true mass. The effective mass of the deposited thin film Δm_{eff} can be defined in the same way, where in this case the integral runs over the volume of added mass, not the entire resonator. As discussed previously, the spring constant of the system will not be affected by the added mass, therefore, for a small added mass (small compared to the total mass of the resonator), a simple relationship between the effective mass change and resonant frequency can be used:

$$\frac{\Delta f}{f} = -\frac{1}{2}\frac{\Delta m_{eff}}{m_{eff}} \tag{3.2}$$

The effective mass of the mass sensor m_{eff} can be easily calculated by integrating over the volume of the resonator:

$$m_{eff} = \rho \iiint (\frac{v}{v_{max}})^2 \,\mathrm{d}V = 0.8013 m_0 = 1.354 \times 10^{-10}\,\mathrm{kg} \tag{3.3}$$

Here, $m_0 = 1.690 \times 10^{-10}\,\mathrm{kg}$ is the mass of the mass-spring system in the simulation, including the oscillating plate and the folded springs. v/v_{max} is determined by oscillation geometry assuming that, for a small amplitude oscillation, each point of the system is undergoing a harmonic oscillation with the same frequency. Thus the ratio of velocities between two different locations is equal to the ratio of the amplitudes.

The effective mass of the deposited film Δm_{eff} for a given actual mass Δm is also obtained by taking the surface integral over the area of the shield opening on the oscillating plate. Assuming a uniform thickness, we get

$$\Delta m_{eff} = \frac{\Delta m}{A} \iint (\frac{v}{v_{max}})^2 \, \mathrm{d}S = 0.8581 \Delta m \tag{3.4}$$

where A is the area of the shield opening. The ratio between Δm_{eff} and Δm stays constant for varying Δm because it depends entirely on the geometry and oscillation mode of the mass sensor. In this case, by combining this ratio into m_{eff}, Equation 3.2 can be rewritten as

$$\Delta m = -2 \cdot m_{ce} \cdot \frac{\Delta f}{f} \tag{3.5}$$

where m_{ce} is the combined effective mass. $m_{ce} = \dfrac{1.354 \times 10^{-10}\,\mathrm{kg}}{0.8581} = 1.578 \times 10^{-10}\,\mathrm{kg}$.

The simulated frequency shift for an added mass boundary condition of the fundamental mode is plotted in Figure 3·2. The fit confirms the linear relationship between the frequency shift and change of effective mass with a slope of -0.4956 ± 0.0004, which is close to the theoretical prediction of $-1/2$. The intercept is $-9.42 \pm 2.37 \times 10^{-6}$. The fitting line, together with Equation 3.3 and Equation 3.4, is the basis of measuring mass of change by monitoring frequency shift. It should be noted that the linear relationship only holds within a certain regime because, for large mass change, the accurate form of the frequency shift is

$$\Delta f = \frac{1}{2\pi} \sqrt{\frac{k}{m + \Delta m}} - f_0 \tag{3.6}$$

In our application, we are only interested in the regime where the assumption of

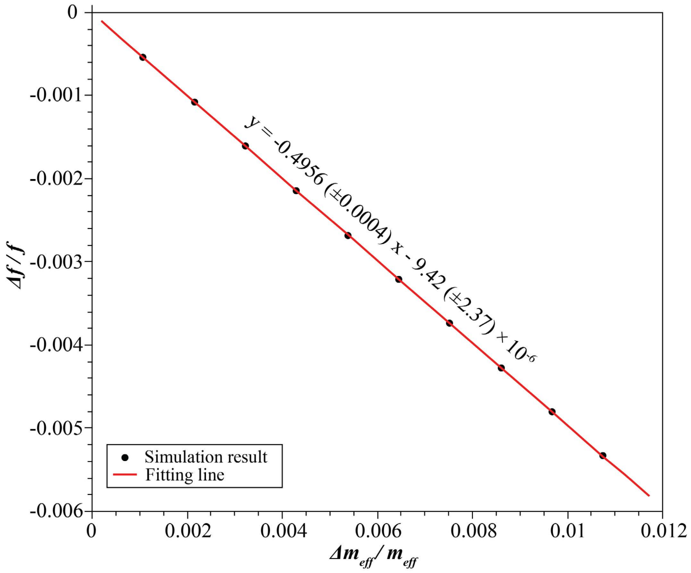

Figure 3·2: The simulation of mass loading effect on the mass sensor shows a linear relationship between the frequency shift and change of effective mass.

linear dependency offers adequate accuracy.

3.3 Driving and sensing the mass sensor

The MEMS mass sensor is capacitively driven and sensed. When applying a voltage across the two plates of the resonator, the equation of motion for the oscillating plate can be written as

$$\ddot{x} + \gamma \dot{x} + \frac{k}{m} x = \frac{1}{2m} \frac{\mathrm{d}C}{\mathrm{d}x} V^2 \tag{3.7}$$

For small amplitude oscillation, the capacitance of the resonator can be approximated as

$$C = C_0 + C' x + C'' x^2 \tag{3.8}$$

where C_0 is the capacitance at the equilibrium position while C' and C'' are the first and second derivatives of the capacitance evaluated at the equilibrium position. The driving voltage is a superposition of AC and DC signals, so by plugging equation Equation 3.8 into the equation of motion, one can get

$$\ddot{x} + \gamma\dot{x} + \frac{k}{m}x = \frac{1}{2m}(C' + 2C''x)(V_{dc} + v_{ac})^2 \tag{3.9}$$

Since the amplitude of the AC signal v_{ac} is much smaller than the DC bias V_{dc}, to a first order approximation, Equation 3.9 can be simplified as

$$\ddot{x} + \gamma\dot{x} + (\frac{k}{m} - \frac{C''V_{dc}^2}{m})x = \frac{1}{2m}C'V_{dc}^2 + \frac{1}{m}C'V_{dc}v_{ac} \tag{3.10}$$

For a harmonic excitation $v_{ac} = v_i \cdot \cos\omega t$, by redefining the equilibrium position of x, this equation can be solved and the solution is

$$x(t) = A(\omega)\cos(\omega t + \phi(\omega)) \tag{3.11}$$

with

$$A(\omega) = \frac{\frac{1}{m}C'V_{dc}v_i}{\sqrt{(\omega^2 - \omega_0^2)^2 + \gamma^2\omega^2}}, \tag{3.12}$$

$$\omega_0^2 = \frac{k}{m} - \frac{C''V_{dc}^2}{m} \tag{3.13}$$

and

$$\phi(\omega) = \arctan\frac{\gamma\omega}{\omega_0^2 - \omega^2} \tag{3.14}$$

The oscillation is sensed by detecting the current flowing from the static plate

$$i = -\frac{\mathrm{d}Q}{\mathrm{d}t} = -\frac{\mathrm{d}[(C_0 + C'x + C''x^2)(V_{dc} + v_{ac})]}{\mathrm{d}t} \approx -V_{dc}C'\frac{\mathrm{d}x}{\mathrm{d}t} - C_0\frac{\mathrm{d}v_{ac}}{\mathrm{d}t} \tag{3.15}$$

The second term has an amplitude linearly dependent on ω, while the first term depends strongly on ω near ω_0

$$i = \frac{\frac{1}{m}(C'V_{dc})^2 v_i\omega}{\sqrt{(\omega^2 - \omega_0^2)^2 + \gamma^2\omega^2}}\sin(\omega t + \phi(\omega)) + C_0 v_i\omega\sin\omega t \tag{3.16}$$

which indicates that the current has a Lorentzian line shape for a frequency sweep near ω_0, after subtracting out the background term $C_0 v_i\omega\sin\omega t$.

3.4 Circuit setup for resonance frequency tracking

In order to monitor the atomic flux during an experiment, the resonance frequency is continuously monitored. To this end, a self-oscillating circuit was built using a SR 124A lock-in amplifier to complete the phase-locked loop. The circuit diagram is shown in Figure 3·3. The lock-in amplifier uses a reference channel to lock onto the external signal, and outputs a sinusoidal signal with the same frequency as the reference. The output signal is used to drive the resonator and the signal sensed on the ground plate of the resonator is sent back to the lock-in amplifier to form a closed resonating loop. The AC amplitude, phase and DC bias of the output signal can be set to desired values on the front panel. A frequency counter is used to measure the resulting closed loop resonance. The averaging time for frequency counting is 0.5 seconds, followed by 0.5 seconds of data communication and processing time.

Such a system can work as either an open loop setup using a waveform generator as the frequency source or closed loop to form a self-oscillating circuit. With the open loop setup, the resonator can be characterized by performing a frequency sweep to get

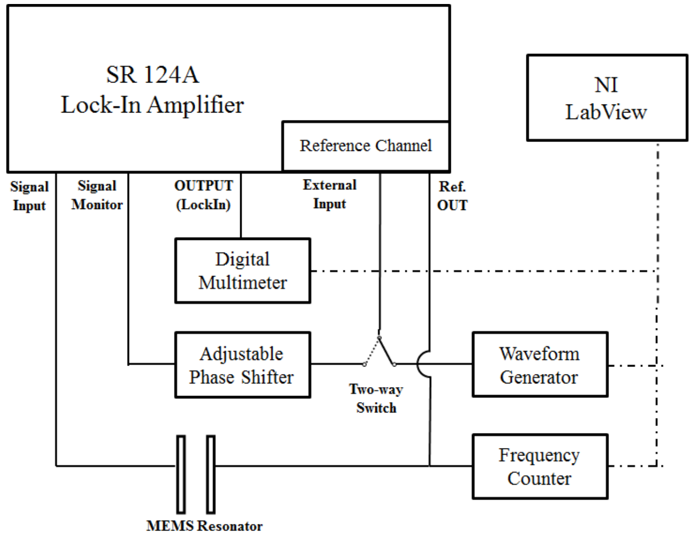

Figure 3·3: The diagram of a MEMS resonator self-oscillating circuit. A lock-in amplifier is used to phase lock the resonator so that an electrical oscillation with the same frequency as the resonator is kept inside the loop.

the Lorentzian response. Figure 3·4 shows the plot of such a sweep. In the sweep, the driving voltage is set to 10 mV with a DC bias of 500 mV. The y-axis is the amplified current sensed on the ground plate of the resonator with the sensitivity of the lock-in amplifier set to 1 nA. For a harmonic oscillator with a damping proportional to the velocity, the oscillation amplitude should have a Lorentzian line shape according to the discussion in section 3.3 and Equation 3.16

$$u(f) = \frac{\frac{u_{max} \cdot f_0}{Q} f}{\sqrt{(f^2 - f_0^2)^2 + (\frac{f \cdot f_0}{Q})^2}} \tag{3.17}$$

where $u(f)$ is the oscillation amplitude depending on frequency; u_{max} is the oscillation amplitude at resonance; f_0 is the resonant frequency; Q is the quality factor, which describes the width of the resonance peak. A curve fitting using this equation has been applied to the sweep data. The fit gives $f_0 = (85\,080.664 \pm 0.013)\,\mathrm{Hz}$ and

$Q = 26442 \pm 258$.

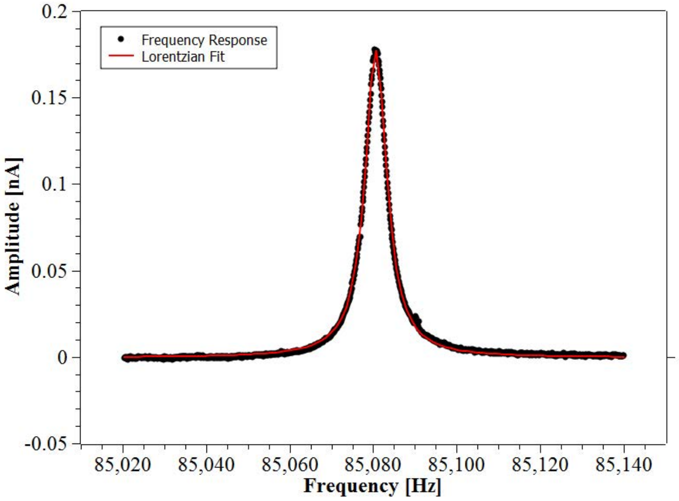

Figure 3·4: The Lorentzian response of an 85 kHz resonator. The Q-factor of this resonator is around 26K.

For a closed loop oscillation, the oscillating frequency in the loop will be locked to the resonant frequency. In a mass loading experiment, the resonant frequency shifts due to the mass change, and the oscillating frequency will shift as well to follow the resonant frequency at all times. By reading the frequency counter, the added mass can be easily calculated using Equation 3.5 or the calibration data obtained from a macroscopic film thickness monitor typically used in thin film deposition systems. For such a phase-locked state, the typical AC driving voltage is 10 to 20 mV, with a DC bias voltage of 100 to 1000 mV for a 85 kHz mass sensor.

3.5 Calibration and sensitivity of the mass sensor

The mass sensor is calibrated in a standard thermal evaporator. Using a conventional crystal thickness monitor the deposition is recorded independently of mass sensor's frequency shift. The crystal sensor is placed beside the MEMS mass sensor to ensure that they receive the same thickness of deposition. The results are plotted in Figure 3·5. For the mass loading, it is found that $\Delta f/\Delta m = (201.1 \pm 0.1)\,\mathrm{Hz/ng}$. The metal deposition will also change the temperature of the MEMS device and introduce a frequency shift due to the change in the Young's modulus. (Kim et al., 2007) To take this effect into account, the temperature is cycled without adding mass. The temperature dependence of $(-1.814\,37 \pm 0.000\,08)\,\mathrm{Hz/K}$, plotted in Figure 3·5 c), is used to subtract out thermal effects by measuring changes in temperature during evaporations. This function can also be accomplished using on-chip silicon thermometers. While the relative change in mass can be determined with high precision, the absolute mass accuracy is limited by the calibration accuracy, which is on the order of 1%.

The advantage of self-oscillating phase-locked-loop is that it provides an extremely precise real-time measurement of resonant frequency, which depends on the mass loading. The resolution and precision of this measuring system is determined by the stability of the measured frequency that can be quantified. Allan deviation is a widely used two-sample deviation to evaluate the frequency stability of oscillators. (Allan, 2005)

$$\sigma_f(\tau) = \sqrt{\frac{1}{2N}\sum_{n=1}^{n\to\infty}\left(\overline{f}_{n+1} - \overline{f}_n\right)^2} \tag{3.18}$$

where τ is the averaging time for each measurement; $\overline{f}_n$ is the average value of the n-th measurement. Also the definition of Allan deviation is based on measurements which have no wait time between them. Since, in our current setup, a wait time is used for data processing and communication, the Allan deviation is obtained by applying a conversion to eliminate the influence of wait time. (Barnes and Allan, 1990)

The Allan deviation of the mass sensor for different averaging time has also been measured. The result is shown in Figure 3·6. The minimum of Allan deviation occurs

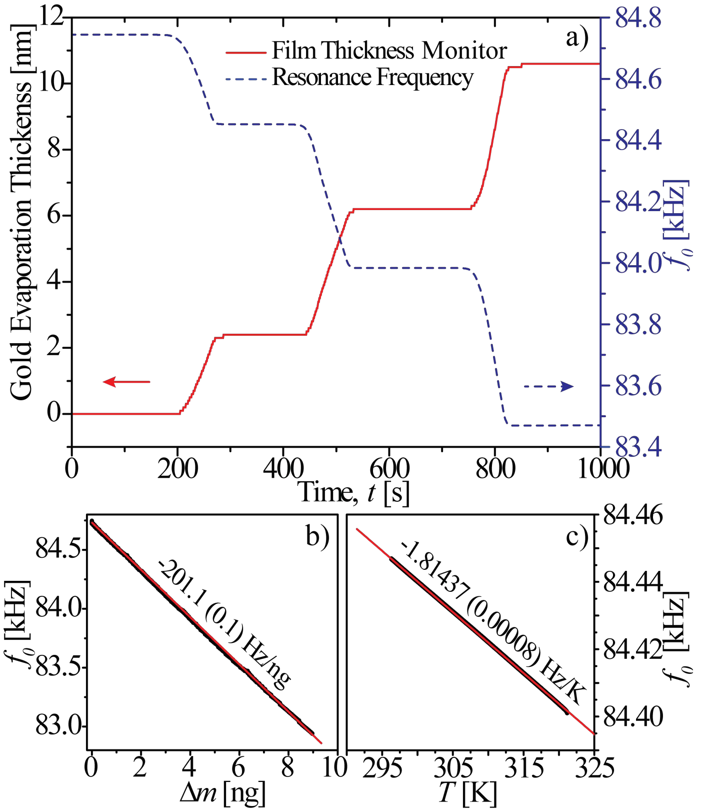

Figure 3·5: a) Calibration of the MEMS mass sensor using a conventional evaporator and film thickness monitor. b) From the slope it is found that a change of 1 mHz in resonance frequency corresponds to approximately 5 fg added mass. c) Temperature calibration reveals a (-1.81437 ± 0.00008) Hz/K linear temperature dependence. Parentheses indicate the standard fitting error.

at $\tau = 10\,\mathrm{s}$. $\sigma_f(\tau = 10\,\mathrm{s}) = 0.717\,\mathrm{mHz}$, which corresponds to a mass resolution of approximately 3.56 fg. However, when using the mass sensor as a film thickness monitor during evaporation, a fast response of the mass change is desired. Hence for our application the averaging time is determined as a balance of both resolution and response time. The averaging time for minimum Allan deviation is usually not practically feasible.

State of the art NEMS devices have reached single atom mass sensitivity. (Jensen et al., 2008) While this level may not be achievable using MEMS structures, it is

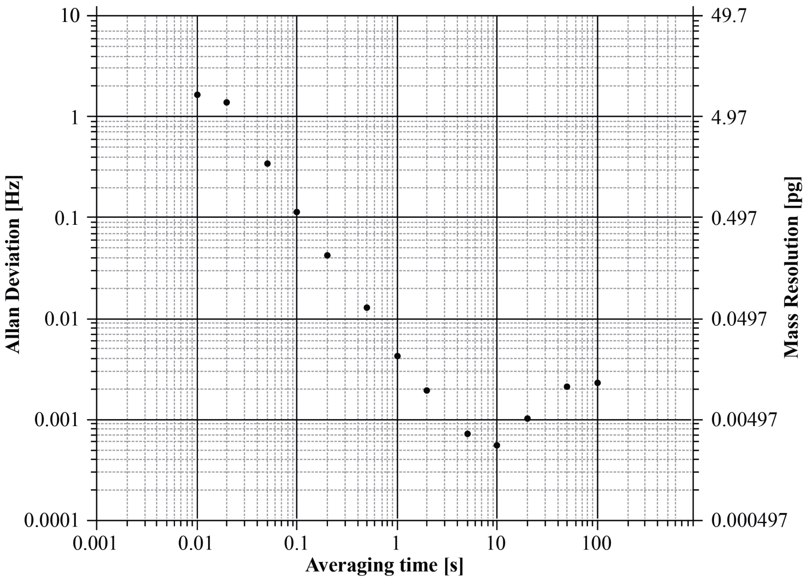

Figure 3·6: The Allan deviation of an 85 kHz mass sensor for different averaging time, demonstrating $\sim 1 : 10^8$ resolution. Minimum Allan deviation ia achieved at an averaging time of 10 s.

believed that there is still room for orders of magnitude improvements resulting in sensitivities on the order of $10^4 - 10^5$ gold atoms. Given that we are targeting evaporation rates of a monolayer per second for our experiments, we currently have ample sensitivity for our experiments. In operation, this device will be used to measure both the evaporation rate and the total number of evaporated atoms emitted by the micro evaporation source which will be introduced in the next chapter. By using the mass sensors in high flux areas and considering geometric factors such as aperture size and distance from the source to the aperture, it will be possible to generate flux and monitor rates of a few atoms per second per aperture, and hence to fabricate structures comprised of single or few atoms. It will also be discussed in the next chapter that even though single mass deposition smaller than 3.56 fg may not be detectable using our mass sensor, by having thousands of identical mass emissions set off sequentially and measuring the total effect on the mass sensor, one can characterize and quantify single mass emission that is much smaller than the resolution of the mass sensor.

Chapter 4

Programmable Solid State Atom Sources for Nanofabrication

4.1 Overview: A micro evaporation source

The inexorable march to smaller feature sizes in devices and systems as described by Moores Law has created a large, international research effort to develop scalable techniques for producing nanoscale structures.(Liddle and Gallatin, 2011)(Moore, 1995) General categories of approaches include nanolithography with a wide range of resist technologies, nano-imprint,(Chou, 1996) AFM/STM,(Xia et al., 1999) and direct write methods such as dip-pen lithography(Zhang et al., 2003) and dynamic stencil lithography(Egger et al., 2005)(Racz et al., 2004)(Vazquez-Mena et al., 2014) including our Atomic Calligraphy technique introduced in chapter 2. In many of these methods, one needs a source providing atoms which get positioned or patterned by these techniques. For example, in Atomic Calligraphy, one uses a MEMS plate with nanoscale apertures which move while a flux of atoms rains down upon the substrate. By moving the plate and aperture, a pattern is written. Sources of atoms with fast response times placed into an array would allow one to start and stop the writing and evaporate different materials simultaneously at different rates while the plate moves. Atom sources are an integral part of the Fab on a Chip concept, which will enable real-time *in-situ* nanofabrication using silicon micromachines.(Imboden et al., 2014a) In this chapter such micro solid state sources of atoms with millisecond response times will be described. At least eight orders of magnitude in mass of a wide range of metals can be deposited controllably. It is shown that one gains many advantages by doing physical vapor deposition at the micron scale.

The source is based on a polysilicon plate suspended by two electrical constriction leads. When resistively heated, the pre-loaded material is thermally evaporated from the plate. While micro sources have been used for thin film and nanoparticle deposition,(Meyer et al., 2011) we show that our further-miniaturized device has a fast thermal response time and requires small amounts of electrical power to reach high temperatures. It can reach high enough power densities to evaporate atoms off the micro-plate while consuming low overall powers, thus keeping both the target and the source substrate cool. Its miniature size also enables one to place many such sources in an array, each one loaded with a different material, building a multi-element evaporator. Furthermore, being compatible with standard MEMS manufacturing process, our devices can be integrated to work with other Fab on a Chip modules including the writer covered in chapter 2 and the mass sensor which is used to weigh the deposited mass and detect the atom emission of the source, as described in chapter 3. We show that our devices can produce atom fluxes with precise control in terms of what, when and how many atoms are being evaporated.

4.2 Device design and operation

The devices are fabricated using the same MEMSCAP PolyMUMPs foundry process as the writer and mass sensor. After the wet etch release step, the devices are then coated with a ∼20 nm thick layer (200 cycles) of Al_2O_3 by Atomic Layer Deposition (ALD). This forms an electrically insulating layer between the polysilicon structure and the material loaded for evaporation. The devices are shown in Figure 4·1. The

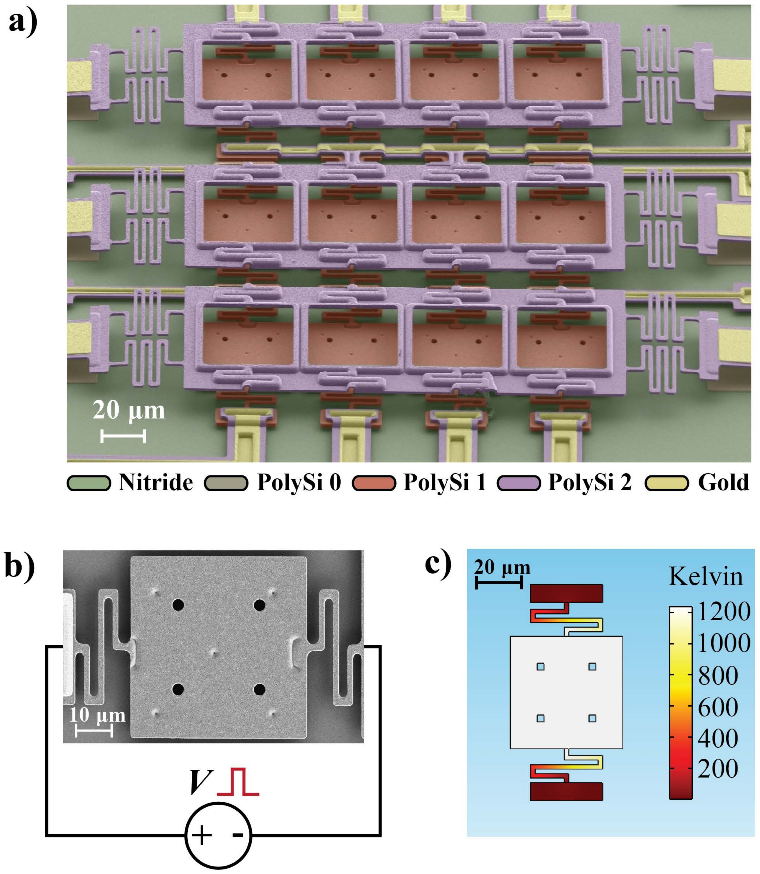

Figure 4·1: a) False-colored SEM image of the source array with springs (red) protected by the integrated shadow mask (purple). Power can be applied to each source element individually, through polysilicon leads coated with gold. b) Each source element consists of a suspended source plate and two spring-shaped constrictions. A bias voltage across the source plate heats the source. c) FEA simulation shows a uniform temperature profile across the source plate.

sources are arranged into arrays of 12 polysilicon plates, each 50 µm × 50 µm in size, 2 µm thick and are suspended 2 µm over the substrate by two 2 µm wide serpentine springs. The typical room temperature resistance of a source element is $\sim 800\,\Omega$, with most of the resistance dominated by the two springs. The source plate can be loaded with material using a conventional PVD process. When a current is applied, the spring acts as a heater, and the device works like a micro hot-plate.(Grabiec et al., 2005) As the center plate reaches certain temperatures, the loaded metal of choice is thermally evaporated. Each plate and heaters form an individual atom source element. Variants can be designed by adjusting the dimensions of the plate and heaters, resulting in different electrical and thermal characteristics. Electrical leads wire the source array to bonding pads in a way that each source element can be accessed independently. Micro polysilicon shadow masks elevated by bimorphs can also be introduced to protect the heaters, as shown in Figure 4·1 a). This feature helps by keeping loaded material off the heaters as is discussed later on.

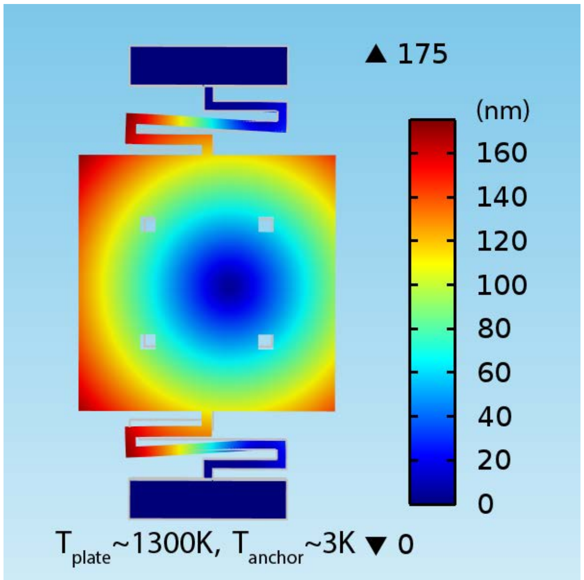

Figure 4·2: Finite element simulation of the mechanical deformation due to thermal expansion of the source. Color scale shows displacement in nanometers with the source plate heated to 1300 K and anchored at 3 K. The deformation in the figure is exaggerated for better visibility. The spring shaped heaters allow the structure to bend, ensuring the mechanical integrity of the device during hundreds of thermal cycles.

The polysilicon heaters are electrical and thermal constrictions and get hot through joule heating when a current is applied. A typical working current is less than 2 mA, with a power less than 10 mW. Thermal energy is added symmetrically by the two heaters until an equilibrium temperature is reached. Heat dissipation is dominated by thermal conduction to the base. Finite element simulations indicate that above 1000 K radiation effects become more and more significant. The $j = \epsilon\sigma T^4$ dependency of thermal radiation density, given by the Stefan-Boltzmann law, improves the temperature uniformity of the plate. Simulations including radiation cooling suggest a 1 K uniformity on a plate heated to 1300 K as shown in Figure 4·1 c). Because of the small powers involved the much larger substrate stays cool even as the springs and plate are hot. When heated, the plate glows like a micro-incandescent source(Mastrangelo et al., 1992) and can be seen with the naked eye. Because of the elevated temperatures, thermal expansion of the plate and springs induces stresses on the heaters. The source deformation caused by thermal stress is simulated and plotted in Figure 4·2. The serpentine design is critical because it relieves these stresses so that each device can be pulsed to high temperatures thousands of times without mechanical failure. This robustness enables us to use continuous voltages for ample mass depositions, as well as short voltage pulses that can deliver controlled amounts of metal atoms at precise times.

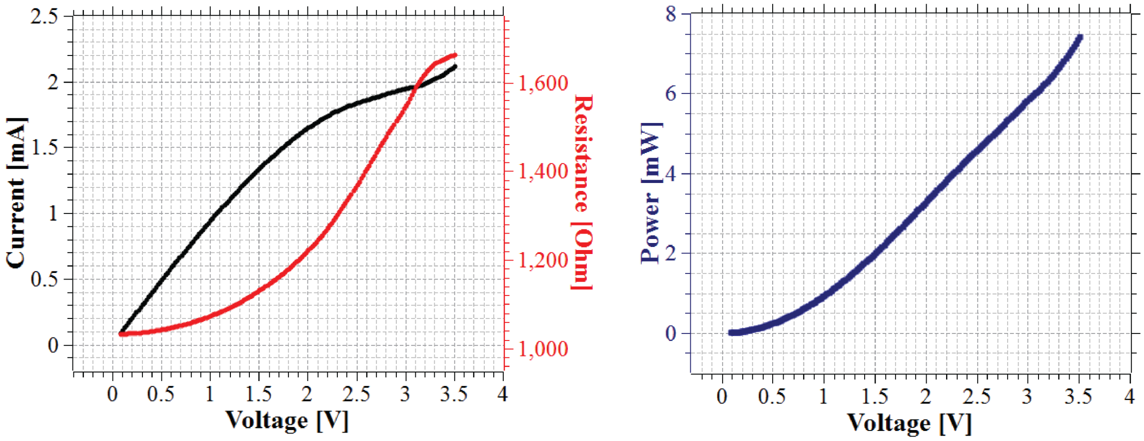

Figure 4·3: Voltage sweep of the unloaded MEMS source. When the voltage exceeds 3 V (point of inflection), the source becomes unstable. This can be explained by thermal breakdown of the polysilicon or other possible causes.(Mastrangelo et al., 1992)

The source is typically operated by applying a constant voltage bias or voltage pulses (see Figure 4·1 b)). The non-Ohmic behavior (increasing resistance with increasing temperature(Geisberger et al., 2003)) favors a voltage bias to prevent run-away heating. The plot of voltage sweep is included in Figure 4·3. Hence a constant voltage constrains the power and a final equilibrium can be reached faster and more reliably than would be the case for current biasing. Figure 4·4 illustrates the devices in operation. Shown are four configurations: All sources turned off (a), voltages applied to all 12 sources in the array (b), voltage on one device (c) and half of the devices biased in a pattern (d). Detailed measurements (discussed later in this chapter) show that the devices have a thermal response time of several milliseconds. This feature gives one precise control over the starting and stopping of atomic evaporations. With the ability to actuate each source of an array individually, a digitally programmable atom source is achieved.

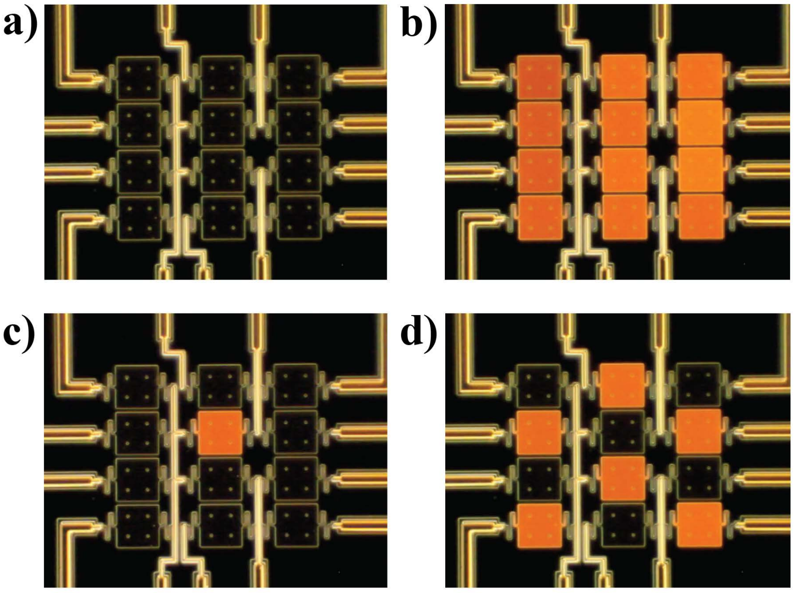

Figure 4·4: Dark-field optical microscopic images of the source array glowing when current is applied. Each source can be actuated independently. Adjacent sources, separated by a few microns are thermally independent.

4.3 Metal evaporation and mass transfer detection

4.3.1 Metal loading and evaporation

The micro hot-plates become atom sources when a material is deposited onto the plates using conventional PVD methods. When heated, films of the material ($\sim 100\,\mathrm{nm}$) are evaporated off of the source. The mass flux coming off the surface of the material is given by Hertz-Knudsen equation(Hołyst and Litniewski, 2009)

$$j = \frac{mP_{vap}\left(T\right)}{\sqrt{2\pi m k_B T}} \tag{4.1}$$

where m is the atomic mass of the material and $P_{vap}\left(T\right)$ is the vapor pressure of the material, depending on its temperature. The theoretical relation between vapor pressure and temperature is described by Clausius-Clapeyron equation(Frost and Kalkwarf, 1953)

$$\ln\left(P_{vap}\right) = A - \left(B/T\right) \tag{4.2}$$

where A and B are empirical constants. This equation indicates that the vapor pressure changes dramatically with a small change in temperature. This provides the foundation of controlling the evaporation rate over several orders of magnitude while still keeping the temperature within a reasonable range.

Shadow masks can be used to only expose selected source plates of an array for material loading in a conventional thermal or e-beam evaporator. Therefore each source plate can be loaded with different material by repeating the PVD and exposing different source plates each time. This procedure prepares a multi-material source array, which would enable multimaterial co-evaporation. Because each source element has independent electrical leads and are thermally decoupled, different materials can be evaporated simultaneously or sequentially, offering great flexibility.

Because only the micro plates get hot while the substrate stays cool, each evaporation only dissipates a few milliwatts of power. These are in essence solid state sources of atoms suitable for materials that have a vapor pressure higher than that of silicon. Because of the low powers needed, we will show that these sources are well suited for low temperature environments. Furthermore, the total power can be constrained by pulsing the source. This lets one have the ability to quench condense atoms on a sample at low temperatures *in-situ*, without significant heating of the sample.

4.3.2 Metal-silicon reaction prevention

When the source is in operation, the high temperatures cause the silicon to react with the source metal. To prevent this reaction, an inert barrier layer protects the silicon from chemical attacks such as the formation of metallic silicide. Gold, for example, forms an eutectic with silicon at $\sim 636\,\mathrm{K}$,(Okamoto and Massalski, 1983) far below the evaporation temperature. As previously mentioned we use a $\sim 20\,\mathrm{nm}$ thick ALD deposited Al_2O_3. The robustness(Miller et al., 2010) of the sapphire film helps to isolate the polysilicon structure from the evaporant both electrically,(Groner, M. D., Elam, J. W., Fabreguette, F. H., & George, 2002) and chemically,(Miller et al., 2010)(Groner, M. D., Elam, J. W., Fabreguette, F. H., & George, 2002) allowing one to use a wider range of elements on the source. Eight different metals have been evaporated, including In, Ag, Au, Cu, Fe, Al, Pb and Sn. No molecular materials have been tested so far, but in principle they should work equally well.

The failure temperature of the atom source is dependent on the loaded material. For example, it has been observed that aluminum will diffuse through Al_2O_3 as temperatures exceed $1200\,\mathrm{K}$(Guha et al., 2002) and react with silicon, resulting in an unstable drifting of the resistance. An e-beam evaporated tungsten coating ($\sim 30\,\mathrm{nm}$)

as barrier layer was also tested for aluminum evaporation. The evaporation rate and source resistance was stable for low power because the silicide-forming reaction of tungsten is minimal below 1000 K.(Kamins, T. I., Laderman, S. S., Coulman, D. J., & Turner, 1986) Failure has occurred on gold and iron for high evaporation temperature as well. Micro-cracking of alumina is a probable failure mechanism.(Baumert et al., 2011) This is shown in Figure 4·5 where bare plates show pitting at high powers. Once the material reaches the polysilicon structure, a eutectic may form, lowering the melting point of the alloy to make the source fail early. The source was heated by 100 ms pulses with each pulse voltage increasing by 10 mV. The silver melted at power of 6.01 mW (as determined by the SEM image) and was all evaporated by the time the source reached a power of 8.31 mW. The pitting is first observed at 8.75 mW. It has been reported that Al_2O_3 fails at 1500 K,(Zhang et al., 2007) a plausible temperature of the source. For sources loaded with gold this pitting leads to catastrophic failure. At the failure temperature the gold is still present and comes in contact with the silicon to form a eutectic. This can be observed for the source actuated with 100 ms $\sim$ 9.0 mW pulses shown in Figure 4·5 b). Faults rapidly grow and failure occurs as the defect reaches the heaters. It is believed that the atom source performance can be further improved by optimizing surface passivation and barrier layers to the source material. For example silicon oxynitride has also been proposed as an effective barrier layer between aluminum and alumina,(Guha et al., 2002) and platinum is a known barrier metal for gold. Optimizing the alumina thickness has also been shown to have a significant effect on the fracture strength of the barrier layer.(Baumert et al., 2011)

Best performance is obtained by placing the source material only on the plates and keeping the heaters clean: (1) a metal film deposited on both heaters and plate may short out the applied current as the resistance of the heater is much greater than that of the metal; (2) material on the heaters also acts as a thermal short, increasing the

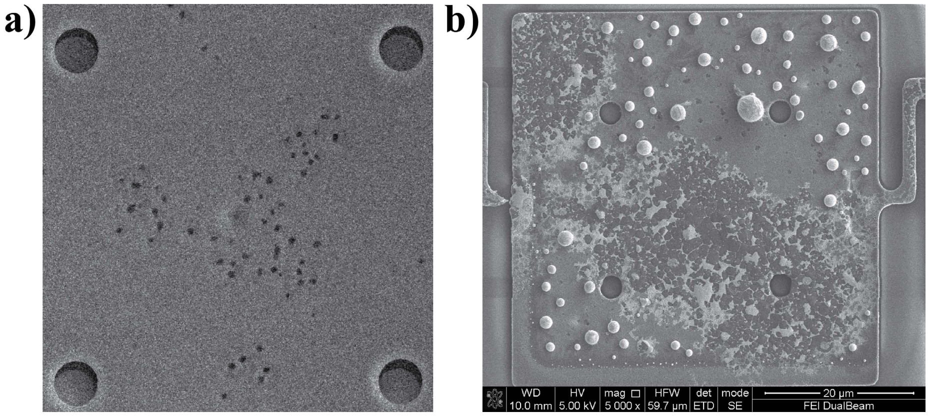

Figure 4·5: At high temperature the Al_2O_3 protection layer may degrade. a) A source plate actuated with 100 ms pulses. The power was slowly ramped up and above 8.75 mW the pitting appeared in the center of the source plate. Such defect will allow material to diffuse into polysilicon thus destroy the source. b) A failed source loaded with gold. When pulsed with high power (~ 9.0 mW) gold made contact with silicon though the defect of Al_2O_3 layer. The alloying can be seen in the SEM image.

power consumption and reducing control as the amount of material changes during an evaporation; (3) It has been observed that the metal-loaded heaters tend to fail at lower powers than the metal-free ones. A possible explanation for the third problem could be the failure of the Al_2O_3 protection layer. As previously studied,(Baumert et al., 2011) the subcritical cracking of alumina due to thermal expansion of the spring may expose the underlying polysilicon to the metal. As the heaters experience the greatest thermal strains, it can be expected that protecting them from chemical attack will enhance the device performance. To solve these problems, an overhanging, self-assembling, shadow mask structure that is elevated $\sim 10\,\mu m$ above the source plate by a set of bimorphs was incorporated. During a PVD procedure to load materials onto the source, the mask keeps the material off of the heaters.

4.3.3 Evaporation monitoring using the mass sensor

To detect the small number of atoms provided by these sources, a special mass detector is required with a resolution orders of magnitude higher than conventional film thickness monitors. The mass sensor we developed and introduced in chapter 3 is suitable for this task. The specific design we used for micro evaporation monitoring has a frequency of $\sim 84\,\mathrm{kHz}$ and a quality factor Q ranging between 10 000 and 250 000 at room temperature, depending on the drive parameters. It is found that at cryogenic temperature the quality factor is even enhanced. During a micro-evaporation the mass transferred from the source to the resonator increases the mass of the oscillating plate and shifts its resonant frequency. The springs of the resonator are covered by a shield to prevent material landing on the springs which would affect the spring stiffness during metal deposition. The deposited mass is calculated using the calibration data as discussed in section 3.5. For the rest of this chapter, all subsequent errors of mass deposition given do not include the systematic error limited by the calibration inaccuracy of the film thickness monitor and are only accurate as relative errors resulting from subsequent measurement uncertainties.

To test the micro-evaporator, the resonator and the loaded source are wire-bonded to two separate ceramic sockets and placed facing each other at a distance of $\sim 1\,\mathrm{mm}$. Mass emitted from the source will impact the resonator, causing a frequency shift that can be continuously monitored, as is the case for standard macroscopic deposition monitors. Such a setup is convenient to study the behavior of the material being thermally evaporated from the source, and was used for most experiments described throughout the rest of this thesis. For example, Figure 4·6 shows the results of the evaporation from 11 sources, each loaded with $\sim 140\,\mathrm{nm}$ of silver. The evaporation was done at room temperature and each source was heated until all metal

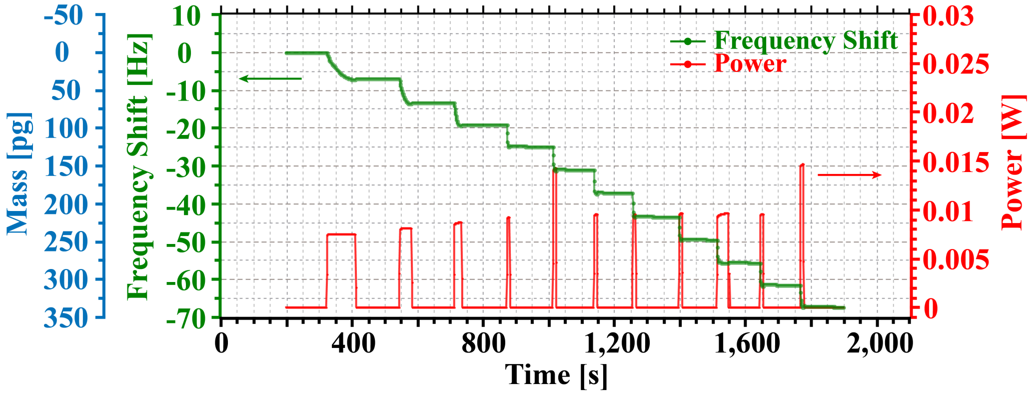

Figure 4·6: Silver evaporation from an array of sources at room temperature. The source was loaded with ∼ 140 nm of silver prior to use. 11 voltage pulses were applied sequentially to the 11 source elements of the array. The pulse duration ranged from 9 to 90 s. A single resonator constantly monitored the mass flux. The total frequency shift was (67.5 ± 0.5) Hz, corresponding to a mass loading of (338 ± 3) pg.

was evaporated. Hence, each frequency step is of roughly equal size. Distribution of individual sources in the array accounts for the small variation of the frequency step, which will be discussed later. From the first four pulses it can be seen that increasing the power produces a higher evaporation rate as a result of the higher plate temperature. Therefore the evaporation rate can be regulated by the applied voltage. For the 5^{th} and 11^{th} pulse the power is so high that all the material is emitted within the integral time of the resonance frequency measurement. The total frequency shift induced by mass loading from all 11 sources was (67.5 ± 0.5) Hz, corresponding to a mass transfer of (338 ± 3) pg.

The atom sources can be actuated using pulse width modulation (PWM) techniques. Due to the exponential term in the Clausius-Clapeyron equation, controlling the evaporation rate by tuning the temperature is difficult (not only is the temperature- power relation non-linear, the evaporation flux is exponentially dependent on the reciprocal of temperature). To obtain a linear control, PWM techniques are used. If the mass transfer of a certain power is well calibrated, one can control the total amount of mass transferred by tuning the width and number of pulses. This effectively linearizes the control of the sources. Furthermore, by adjusting the duty cycle, the time-averaged power generation is well constrained and the system is ensured to return to equilibrium after each pulse. The above operation is based on the assumption that the pulse width is significantly longer than the thermal response time of the source. If not, the source will no longer be able to reach equilibrium during the pulse. For short-pulse mode, one can overdrive the source with very high power which will generate a short hot spot and induce a burst of mass emission. According to Equation 4.1 and Equation 4.2, a slightly higher temperature will induce a much faster evaporation rate. Hence the power consumption per emitted atom will be low, minimizing unwanted heating to the system. This non-equilibrium pulsing is in the non-linear regime and the emitted mass will no longer be proportional to the pulse width. This effect can be seen in Figure 4·8 b).

Shown in Figure 4·7 a) and b) are such experiments done at low temperatures ($\sim 3\,\mathrm{K}$) in a specially designed, closed cycle, low vibration cryostat. Low temperatures improve the Q factor of the resonator and enhance its sensitivity. In Figure 4·7 a) the mass transfer from five power pulses on a single source element are depicted. Each pulse has an amplitude of $6.36\,\mathrm{mW}$ and a width of $100\,\mathrm{ms}$, causing a $(21 \pm 1)\,\mathrm{mHz}$ shift in frequency for a mass transfer of $(105 \pm 5)\,\mathrm{fg}$ per pulse. The measurement showed that the resistance and power remain constant during each pulse, and the small variations on mass transfer are believed to be caused by the projected surface area shrinking effect, which will be discussed in subsection 4.4.4. The overshoot seen in the frequency shift after each pulse (as shown in the inset of Figure 4·7 a)) may be explained by heating of the resonator due to the power pulse. There are three main energy transfer mechanisms: (1) the kinetic energy from the emitted atoms ($\frac{3}{2}Nk_BT$,

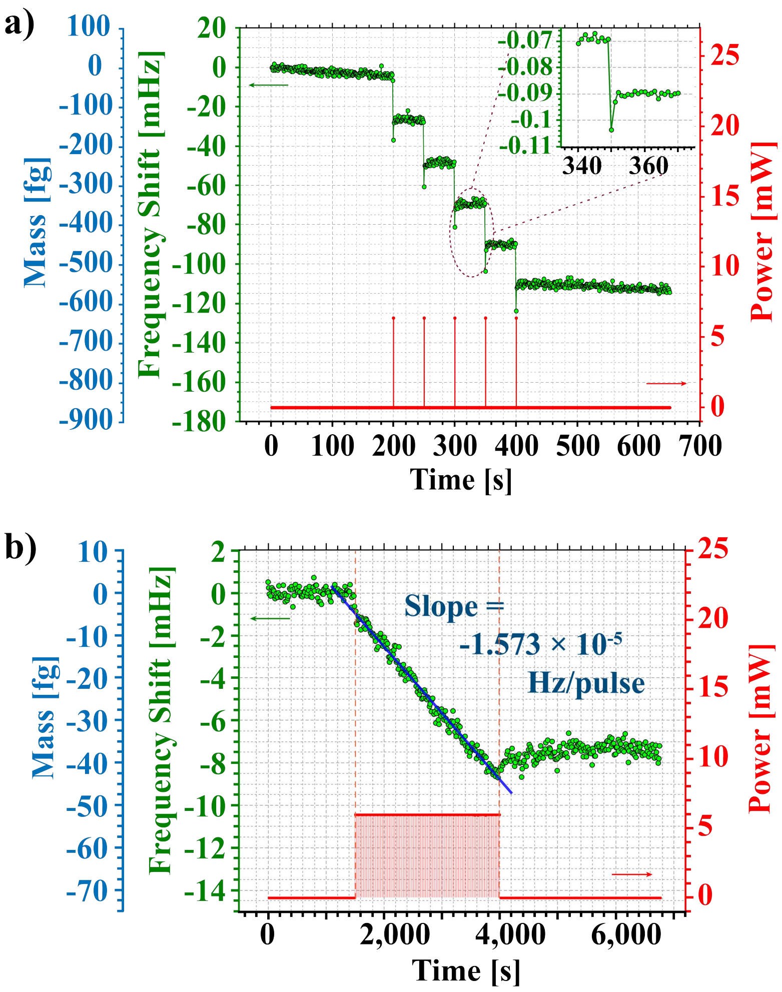

Figure 4·7: a) Indium evaporation in a cryostat at low temperatures ($\sim 3\,\mathrm{K}$). The source was loaded with $\sim 120\,\mathrm{nm}$ of indium prior to use. Five pulses of 6.36 mW, each lasting 100 ms followed by a 50 second wait time resulted in five bursts of atoms. Each mass transfer corresponded to a $(21 \pm 1)\,\mathrm{mHz}$ frequency shift or $(105 \pm 5)\,\mathrm{fg}$ of indium deposited on the resonator. The inset shows the details of a frequency step. b) By pulsing the source many times and measuring the cumulative effect of mass loading, lower deposition rates, below the resonators resolution can be detected. Shown here is the frequency shift (after background subtraction) resulting from 500 pulses, each 6.0 mW lasting 10 ms. The wait time between each pulse is 5 s. The linear fit of $(-1.573 \pm 0.107) \times 10^{-5}$ Hz per pulse corresponds to a mass transfer of (0.079 ± 0.006) fg per pulse.

k_B is the Boltzmann constant, N is the total number of emitting atoms, T is the temperature of the evaporant), on the order of 10^{-7} J, (2) the black body radiation energy ($\int A\epsilon\sigma T^4\,\mathrm{d}t$, σ is the Stefan-Boltzmann constant, ϵ is the emissivity, A is the area of the source), on the order of 10^{-5} J, (3) the rest of the power which heats the whole packaging through thermal conduction, on the order of 10^{-3} J. Measurements (not shown) suggest that the temperature spike of the resonator never exceeds $\sim 2\,\mathrm{K}$ (averaging over the response time of the resonator).

For smaller mass transfers, shorter pulses or lower powers are required. Due to the thermal coupling and associated drift of the mass sensor with the source, best results have been obtained by reducing the pulse time and increasing the applied power. The exponential atom flux given by the Hertz-Knudsen equation favors short, high power pulses to maximize mass transfer while minimizing the heat transferred to the sensor. For such very small mass pulses, the noise in the resonator is such that we can no longer detect individual pulses. However, by using a large number of repeated pulses and detecting the cumulative change, one can deduce the mass transfer of a single pulse. Figure 4·7 b) shows the frequency shift during 500 pulses, each 6.0 mW, 10 ms long and 5 s apart. Due to the long duty cycle the time-averaged power is 12 µW, far less than needed to raise the temperature of the cryostat. The total frequency shift for 500 pulses was (7.86 ± 0.54) mHz. A fit shows that the frequency shift exhibits high linearity during 500 pulses, therefore it can be estimated that for each pulse the deposition on the resonator is (0.079 ± 0.006) fg, which is equivalent to $4.14 \pm 0.32 \times 10^5$ indium atoms deposited on the mass sensors 172 µm × 172 µm sensing plate. These atoms land on the surface at random locations with a surface density on the order of ten atoms per square micron. From a statistical point of view, at the above deposition density, a 300 nm × 300 nm area will have one atom on average deposited for each pulse. Hence when a MEMS writer plate with submicron apertures is present, single atom deposition at a desired location is stochastically achieved. Figure 4·8 summarizes the mass transfers measured for different materials, evaporation parameters and the total mass deposited. Table 4.1 lists parameters of various evaporations. Two data points on the top-right of Figure 4·8 a) represent the mass transferred from 11 sources of an array, with a total mass loading of (916 ± 4) pg, demonstrating the maximum material deposition available using this particular array. The data point on the lower-left is the mass loading of (0.079 ± 0.006) fg from a single 10 ms pulse, which is the smallest that we have measured so far. This demonstrates that such a source array can controllably "puff off" atoms over a seven orders of magnitude. Based on various applications, we have a selection of devices (not shown) with sizes ranging from 10 µm × 10 µm single source to an array of 128 100 µm × 100 µm sources covering an entire 2.5 mm × 2.5 mm die. An array of 36 100 µm × 100 µm sources loaded with $\sim$ 500 nm of Pb has been evaporated to depletion, resulting in a total frequency shift exceeding 2 kHz for the mass sensor, corresponding to a $\sim$ 30 nm thick film, which is an order of magnitude more than the deposition from a typical 12 50 µm × 50 µm source array.

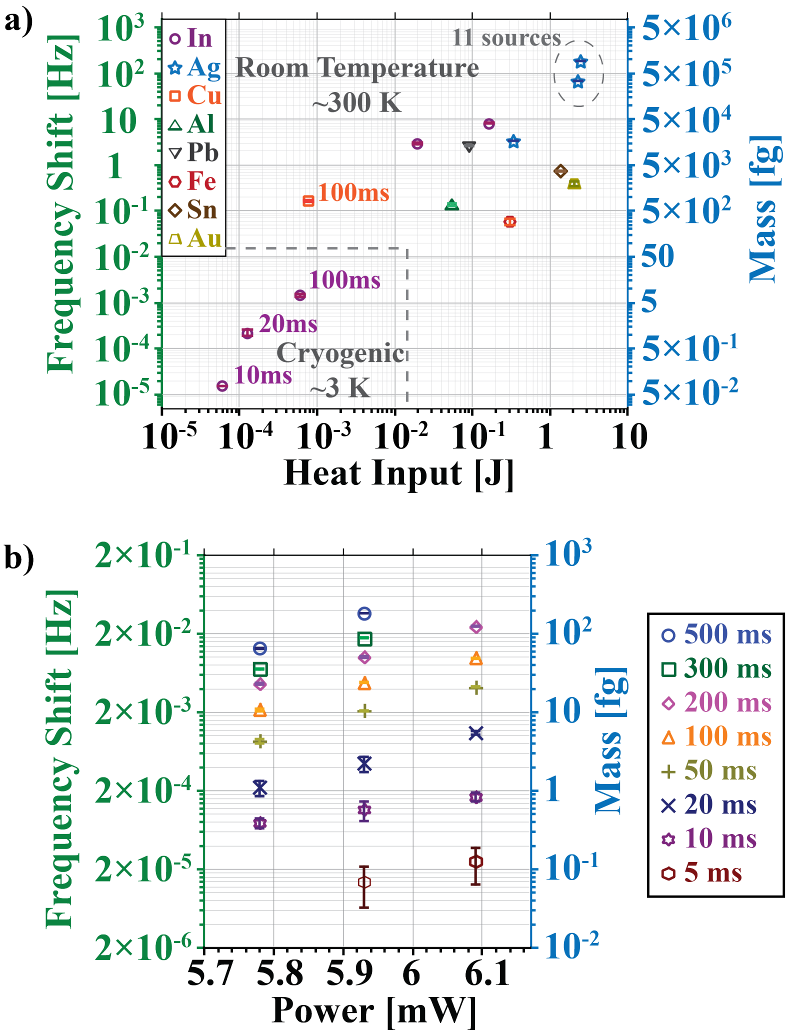

Figure 4·8: A summary of representative evaporations using the 50 µm × 50 µm sources, showing the seven orders of magnitude mass deposition range we have measured. a) The mass loading on the resonator *versus* the total heat generated on the source is plotted. The power was either precisely pulsed (with its width noted beside the data point), or remained on until the source was depleted. b) The plot shows the evaporation of indium when pulsed with different widths and voltages at cryogenic temperature (∼ 3 K). For faster pulses (width shorter than 50 ms) of same power the mass flux does not scale linearly with pulse width. This is a result of the thermal response time of the sources being comparable to the pulse widths.

Metal	Metal Thickness [nm]	Source Thickness [µm]	Base Temperature [K]	Pulsed Power [mW]	Pulse Width [ms]	Source Resistance (during pulse) [Ω]	Heat Input [J]	Frequency Shift [mHz]
Ag	60	1.5	300	6.39	52 000	3175	332	3340 ± 33
Pb	120	1.5	300	3.10	29 000	1289	90.0	2630 ± 70
Au	100	2.0	300	4.69	436 000	1350	2020	390 ± 36
Fe	25	2.0	300	4.49	67 000	1507	301	59 ± 9
Al	100	2.0	300	4.10	13 000	1290	53.3	132 ± 6
Cu	50	2.0	300	7.59	100	960	0.759	169 ± 10
Sn	50	1.5	300	2.88	472 000	2167	1360	742 ± 21
In	60	1.5	300	3.84	5000	2662	19.2	2945 ± 75
In	150	1.5	300	3.04	53 000	3370	161	8099 ± 123
In	120	1.5	3	5.98	10	1931	0.0598	0.0157 ± 0.0011
In	120	1.5	3	5.79	20	1997	0.116	0.221 ± 0.048
In	120	1.5	3	6.01	100	2036	0.601	1.39 ± 0.08

Table 4.1: Parameters of typical evaporations of different materials, using the 50 µm × 50 µm sources. Two variations of the source with the plate on either POLY1 or POLY2 were used. The data is also plotted in Figure 4·8.

4.4 Thermal transient properties and emission geometry

4.4.1 Thermal response during a pulse

In order to better understand the thermal response of the source during a pulse, the transient heating curve of the source was measured. For a 100 ms voltage pulse, the actual output voltage and corresponding current across the source were measured every 10 µs. Given that the polysilicon resistivity monotonically increases with temperature,(Geisberger et al., 2003) the ramp up speed of the resistance reflects how fast the temperature can respond to a pulse. Such a measurement shows that the settling time, *i.e.* the $10\% - 90\%$ rise time, for a typical pulse is less than 5 ms. The effect of the settling time can be seen in Figure 4·8 b), where, for shorter pulses (less than 50 ms), the evaporated mass does not scale with the pulse width because the source never reaches its equilibrium temperature during a short pulse. The heating curve is also affected by the thermal properties of the loaded material, which adds to the heat capacity of the system. Moreover, if the final source temperature is above the melting point, the phase transition of melting will consume some input power to account for the latent heat. Given that the temperature of a material will stay constant when the phase transition is taking place, one can expect a short duration of constant temperature, which is equal to the melting point of the loaded material, on the rising and falling edge of the pulse. This phase transition has been observed in both simulations and experiments, which will be discussed in detail in subsection 4.4.2. Figure 4·9 shows the resistance measurements during a pulse of a source loaded with silver. Details of the rising edge are plotted in the inset. What can be seen is a flat segment that delays the exponential thermal relaxation to the steady state of the system. The segment has a duration of 10.07 ms, and is the result of phase transition during which the temperature remains at the melting point of silver

(1235 K). This adds a calibration point that can be used to estimate the working temperature of the source plate based on its resistance.

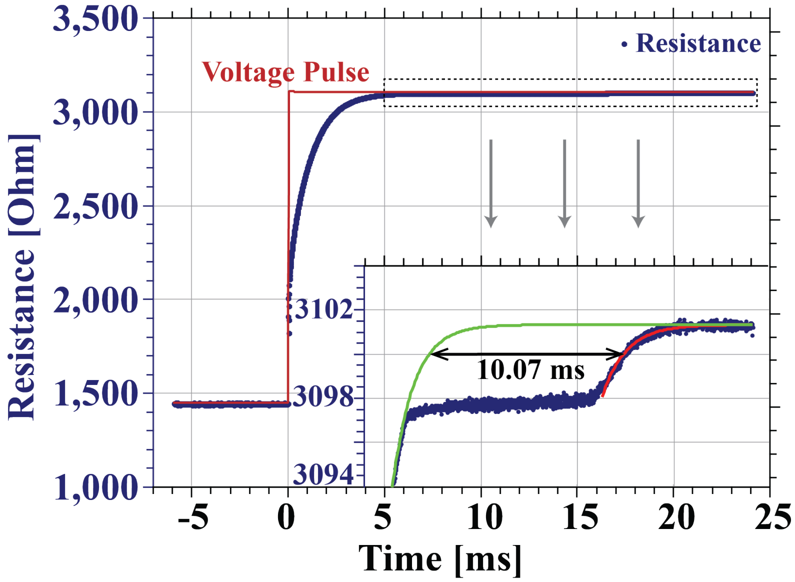

Figure 4·9: Shown is the real-time resistance measurement of a source loaded with silver, on the rising edge of a 100 ms, 6.73 V pulse. The resistance exponentially approaches the equilibrium value as the source thermalizes. The two exponential fit curves (in green and red) demonstrate the thermalization of the source plate before and after the melting. The flat segment shown in the inset has duration of 10.07 ms, corresponding to time during which the material is melting. During this time the power difference between joule heating and dissipation is consumed by the latent heat of silver.

4.4.2 Using the micro source as a calorimeter

The resistance measurement on the source during a pulse provides important information about the thermal properties of the source and the material on it. When the source is being pulsed, heat is generated in the heaters and flows to the source plate. The elevated temperature will cause an increase in the resistance, described in (Mastrangelo et al., 1992). For a voltage biased system the rising resistance will reduce the power, where a current bias may lead to runaway heating. Eventually, the source will reach equilibrium and the temperature and resistance remain constant, as the power generated from joule heating is equal to the total heat dissipation through radiation and thermal conduction to the anchor. Given the fact that the resistance monotonically increases with temperature (within the range we are interested in), the resistance can be used as a scale of the temperature. By pulsing the source many times with different voltages, one can map out the relationship between equilibrium power and resistance. The heat dissipation at a given resistance can then be extrapolated from the measured power-resistance data. The power-resistance relation is plotted in Figure 4·10 and a linear fitting describes the relationship well within the range we care about. As discussed in the previous subsection, the silver melting effect emerges when the pulsed voltage reaches around 6.7 V. Figure 4·11 plotted the resistance on the rising edges of three different voltages pulses. What can be seen is that for 6680 mV there is no melting-induced resistance plateau on the curve, while for slightly higher pulses at 6730 mV and 6780 mV the plateau appears. For the two higher voltage pulses, the power is sufficient for the source to reach the melting temperature of the loaded silver. As it melts the material will consume heat and undergo a phase transition (this is the latent heat of melting). This power drain will prevent the temperature of the whole source plate from increasing, until the melting is completed. After the melting procedure finished, the resistance will resume ramping up until equilibrium is reached. The total thermal energy absorbed by the silver is equal to the product of its mass and its latent heat per unit mass. This must be equal to the time integral of power difference between heat generated from joule heating (power in) and the heat dissipation (power out) which can be estimated from the source resistance using the fitting line in Figure 4·10.

$$P_{Ag} = P_{joule} - P_{dissipation} = \frac{V_{pulse}^2}{R} - P_{dissipation}\left(R\right) \tag{4.3}$$

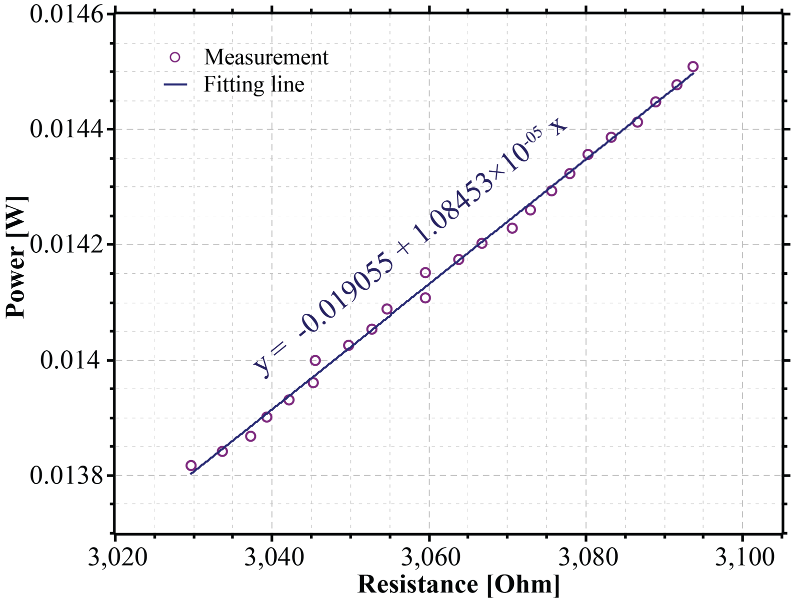

Figure 4·10: Measured power-resistance data at equilibrium, when the applied power is equal to total dissipation. A fit suggests an empirical linear relationship between heat dissipation and source resistance.

where P_{Ag} is the power consumption of silver melting. Once melting finishes and the equilibrium is established again, the heating power will be equal to the dissipation:

$$P_{dissipation}\left(R_{eq}\right) = \frac{V_{pulse}^2}{R_{eq}} \tag{4.4}$$

Recalling that the dissipation is linearly related to the resistance, this will lead to:

$$P_{Ag} = V_{pulse}^2\left(\frac{1}{R} - \frac{1}{R_{eq}}\right) + b\left(R_{eq} - R\right) \tag{4.5}$$

where b is the slope of the linear fit on the heat dissipation data in Figure 4·10, and $b \approx (1.08 \pm 0.01) \times 10^{-5}\,\mathrm{W}/\Omega$. Here we assume that the linear relationship between dissipation and resistance remains during the phase transition of the loaded material because as discussed in subsection 4.3.3 thermal conduction through the polysilicon heaters is the dominated mode of dissipation and will not be affected by the state of

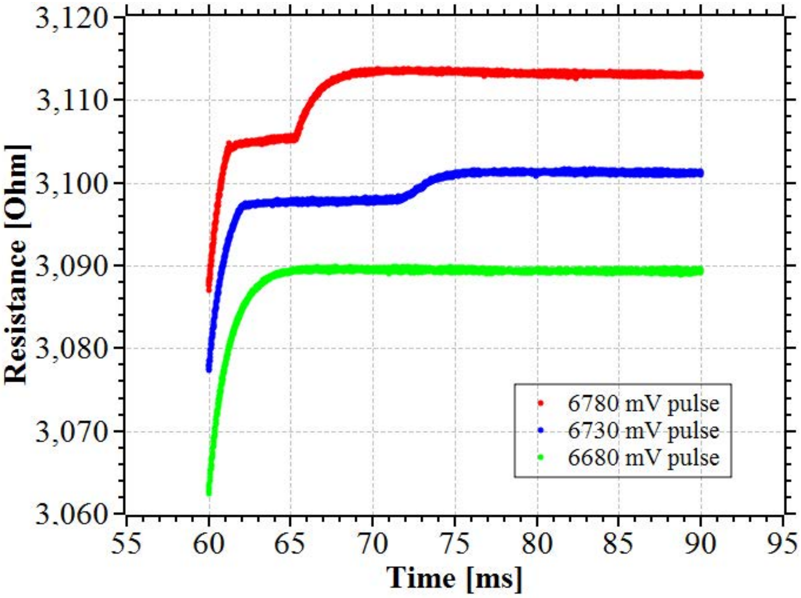

Figure 4·11: Resistance plots on the rising edges of three pulses at different voltages. At 6680 mV no melting is observed, while at 6730 mV and 6780 mV the melting-induced resistance plateau is clearly visible. The 6780 mV pulse has a shorter melting duration since it provides more power that can be consumed by material melting.

loaded material. Therefore, by integrating both sides over time, we get:

$$m_{Ag} Q_{Ag} = \int \left[V_{pulse}^2 \left(\frac{1}{R} - \frac{1}{R_{eq}} \right) + b \left(R_{eq} - R \right) \right] \mathrm{d}t \tag{4.6}$$

Q_{Ag} is the specific latent heat of silver melting. The mass of material m_{Ag} can be calculated based on its thickness and the receiving area of the source plate. The integral on the right can be computed from the resistance data in Figure 4·11. By performing this calculation on the data from 6730 mV pulse, the latent heat is estimated to be (70 ± 20) kJ/kg, in agreement with the accepted value 88 kJ/kg. This result validates the hypothesis of material melting and the discrepancy of the latent heat value can be explained by the uncertainty of the material mass, which is calculated from the film thickness and density. This result also suggests that the source can be used as a micro calorimeter. Compared to a specifically designed micro calorimeter with similar structure,(Poran et al., 2014) our device measures the latent heat of melting without the requirement of a calibrated temperature measurement, by exploiting the observed linear relation between dissipation power and source resistance. The time delay due to the latent heat is only relevant when the final temperature of the source is slightly above the melting point of the material.

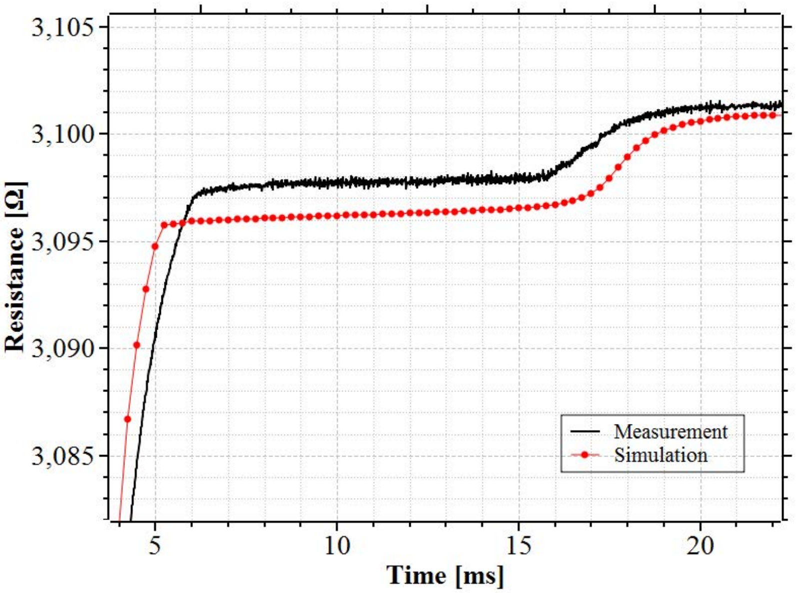

Figure 4·12: The FEM simulation shows a similar constant temperature plateau as in the measurement data. The x-axis for the simulation is shifted to match the time of melting. Before and after the melting time, the resistance exponentially approaches the equilibrium value.

This phenomenon is observed in a FEM simulation as well, which is shown in Figure 4·12. The finite element simulation was matched to the experiment by adjusting the material properties of the polysilicon. As a baseline the following parameters were used: The temperature dependent resistivity was measured by (Imboden et al., 2014a) and (Geisberger et al., 2003), specifically for PolyMUMPs polysilicon; the thermal conductivity was taken from (Geisberger et al., 2003) and (McConnell et al., 2001); (Desai, 1986) and (Okada and Tokumaru, 1984) contain data for the heat capacity and coefficient of thermal expansion of silicon. The temperature range of interest exceeds the range documented in the references, hence for 800 K to 1500 K, the resistivity and thermal conductivity have been extrapolated based on the lower temperature measurements. It is assumed that the heat capacity of silicon is a good approximation to the doped polysilicon used in our experiments, this may not be an accurate assumption as the time axis had to be shifted for the simulation to match the experiment, indicating a higher than expected heat capacity. As measured by MEMSCAP(MEMSCAP,), the electrical conductivity can change considerable from run to run, so it should be assumed that the charge carriers will also affect the thermal conductivity.

Differences between the experimental response and simulations are expected, especially as the material properties are not known very precisely. To match both, the electrical and thermal conductivity were adjusted. The melting point of silver was used as a calibration value. It is known experimentally how much power must be applied to heat the samples. The plateau is an excellent indication of the sample temperature. In order for the simulation and experiment to match, the electrical resistivity was scaled by 5.3% (for all temperature values) and the thermal conductivity was increased by a factor of 1.967. The resulting agreement can be seen in Figure 4·12. The electrical resistivity was scaled so that the simulation and experiment matched at the melting point of silver. The thermal conductivity was matched so that the total thermal energy dissipation matched the power input used in the experiment. The melting time of the silver is very sensitive to these properties, the qualitative agreement is however easily recovered. The correction factor of the electrical resistivity is small and well within the variations expected from the PolyMUMSs fabrication runs. The relatively large correction of the thermal conductivity needed to match the simulations to the data is less easily explained. A possible contribution may be due to the impurities in the polysilicon structure including Al_2O_3 and the deposition material.

4.4.3 Spatial distribution of the mass emission

The spatial distribution of the mass evaporated from the source was also measured, so that the thickness profile of the deposited thin film can be estimated. This can be achieved by varying the detector position and emitting the same amount of material for each point. By evaporating each source element of a uniformly loaded source array to depletion, each evaporation emits the same amount of mass. The in-plane position variation among source elements within the array are ignored because they are small ($< 150\,\mu\text{m}$) compared to the scanning range in x (10 mm) and the gap distance d (1.21 mm). The layout is shown in the inset of Figure 4·13. Measurements were carried out by scanning the resonator parallel to the source plane, to obtain the zenith angle distribution of the deposited mass. The protective shadow mask was removed prior to the evaporation to prevent shielding of the flux. Results are plotted in Figure 4·13, with each data point representing a frequency shift for a completely depleted source. The mass flux from an evaporation source (size of the source $\ll$ distance from the source to the target) has a zenith angle distribution of

$$\Phi = \Phi_0 \cos^m(\theta) \tag{4.7}$$

where Φ_0 is the maximum flux at $\theta = 0$. It can be shown that for a sphere source $m = 0$, while for a flat surface source $m = 1$. Considering the configuration shown in the inset of Figure 4·13, by taking the geometry and the resonator orientation into account, and neglecting the finite size of the resonator ($172\,\mu\text{m} \ll d = 1.21\,\text{mm}$) the frequency shift will have the following form:

$$f = \frac{f_0}{\left(\left(\frac{x - x_0}{d}\right)^2 + 1\right)^{n+1}} \tag{4.8}$$

where $n = 0.5$ for a spherical source and $n = 1$ for a flat surface source. f_0 is the maximum possible frequency shift occurring at $x = x_0$. A fit of this curve to the 11 data points on the plot yields $n = 0.577 \pm 0.001$. The n shows a distribution pattern between sphere model and flat surface model, because the metal films on the sources tend to ball up and form many small islands (will be discussed in the next subsection), which are not exact spherical source or flat surface source. Depending on the material, surface treatment and thermal pulse power, the morphology of the material may be different. For example some material may stay solid and sublime at lower temperature while it melts and then evaporates at higher temperature. Due to the surface tension, solid state and liquid state exhibit very different surface morphology. As a result repeating the above measurement does not yield the same n every time.

4.4.4 Morphology of evaporating metal on the source

The evaporation process has been imaged in real-time using SEM. In such an experiment, the sources were loaded with a desired metal and actuated inside an SEM chamber. The source plates were then pulsed hundreds of times while the SEM took an image after each pulse. Figure 4·14 shows selected images from the data set of a source loaded initially with 150 nm of silver. In this experiment the source element was pulsed 230 times. Pulses started at 1 V and were incremented by 10 mV each time until the maximum pulse amplitude of 3.3 V was reached, by when all source material had evaporated. It can be seen that as the power increases the silver film changed its roughness, then melted and balled up, and eventually evaporated to depletion. In a common setup the target is facing the source with both surface in parallel, and

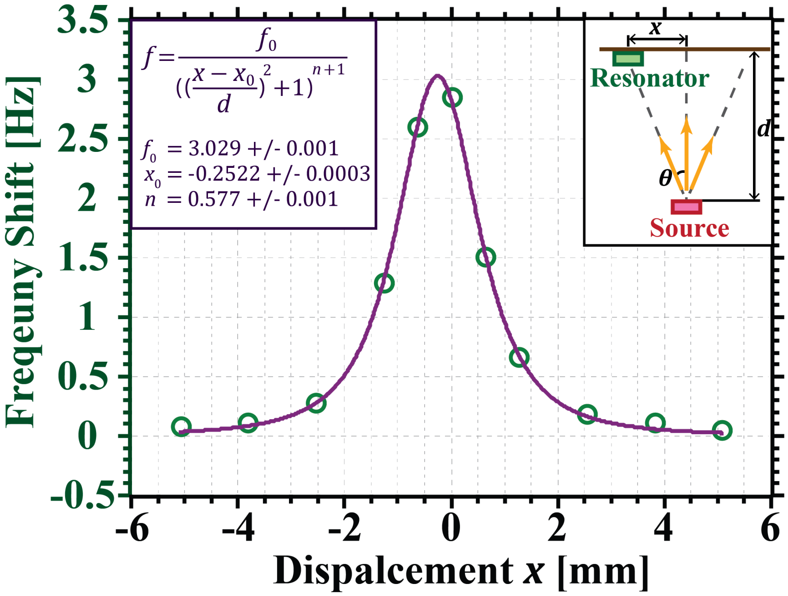

Figure 4·13: The frequency shift measured at different angles, mapping out the distribution of material from a source. Each data point corresponds to equal amount of the material from a single source. The inset shows the configuration of the source and the resonator. The resonator is shifted parallel along the x-axis for each measurement.

the sizes of both target and source are relatively small compared to their distance, so that we only care about the deposition flux in the normal direction of the target plane. The deposition flux on the target is proportional to the projected area of the evaporants surface in the normal direction. As the material gets evaporated off, the morphology changes and the surface area shrinks. This effect can be seen in the SEM images taken as described above. We care about the flux at the normal direction of the target plane, which is proportional to the projected surface area of silver on the 2D plane parallel to the source plate. This is exactly what has been captured in the SEM images.

The projected surface area can be quantitatively estimated by utilizing an image processing algorithm on the SEM images. The evaporant and polysilicon plate have very different contrasts as viewed in an SEM. Hence the sum of gray scale value of each

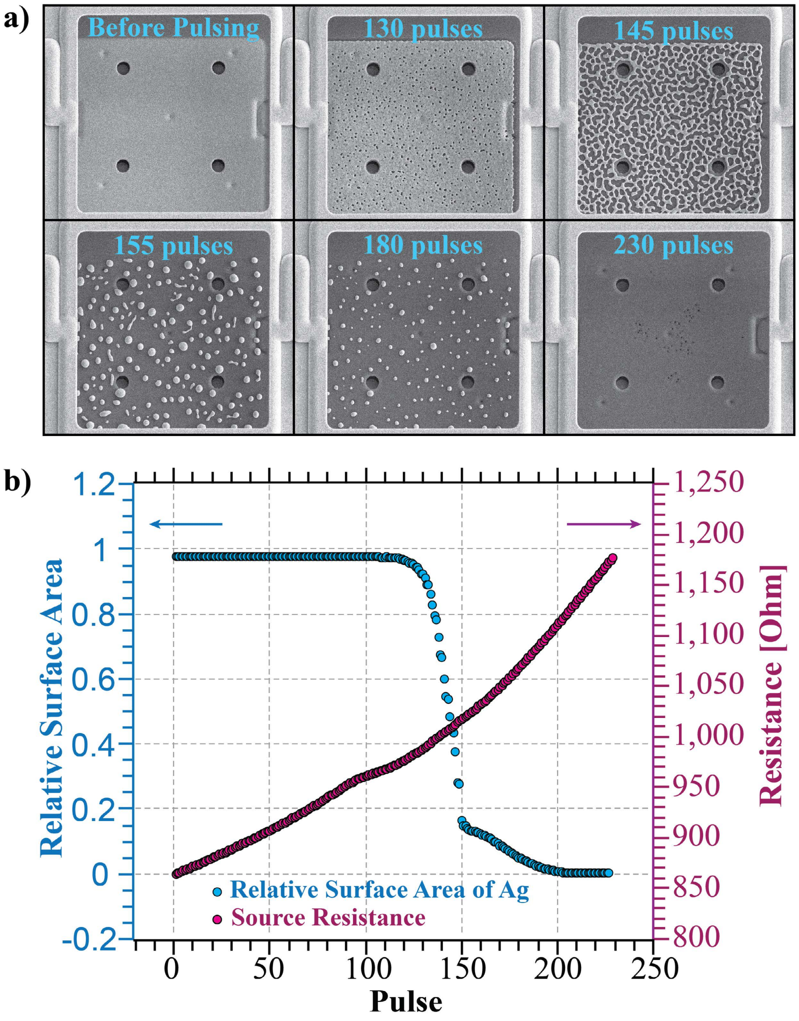

Figure 4·14: A source loaded with 150 nm of silver was pulsed 230 times. Pulse amplitudes were swept from 1 V to 3.3 V in 10 mV increments. a) Six SEM images during the pulses. Before pulsing, the source was covered uniformly with silver. As the pulse power increased silver started to melt and evaporate, resulting in a decrease of projected surface area. Eventually all silver is depleted. b) The resistance of the source increased at higher temperature resulting from higher pulse powers. The projected surface area covered by silver was determined using the intensity of the SEM images and is plotted on the same graph.

pixel within the source plate area provides a measure of how much area of the source plate is covered by metal. Figure 4·15 shows the pixel values of a silver grain and its surrounding area of bare polysilicon source plate. The images contrast and brightness have been adjusted so that metal and polysilicon can be better distinguished. For a given image during the evaporation, the summation over the plate is subtracted by the image of an empty source plate as a background. The value is then normalized to a range from 0 to 1, by setting the first image when entire plate is uniformly covered to be 1. This normalized value can be regarded as a relative projected area of the evaporant. It should be noted again that this measure can only map out the surface area projected on the normal direction, while not counting the area of the curved side wall of the metal grain resulting from dewetting. However, since the target is typically placed facing the normal direction of the source, the projected surface area is an accurate measure to estimate the evaporation flux in this direction. For a constant temperature, the deposition flux in the normal direction of the target plane is proportional to the surface area of the evaporant projected onto that direction.

4.5 Conclusion

We have shown solid state atom sources with potential uses for novel nano-fabrication applications. One can tile a silicon substrate with sources ranging in area from a few square microns to 1 000 000 square microns and have many different materials prepositioned on the sources. Using PWM techniques, one can turn any of the sources on or off at will and control the mass emission over many orders of magnitude. A possible application might be producing nano-alloys with a controllable composition by having two sources with two different materials evaporating simultaneously and adjusting each sources rate independently. The flexibility of having multiple sources working together also enables the fabrication of stacks of monolayers of different materials by alternatively depositing monolayers from different sources. Such a system may allow for nanoscale phase spread studies(He and Ma, 2001) and nanoscale multilayer

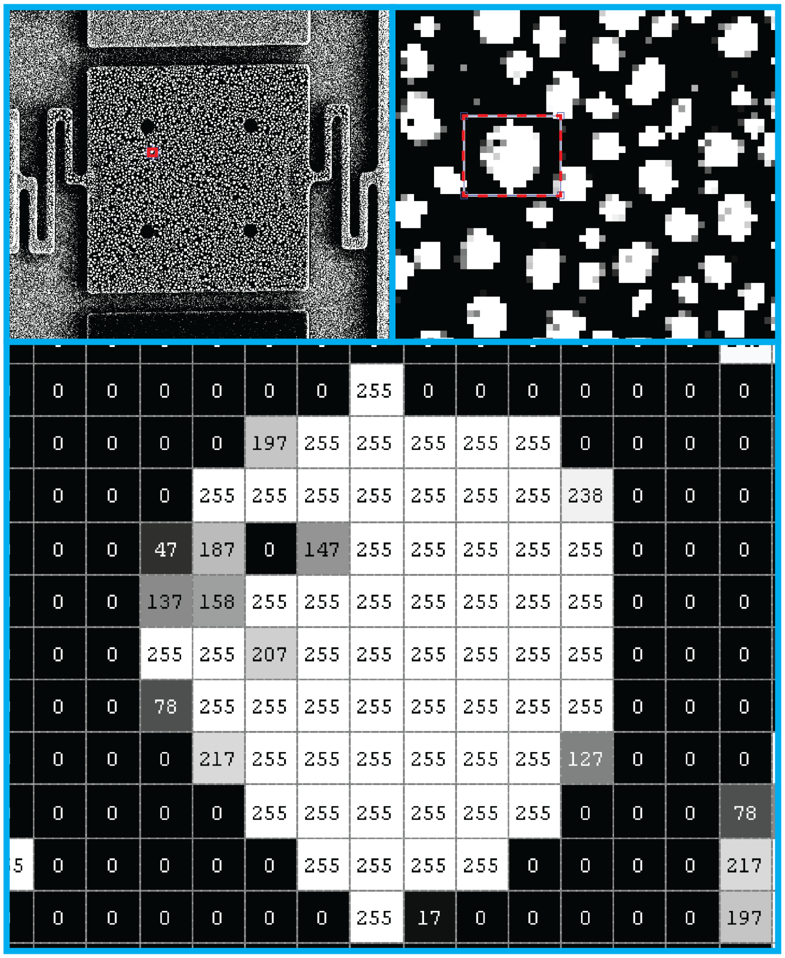

	0	0	0	0	0	0	255	0	0	0	0	0	0	0
	0	0	0	0	197	255	255	255	255	255	0	0	0	0
	0	0	0	255	255	255	255	255	255	255	238	0	0	0
	0	0	47	187	0	147	255	255	255	255	255	0	0	0
	0	0	137	158	255	255	255	255	255	255	255	0	0	0
	0	0	255	255	207	255	255	255	255	255	255	0	0	0
	0	0	78	255	255	255	255	255	255	255	255	0	0	0
	0	0	0	217	255	255	255	255	255	255	127	0	0	0
	0	0	0	0	255	255	255	255	255	255	0	0	0	78
5	0	0	0	0	0	255	255	255	255	0	0	0	0	217
	0	0	0	0	0	0	255	17	0	0	0	0	0	197

Figure 4·15: SEM image of a source evaporating Indium. Upon melting the metal balled up to many small grains and the projected surface area is measured by summing up the pixel values. The bottom figure shows the pixel values are for a very small region containing a single metal grain.

structure research.(Schmitt et al., 1997)

In conclusion, we have described solid state atom sources that let us deposit metals on a target 1 mm away at densities ranging from ten atoms per square micron to over a hundred monolayers, a range of roughly eight orders of magnitude. Since the evaporation rate scales as the plate area, it can be imagined that by placing sources with various sizes together and having a more sensitive mass sensor, controlling the mass deposition over a range of approximately ten orders of magnitude appears feasible. These sources can be used in cooperation with the Atomic Calligraphy technologies, which provide a way to directly pattern the structures as the atoms are being puffed off the plates. With a sub-micron aperture, single atom deposition is feasible. With many apertures in the plates and many sources, arrays of structures can be written in parallel, significantly increasing the throughput of the system. With the Atomic Calligraphy devices, we are in essence doing additive manufacturing at the nanoscale. Moreover, the dimension of the source and its ultra-low power consumption make it suitable to be integrated into a cryogenic system without significantly increasing the base temperature. It will be shown in the next chapter that high-quality quench-condensed thin film with very precise thickness control, which are of great interest to condensed matter physics research, can be fabricated using the micro source. Manufactured in a standardized foundry, these devices can economically and easily be brought into mass production. We believe such sources, with their flexibility and precision, will become powerful tools for nano-fabrication or even nano-manufacturing.

Chapter 5

Quench Condensed Superconducting Thin Films

5.1 Overview: Superconductivity of thin films

Quench-condensed superconducting metallic thin films has been extensively studied. Different metals quench-condensed on various types of substrate usually exhibit quite different film morphologies and transport properties (Haviland et al., 1989)(Danilov et al., 1995). For example, as a well-studied metal, lead (Pb) tends to form granular crystalline islands when quench-condensed on passivated substrate. (Frydman et al., 2002) Those Pb islands have a percolation effect that very thin films are insulating while beyond a certain thickness threshold the film becomes conductive. This is because that when more materials get deposited, the average gap size among Pb islands decreases and conductivity is achieved when grains finally connect. Such an ordered granular film also exhibits different superconductive properties than a disordered or amorphous thin film (Frydman, 2003). In order to obtain ultra-thin uniform disordered films, the vapor deposition method usually requires a special under-layer on the substrate, like a few angstroms of Ge, which has been used to improve the homogeneity of deposited films for decades (Haviland et al., 1989)(Logeeswaran et al., 2009). However, the role of Ge atoms when current is flowing in the superconducting films is not completely clear so it is crucial if quench condensation of continuous and homogeneous superconducting thin films on common passivated substrates like silicon nitride (SiN) can be achieved.

In this chapter, a MEMS approach for quench-condensing superconducting thin films is discussed. It will be shown that by using the micro evaporation sources one gains many advantages over the conventional vapor deposition method. A target die based on the same PolyMUMPs process is designed as a substrate for superconducting thin film deposition and *in-situ* measurement. By assembling the source die and the target die together and mounting them onto a cryostat, one builds a mini cryogenic chamber for ultra-clean quench condensation and *in-situ* transport experiments, which forms a fully functioning Fab-on-a-chip. Superconductive material like lead (Pb) has been deposited using this setup and several experiments are performed on the quench-condensed Pb thin films. Due to the nature that we are conducting quench condensation in a microscopic manner, the continuity and homogeneity of the thin films quench condensed on a passivated substrate have been greatly improved than those obtained using the conventional vapor deposition technique. We will show that our approach outperforms the macroscopic method in many other aspects as well.

5.2 Device: Quench-condensing thin films with the MEMS approach

5.2.1 Micro source array for quench condensation

In chapter 4, the development of a novel microscopic thermal evaporator is discussed, which is a perfect fit for quench condensation of superconducting thin films. First of all, the micro evaporation sources are very small in size, which means that they consume much less power than conventional coil sources. This is crucial for cryogenic environments because eventually all the heat generated have to be dissipated into the helium cooling system, which doesn't favor excessive heat. On the other hand, this also helps to keep the fluctuation of the base temperature at a minimum, so that the deposition target stays at a lower temperature which is beneficial for quench condensation. Of course less heat usually means less atoms throughput. However by utilizing the pulse width modulation techniques and taking Hertz-Knudsen equation Equation 4.1 and Clausius-Clapeyron equation Equation 4.2 into consideration, one can make full use of the pulsed heat to emit more atoms per unit heat generated. This is made possible because of the fast thermal response of the source due to the serpentine heaters' miniature dimensions, while the conventional coil source usually experiences a huge lag when heated or cooled. Although micro sources usually have much less load than macroscopic ones thus they are not suitable for fabrication of thick structures, the regime we are interested in for superconducting thin film study is in the order of a few angstroms to a few tens of nanometers, which are within the capacity of the micro sources. Secondly, the MEMS approach has a more precise control over the deposition process. The pulse width modulation technique provides a way to precisely adjust the amount of atoms during each emission. As has been demonstrated in subsection 4.3.3, the smallest single evaporation measured so far is on the order of ten atoms per square micron for the surface atomic density. This means that even tiny thickness effect on superconductors can be easily measured. The accuracy and high precision of the source is ensured by the mass sensor. A mass sensor constantly monitors the thickness of the deposited thin film during the quench condensation and provides feedback to the control unit therefore the deposition rate and final thickness can be arbitrarily determined, with a much higher resolution than the conventional crystal thickness monitor. With the help of pulse actuation and high-resolution mass sensor, one can use many small pulses distributed within a very long period to grow the superconducting thin film much slower than what the conventional method can do. By doing so, each emission of atoms only contains very few atoms and the total thermal energy carried by them is low, meaning that the atoms will tend to stay fixed on the cold substrate and eventually form a disordered superconducting thin film, even without the help of a Ge sticking layer. We will show and discuss the experiment evidence later in this chapter. Last but not least, many transport experiments on superconducting films involve more than one element. this can be achieved by using the micro source array. By loading different areas of the source array with the aid of shadow masks, one can build a multi-element evaporator in a single chip. This enables the fabrication of nanoscale multi-layer or alloy thin films. By having an ultra-fast shutter similar to the one shown in subsection 2.2.3, the setup has the potential to even place single atom impurity on the deposited disordered film, where quantum effect may be observed (Woolf and Reif, 1965).

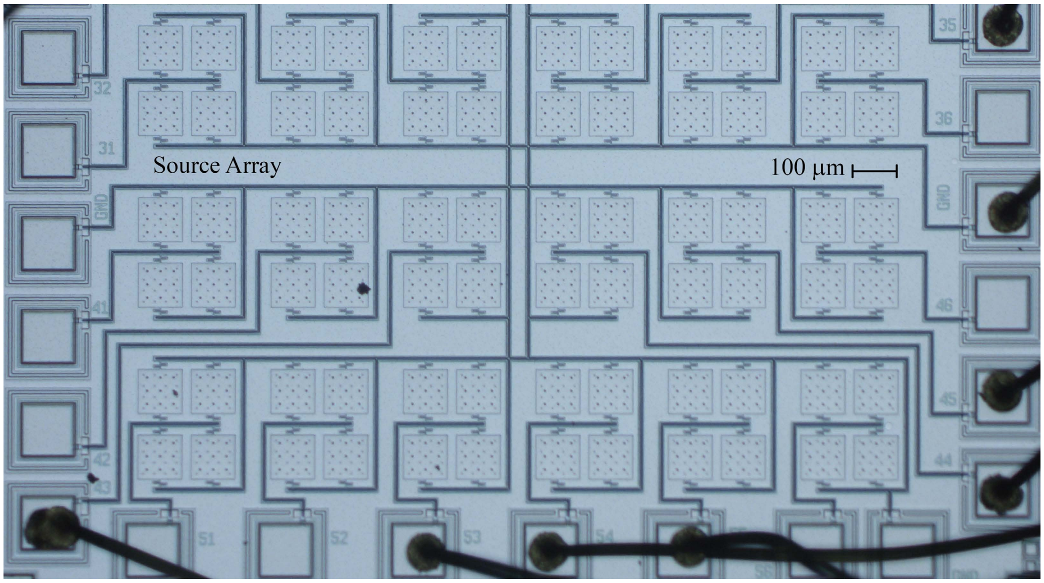

Figure 5·1: The optical microscopic image of the source array designed for superconducting thin film fabrication. Each source element has a dimension of 100 µm × 100 µm. The bonding pads are arranged along the edge of the die. 500 nm of Pb has been loaded onto the source array using a thermal evaporator.

Shown in Figure 5·1 is the micro evaporation source array specifically designed for the superconducting thin film deposition application. Unlike the sources discussed in chapter 4, these source plates made from POLY2 have a dimension of 100 µm × 100 µm. Just as the previous design, each of the source plate is also suspended by two serpentine springs as heaters. Four source elements are bundled into a 2×2 array as a source group, electrically in parallel. The entire 2.5 mm × 2.5 mm sub-die is tiled with 5 rows and 6 columns of the source group, making the total number of source plates 120 and the total available evaporation surface area 1.2 mm^2. Each source group has its own bonding pad and all bonding pads are arranged along the edge of the sub-die for the ease of making bonds and also to make the bonding wire not block the way of the emitted atoms. Wiring is properly done using gold coated POLY2 bridges to minimize the resistance along the wire so that most heat generation is concentrated on the spring heaters. All sources share the same electrical ground and when conducting the evaporation, all sources plates in use are actuated in parallel, which is important because sources are heated using voltage pulses. Hence for each pulse all sources have a same voltage applied across them and every individual source is independent from others. The advantage is that if one or some of the sources are burnt, the rest will not be affected and can still work normally. By adjusting the pulse voltage precisely, one can change the temperature of all source plates during the pulse thus the deposition rate, which is monitored by the mass sensor. Desired metal is loaded onto the sample using conventional e-beam or thermal evaporators. In principle for such a tightly tiled source die there is no room to integrate the bimorph-supported polysilicon shadow mask to keep the spring heaters clear from evaporants. This means that for some materials which require high evaporation temperature the source may fail due to the reaction occurs on the hot heaters. However, many material we are interested in, for example Pb, can be evaporated at an acceptable rate with a relatively low temperature that doesn't break the Al_2O_3 protection layer. Experiments also show that for Pb a shadow mask is not even needed to protect the bonding pad. It is presumed that metal loaded onto the entire source die surface may create a shortcut from pad to pad. This has been observed that the typical initial resistance of a source group loaded with 500 nm of Pb at a voltage of 0.1 V is a few Ω, indicating a short across the source. When the pulse voltage is increased to around 1 V, the resistance will abruptly shoot up to a few hundreds of Ω, and stay high even the voltage is lowered again. This is because that when the Pb film is shorting the current, a lot of heat is generated inside the Pb film, especially on the region above the springs where the film is the narrowest. The heat will first melt a small area of Pb locally on the spring and the surface tension will pull the molten Pb apart to break the circuit. At that time the Pb film is open so the current will have to flow along the polysilicon structure, bringing the source back to the normal working state. This is why the irreversible resistance shoot-up is observed. At the point when Pb melts, its vapor pressure is still very low, thus there is almost no Pb atoms evaporated off of the spring when the melting occurs. However, for some materials with high melting point, it will be very difficult to use this method to break the shorting circuit therefore a shadow mask may be desirable to keep the loaded material away from the bonding pads. Thanks to the Al_2O_3 protection layer, as long as the loaded material does not make direct contact to the gold bond ball, it will not short the source plate.

5.2.2 The quench condensation target

A target die based on the same PolyMUMPs process is used as the substrate for quench condensation of superconducting thin films. This provides several major advantages: 1) The native SiN layer is known to be a smooth and homogeneous passivated substrate, which is suitable for ultra-thin films to be deposited on; 2) The native gold and its smooth transition onto the SiN layer provides excellent electrical contact for resistivity measurement; 3) On-chip MEMS sensors including mass sensors or thermometers can be easily integrated to monitor the deposition process for enhanced precision and control; 4) Micro polysilicon structures and actuators can be used to better define the film geometry or enable multi-step fabrication to build complex superconducting 2D circuit. By making the target small and comparable to the source chip, one builds a micro thermal evaporation chamber which easily fits in a cryogenic environment.

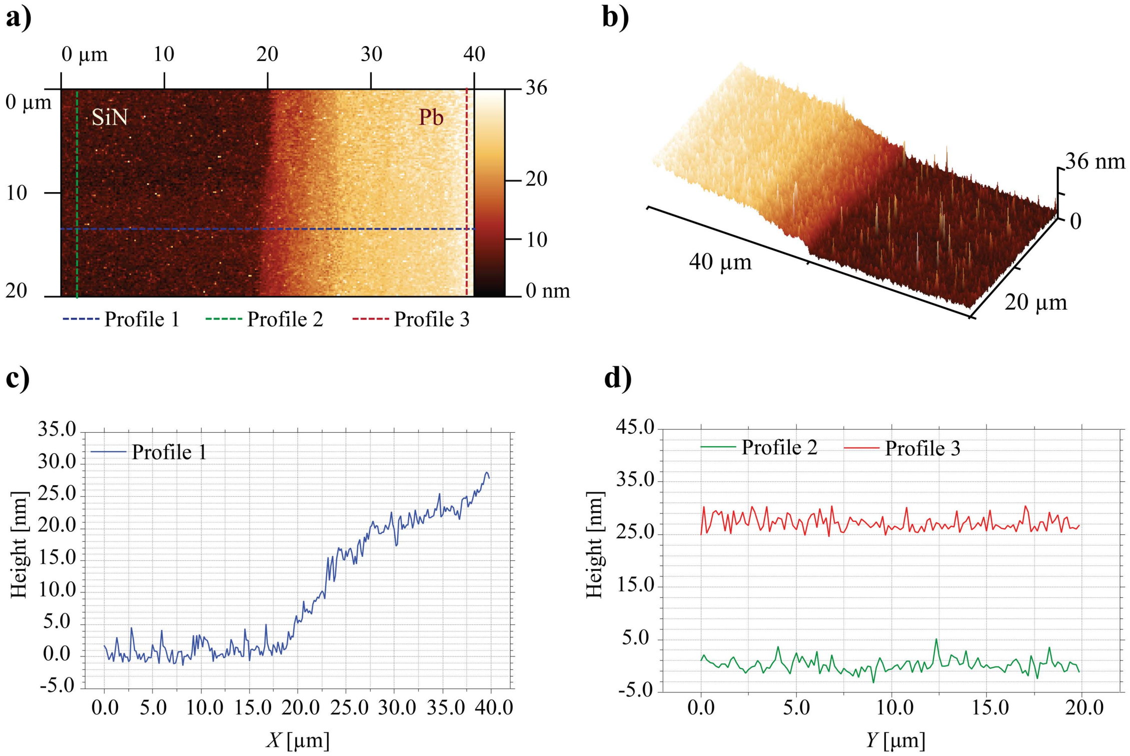

Figure 5·2: AFM measurement is carried out on the surface of the thinned nitride and quench condensed Pb film. A shadow mask is used to define an area for Pb quench condensation within the thinned nitride. The blurry edge between bare SiN and Pb film is the penumbra effect due to the finite size of the source array. a) A 2D colored topographic map of the sample along the edge of Pb deposition area. b) The corresponding 3D topographic map. c) and d) show the profile plot along the lines depicted in a).

The silicon nitride substrate

The native silicon nitride layer of PolyMUMPs process has a thickness of 600 nm, and is deposited by LPCVD (low pressure chemical vapor deposition) (Cowen et al., 2011). AFM and SEM measurements show that it has a much smoother surface than the polysilicon structure. By having the DIMPLE and P1_P2_VIA overlapped on top of the nitride substrate during the design time, the process opens an area on both OXIDE1 and OXIDE2 to expose the nitride for the final POLY2 etch and gold deposition. Experiments show that this method thins the nitride layer and makes it even more flat because of the RIE etching step acting on the nitride. The exposure of nitride also makes it possible to deposit the native gold directly on the nitride to make electrical contact to the film. The SiN layer morphology is studied using AFM, as shown in Figure 5·2. Pb was quench condensed on this sample using a shadow mask so that morphology study can be performed on both the SiN substrate and the Pb thin film. However, due to the fact that *in-situ* AFM is not possible for our configuration, the sample needs to be taken out of the cryostat thus the Pb film has been annealed to room temperature and exposed to air. Figure 5·2 d) shows the profile plot along the green dotted line in Figure 5·2 a) which is within the area of the bare nitride substrate. It can be seen that the upper limit of fluctuation of the surface height is within a few nanometers and the standard deviation of height along the profile line is $(1.2 \pm 0.1)\,\mathrm{nm}$, indicating a very smooth substrate. The actual surface roughness may be even better than what was measured, considering that the measurement only reveals the upper limit due to the limited resolution of the AFM probe.

Making contact to the superconducting thin film

Transport measurements are performed on the quench condensed thin films to investigate its properties and conduct other experiments. The most common measurement is the resistivity measurement which is done using four-terminal sensing. In order to get electrical access to the thin film, the native PolyMUMPs gold is deposited directly onto the SiN substrate, through the opening made by DIMPLE and P1_P2_VIA superposition. Shown in Figure 5·3 are SEM images of the gold electrodes deposited on the SiN substrate. While 500 nm total thickness of the gold and a thin adhesion layer is too thick for the superconducting film which may be only a few nanometers thick, a tapered transition from the thick gold to the substrate is observed. The tapered area is thin and at the very end of it there are many gold nano-particles, which significantly increase the contact area to the thin film. As we will see later when actual measurements are made, these fine structures enable us to make electrical connections to the superconducting thin films.

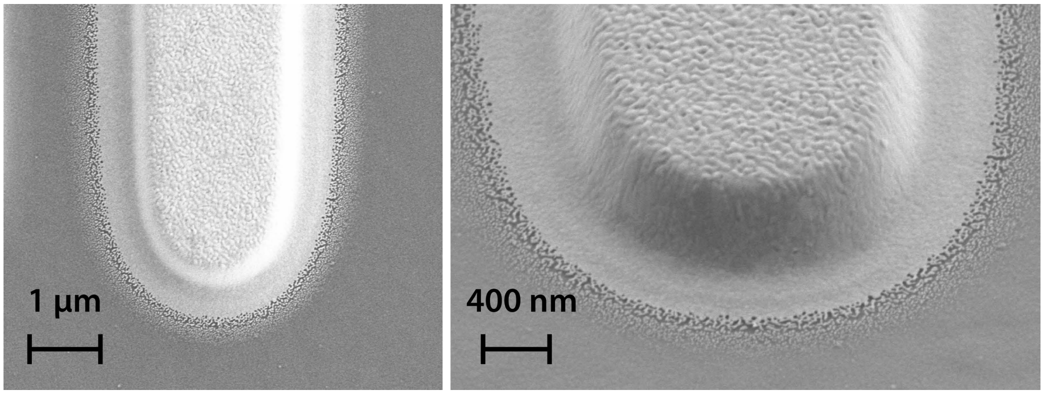

Figure 5·3: SEM images of the gold electrode on the thinned SiN substrate. There is a tapered transition from the gold to the substrate, providing electrical connections to superconducting thin films.

On-chip MEMS sensor and actuators

A major advantage of using MEMS to conduct deposition is that micro sensors and actuators can be used to better monitor and control the fabrication process. For superconducting thin films deposition, a high resolution *in-situ* measurement of the film thickness is usually required. Due to the size of a conventional crystal thickness monitor and the limited space inside a cryostat, using a conventional thickness monitor is not always feasible. Furthermore, the precision of the conventional thickness monitor is not adequate for thin film study, in which sub-monolayer resolution may be needed. As a comparison, the miniature MEMS mass sensor can be integrated onto the same chip and placed close to the target area, to achieve high resolution and less discrepancy. Other sensors like MEMS thermometers are also available and fully compatible with our MEMS target die. Micro structures or actuators are used to control the process and define the deposition geometry. MEMS shuttle plate can be used to conduct static stencil deposition, while a comb drive actuated plate might be used to perform dynamic stencil deposition, just like the Atomic Calligraphy described in chapter 2. With all the technologies discussed here, a typical design of the deposition target chip is shown in Figure 5·4. A mass sensor can be found on the left side of Figure 5·4 a), close to the four-terminal sensing structure. The four-terminal sensing is done through four gold electrodes with each connected to a gold contact pad for bonding. All gold structures are directly deposited on the thinned SiN substrate for continuity. POLY2 over-hanging wall is used to isolate electrodes so the current is flowing only through the central area where a shuttle plate will stay. The way it works is that during the design time a narrower ANCHOR2 line is placed along the center line of the POLY2 strip so that after release the side of the wall extrudes out of the support and is suspended in the mid-air. The cross section of the wall then has a T-shape. When the deposition material is evaporated from the source, it gets deposited on the target directionally and the over-hanging edge of the wall shadows the atomic flux and makes the film discontinuous. Therefore the current will not flow across the wall. The shuttle has a plate attached at the end and arbitrary shapes of opening can be planned during design time, or FIBed during post-processing. The opening defines the geometry of the resistivity measurement. Figure 5·4 a) and c) show that the shuttle is initially away from the central deposition area after release, while b) and d) show that by using a probe station the shuttle plate is guided into the right position that all four electrodes are inside the opening. Therefore the current can only flow through the deposited film inside the designated area without shorting, due to the POLY2 wall and the suspended arms of the shuttle. However, because of its nature, a static stencil is not capable to fabricate patterns with holes in it. In order to fabricate topologically more complex patterns, one can integrate the MEMS writer or a 1D shutter which can be actuated and positioned during the quench condensation to accomplish dynamic stencil fabrication.

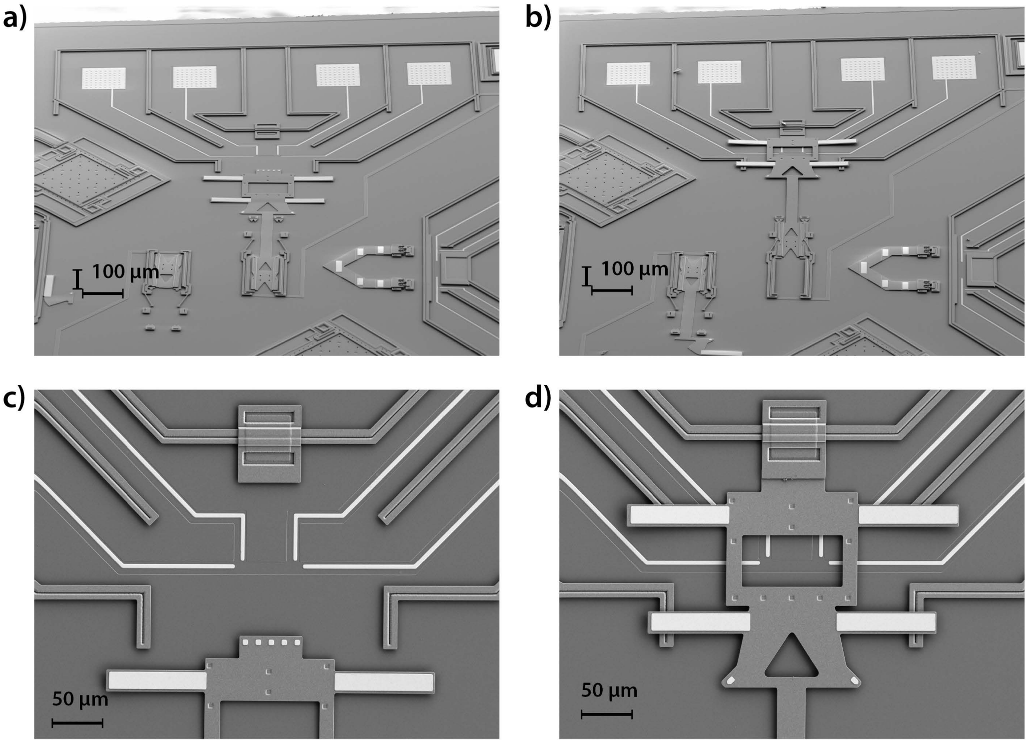

Figure 5·4: SEM images of the thin film deposition target die. The target features a mass sensor for thickness monitoring and a deposition area with four-terminal sensing capability. The shuttle structure is used to define the geometry of the measured thin film, to prevent shorting among gold electrodes wiring. After release, the shuttle is pushed in position using a probe station.

5.2.3 Building a Fab on a Chip for quench condensation

With the specifically designed source and target dies, one can build a Fab on a chip for superconducting thin film quench condensation studies. We use two pieces of leadless chip carrier (LCC) to package the source and the target, then combine them so that the target and source is facing each other with a small gap. Shown in Figure 5·5 is the cross section diagram of the setup. Both the source and target die are bonded onto a LCC package respectively. When placed together with a face to face configuration, the packages form a small chamber where emitted atoms from the source get deposited on the target directly within a short distance. This helps to make full use of the loaded material on the source. An opening on the target LCC package is etched so that a copper cylinder is inserted to make contact to the cold finger of a cryostat and the MEMS chip, providing excellent thermal conduction from the target chip to the cold finger. The cryostat is able to cool down the entire device to $\sim 2.8\,\mathrm{K}$. The temperature discrepancy between the target substrate and what is measured by the thermometer attached to the cold finger is then minimized. When the source is actuated, the generated heat may increase the temperature of the entire device. As discussed in subsection 4.3.3, thermal conduction is the main cause of a temperature spike on the target. However because the pulse actuation lowers the time-average power and the source die is cooled through the package to the cold finger which has a much larger thermal capacity, the actual temperature fluctuation on the target die can be controlled to less than $1\,\mathrm{K}$ while still maintaining a decent deposition rate for Pb. Vent holes were drilled on the source LCC package so that the air trapped inside the small chamber can get pumped out during the process. When the cryostat chamber is pumped to high vacuum, due to cryo-pumping, the space enclosed between LCC packages can reach even lower pressure, which further maximizes the mean free path of the emitted atoms from the source. Similar macroscopic version of this setup has been used for quench condensation previously (Frydman et al., 2002).

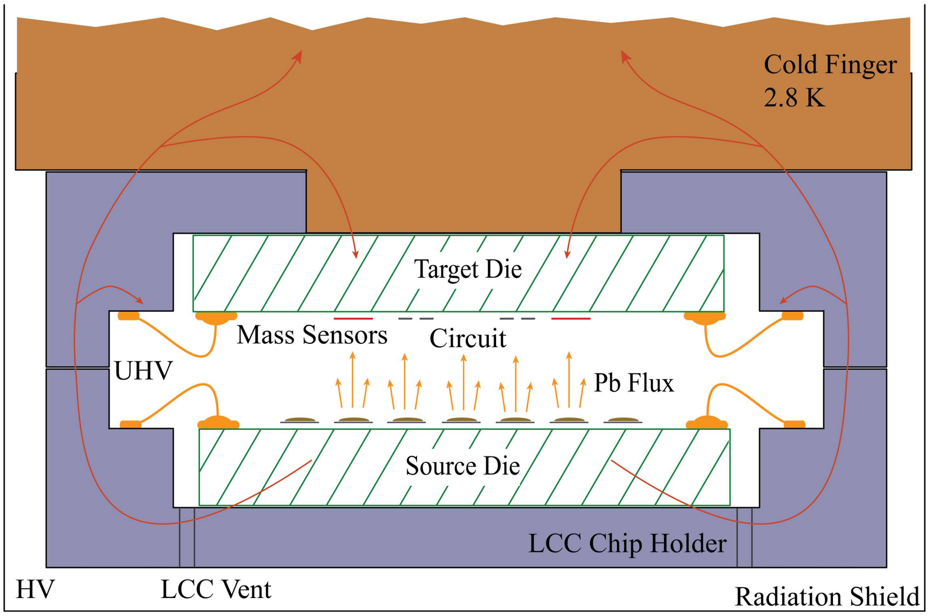

Figure 5·5: The packaging diagram for a Fab on a Chip micro evaporation chamber. The source and target chips are bonded onto two LCC packages and are glued together face to face. Atomic flux emitted from the source directly deposits on the target to fabricate the thin film. There is an opening on the LCC package substrate of the target so that the chip can make direct contact with a cold finger inside a cryostat to conduct quench condensation.

The diagram of the circuit used to measure the resistance of the thin film with four-terminal sensing is shown in Figure 5·6. The driving signal is a 33 Hz sine wave and is applied between two of the four electrodes with a 1 MΩ resistor in series. The main function of the 1 MΩ resistor is to limit the current. For example, when the applied voltage is 40 mV, the maximum current that is allowed through the thin film regardless of its resistance is 40 nA. This can protect the thin film since it is very fragile and may be burnt by a large current. Two lock-in amplifiers are used to make precise voltage measurements. Both of them are synced to the 33 Hz sine wave to pick up signal only in this frequency, eliminating noises with other frequencies. The

SR530 lock-in is used to measure the voltage across the 1 MΩ resistor, so that the current flowing through the thin film can be determined. The SR124 lock-in measures the voltages across the other two electrodes on the thin film. The resistance of the region between the two voltage electrodes can then be calculated from the voltage and current. All cables used are high-frequency coaxial cables to minimize interference. This setup works well when the contact resistance between the thin film and the gold electrode is small. But when the film is in insulating state or the contact resistance is comparable to the internal resistance (10 MΩ) of the lock-in amplifier, the measured resistance may not be accurate any more.

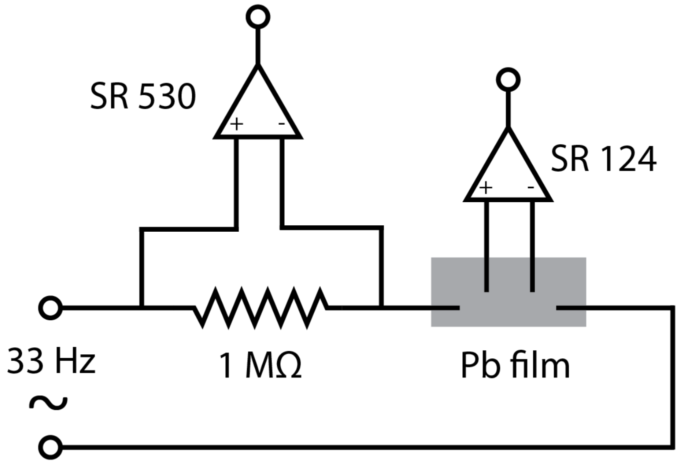

Figure 5·6: The circuit diagram of the four-terminal sensing resistivity measurement on the quench condensed Pb thin film.

5.3 Quench condensed Pb thin films

5.3.1 Superconducting transition temperature and film thickness

With the configuration described in section 5.2, we can conduct quench condensation experiments of Pb inside a cryostat and measure the superconducting properties for different thicknesses. Pb was deposited very slowly with an average rate of $\sim 3\,\mathrm{nm/h}$. To achieve that, each pulse lasts for 10 ms and two consecutive pulsed are 2 s apart. The mass sensor is then used to monitor the deposition rate. During the deposition process, the four-terminal sensing is disabled and all electrodes are grounded to the substrate so no current is flowing in the thin film, to minimize the possible effect of current on the morphology of the deposited film. After the desired thickness is achieved, the electrodes are ungrounded and four-terminal sensing is performed to measure the resistance of the thin film. Temperature is swept carefully with the precisely controlled cryostat while taking the resistance measurements. This process is then repeated on the same sample several times while keeping the temperature low to get measurements on the thin film with different thicknesses. By doing that one can get resistance data on the thin film for various thickness and temperature combinations with just one sample. Plotted in Figure 5·7 is the data of such a measurement. The conduction is first measured at 2 nm with a superconducting transition temperature (T_c) at around 4.8 K. With increasing thickness, a monotonically decreasing normal resistance and increasing T_c have been observed. At 10 nm, T_c has increased to around 6.7 K and the normal resistance has dropped below 3% of the normal resistance of a 2 nm film. The temperature was brought up to 10 K for each thickness and the resistance curves for temperature sweeping up and down overlap, indicating that no obvious annealing effect is observed within this temperature range. The superconducting transition is sharp that it is completed within a narrow temperature range, especially when the film is thicker.

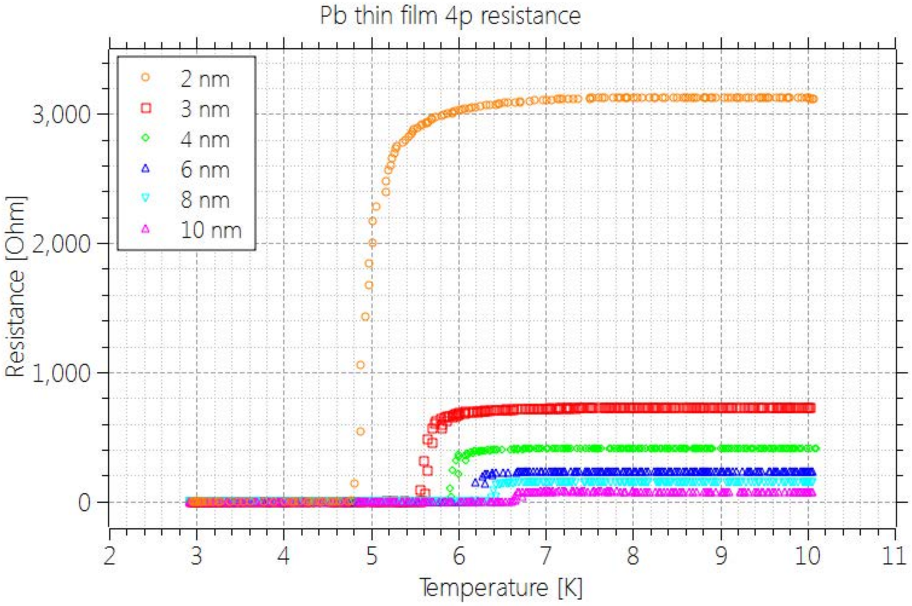

Figure 5·7: Four-terminal resistance measurements done with temperature sweep on the Pb quench condensed thin film for different thicknesses. Thinner films have a higher normal resistance and a lower superconducting transition temperature.

It has been argued that the substrate has a great effect on the morphology and thus superconducting properties of the thin film quench condensed using physical vapor deposition. When deposited on passivated substrates like SiO or SiN, Pb may tend to move around on the surface to form isolated islands first, until when islands are getting large enough to connect with each other to achieve superconducting percolation. In this situation, the thickness of each island can be thick while the averaged film thickness is still relatively thin. Large island may start to behave like bulk superconductor with $T_c = 7.2\,\mathrm{K}$. However, since electrons still need to tunnel among islands, the superconducting transition temperature of the entire film may not be well defined, resulting in a broad and gradual resistance drop during a temperature sweep, instead of a sharp transition. Moreover, the temperature at which the resistance starts to drop for different thicknesses is always around the bulk $T_c = 7.2\,\mathrm{K}$. Shown in Figure 5·8 is the figure reproduced from Frydman's paper (Frydman, 2003). The left plot is the resistance measurement during temperature sweep on different thicknesses of granular Pb thin films quench condensed on passivated substrates. The long tail of the superconducting transition for intermediate thickness is the effect of a not well defined T_c due to the granular film morphology. On the other hand, the right plot shows the same measurements done on a uniform Pb thin film. To achieve a uniform film, a Ge sticking layer is used, which can improve the homogeneity of the quench condensed film significantly (Haviland et al., 1989)(Logeeswaran et al., 2009). As can be seen in the plot, since the thickness of a uniform thin film is well defined, the superconducting transition temperature is well defined and is different for various thicknesses. The sharp transition indicates a disordered amorphous thin film.

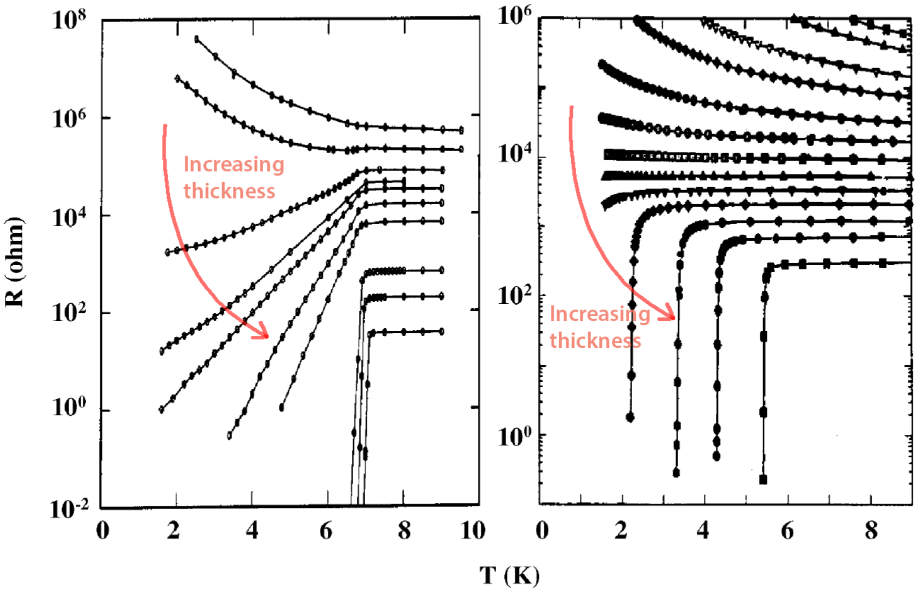

Figure 5·8: Reproduced from reference (Frydman, 2003). This figure shows the resistance versus temperature measurements done on various thicknesses of Pb thin films with two different deposition processes. The left plot corresponds to a granular film deposited on SiO substrate while the right one corresponds to uniform films evaporated on a Ge under-layer.

The positive correlation between T_c and film thickness for superconducting thin films has been well studied and is supported by theory. According to Bardeen-Cooper-Schrieffer (BCS) theory (Bardeen et al., 1957), the superconducting transition temperature is determined by

$$kT_c = 1.14\hbar\omega_D \exp(-\frac{1}{N(0)V}) \tag{5.1}$$

where k is the Boltzmann constant, ω_D is the Debye frequency, $N(0)$ is the electron density of states at the Fermi surface, and V is the attractive interaction. On the other hand, the energy gap can be express as

$$\Delta = \frac{\hbar\omega_D}{\sinh(\frac{1}{N(0)V})} \tag{5.2}$$

which means that there is a positive correlation between T_c and the energy gap. From a qualitative point of view, when the energy gap is larger, a higher temperature is required in order to excite electrons to destroy the superconductivity. For bulk material, T_c does not depend on the dimension of the sample, because a macroscopic dimension has no effect on the energy gap. However, the situation is quite different for thin films when the thickness is so small that the quantum effect becomes significant. The motion of the electron along the axis of the thickness will be quantized and can be modeled as confined in a quantum square well. While a simple model assumes infinite wall boundary conditions, a more realistic model allows for leakage of electronic wave function into a distance outside the film. In such a model, the relationship between energy gap and film thickness can be estimated by solving the quantum well state problem with the assumed boundary condition (Yu et al., 1976)

$$\Delta \cong 2\hbar\omega_D \exp(-\frac{1}{\rho(1 - Bb_\infty/a')}) \tag{5.3}$$

where ρ and B are constants, b_∞ is the allowed penetration depth and a' is the total film thickness including b_∞ on both sides. This result indicates a positive correlation between the energy gap and the film thickness, thus a positive correlation between T_c and the film thickness. By taking assumptions and approximations, it is shown that the relationship between T_c and the film thickness can be approximated as (Yu et al., 1976)

$$T_c = T_{c0} \exp(-\frac{C}{a}) \tag{5.4}$$

where $T_{c0} = 7.2\,\mathrm{K}$ is the superconducting transition temperature for bulk Pb, a is the film thickness and C is a positive constant yet to be determined by the experiment. The T_c versus film thickness plot using the same data set as Figure 5·7 is shown in Figure 5·9. In order to plot the theory prediction Equation 5.4 and compare it with the experiment result, Equation 5.4 is fitted to the experiment data to determine the constant T_{c0} and C. In this case, T_{c0} is determined to be $(7.10 \pm 0.07)\,\mathrm{K}$ and C is determined to be $(0.76 \pm 0.04)\,\mathrm{nm}$. Equation 5.4 is then plotted in Figure 5·9 as the red curve for comparison with the experiment data. It can be seen that the theory prediction and the experiment data match well. They show the similar trend of T_c as the film thickness increases. The fitted parameter T_{c0} has a value very close to the well measured 7.2 K superconducting transition temperature for bulk Pb. As has been discussed in (Yu et al., 1976), the constant C is correlated to the penetration depth of the wave function of the electron out of the material surface. This implies that the material of the substrate may have an effect on T_c for very thin superconducting films, especially when the substrate is metal. This proximity effect has been studied in previous research. (Cooper, 1961) (Lazar et al., 2000)

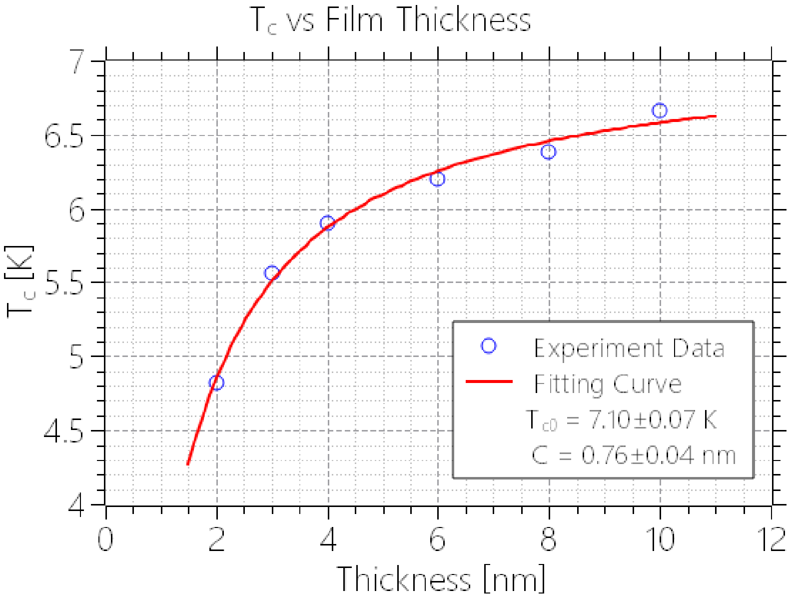

Figure 5·9: The T_c versus film thickness plot of the same data set with Figure 5·7. The red curve shows the theory prediction using Equation 5.4. The parameters T_{c0} and C in Equation 5.4 are determined by fitting the equation to the experiment data. The result shows that $T_{c0} = (7.10 \pm 0.07)\,\mathrm{K}$ which is very close to the well measured 7.2 K superconducting transition temperature for bulk Pb, and $C = (0.76 \pm 0.04)\,\mathrm{nm}$. It can be seen that the trend of T_c as the film thickness increases for the experiment data matches well with the theory.

A more careful theoretical calculation on the energy gap shows that an oscillation exists in the energy gap as the film thickness changes (Yu et al., 1976)(Paskin and Singh, 1965)(Orr et al., 1984)(Blatt and Thompson, 1963), which means that the oscillation should also exist in T_c. This effect has been observed in experiments (Orr et al., 1984)(Eom et al., 2006). Due to the high resolution and uniformity of the thin film quench condensed using Fab on a Chip, such an experiment should be achievable with our approach and could be a future research topic.

Similar granular film results have been reported by Ekinci (Ekinci and Valles, 1999), where different passivated substrates were used. In the research, it is reported that different substrate materials have little effect on the microscopic structure of the thin film and a granular film is always obtained. *In-situ* scanning tunneling microscopy (STM) measurements done on the sample confirm the morphology of the granular films. The T_c for different thicknesses were measured and the data is plotted in Figure 5·10. In Ekinci's data, there is a sudden drop of T_c when the film thickness is below $\sim 6\,\text{nm}$. For films thinner than that, the T_c is beyond the measurement limit. This phenomenon is explained by the finite size effect of the Pb grain. At around $\sim 6\,\text{nm}$, the second layer of Pb grains densely fills in the gaps among grains in the first layer, thus the superconductivity is suddenly boosted (Ekinci and Valles, 1999). The red dots overlaid on Figure 5·10 show the results of similar measurements done on the Pb thin film quench condensed using Fab on a Chip. It is clear that the grain size effect (if any) is much smaller.

The current result indicates that the Pb thin film deposited using the Fab on a Chip approach behaves very differently from the one deposited using the macroscopic counterpart. Comparing the plots in Figure 5·7 with Figure 5·8, it seems that the Pb thin film quench condensed using our micro evaporator is a uniform amorphous film. This implies that even for quench condensation done on passivated substrates, uniform Pb films are achievable. The key might be how the deposition is conducted. The major difference between our approach and the conventional quench condensation process is that by using the micro sources, one can puff off atoms at a slow rate that each pulse only deposits a few atoms per square microns on the substrate. During the entire deposition process, the substrate stays cold because of the low heat dissipation from the source. Even though Pb atoms tend to ball up, they will stay still because the over thermal energy is low. Due to the small amount, they are cooled by the giant substrate in a short time. As for the conventional deposition, the atomic flux

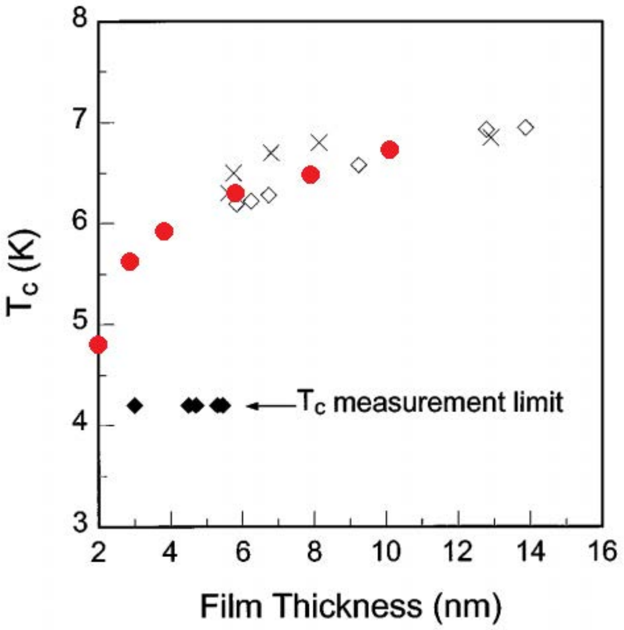

Figure 5·10: Reproduced from reference (Ekinci and Valles, 1999). This plot shows the T_c versus film thickness measurements for Pb thin films deposited on highly oriented pyrolytic graphite (HOPG) (diamonds) and GeO$_x$ (crosses). The red dots overlaid on top of the plot is the data obtained on Pb thin films quench condensed using Fab on a Chip.

is so high that too many atoms reach the substrate simultaneously thus balling up may happen. The amount of emitted atoms can not be precisely controlled in a conventional deposition process.

In order to confirm that the quench condensation using Fab on a Chip continuously adds atoms to the thin film, a resistance measurement is performed while the deposition is undergoing. To prepare for that, an initial 3 nm thick of Pb was deposited. Temperature sweep on this sample measures a well defined superconducting transition as shown in Figure 5·11. The temperature was then raised to 6 K, which is on the edge of superconducting transition. The resistance of the thin film at this temperature was around 4700 Ω. When new atoms are added to a thin film which is just on the transition at 6 K, the resistance will be very sensitive to the newly

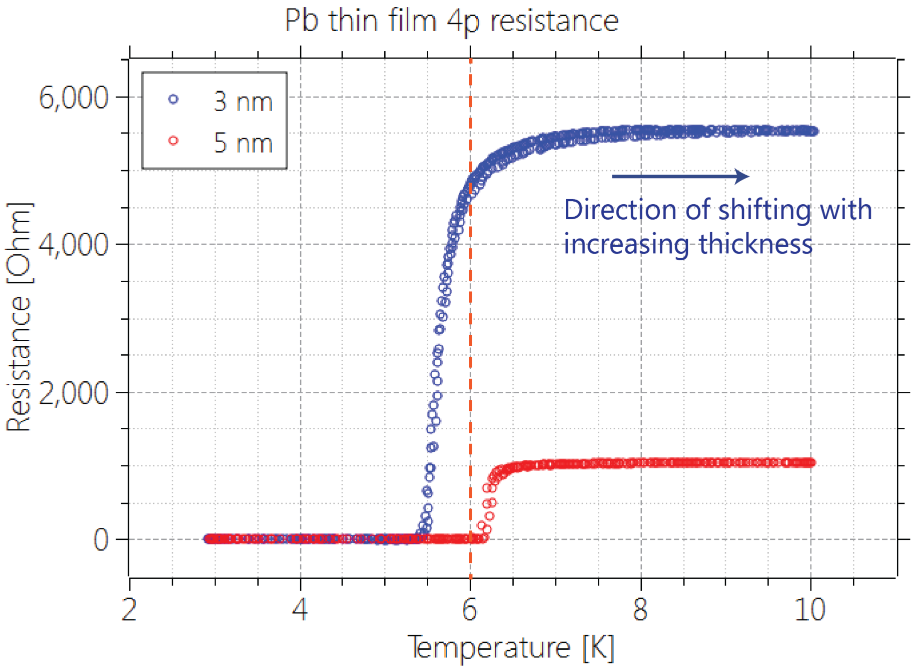

Figure 5·11: A Pb thin film of 3 nm has been quench condensed. The resistance measurement during a temperature sweep shows a well defined superconducting transition. After the quench deposition of another 2 nm at 6 K during which resistance measurement was constantly performed, the superconducting transition shifted to the right.

added atoms and even a tiny discontinuous behavior will have a great impact on the resistance curve thus can be observed. The four-terminal sensing was enabled for resistance measurement as the micro source array was being pulsed. The deposition process was performed slowly and each pulse emitted very few atoms that the quench condensation of additional ~ 2 nm thick of Pb took more than 3 hours at a constant rate. The resistance versus thickness curve is plotted in Figure 5·12. It can be seen that the resistance continuously decreases to zero as the thickness increases. This is because that each time when new atoms are deposited, the film becomes a little bit thicker, so that the normal resistance will decrease and the T_c will increase. The equivalent effect is that the resistance curve in Figure 5·11 will shrink and shift to the right. Eventually at $\sim$ 5 nm and 6 K, the film is completely superconducting.

Another temperature sweep at $\sim 5\,\mathrm{nm}$ as shown in Figure 5·11 further confirms that the superconducting transition still exist, but just moves to the other side of $x = 6\,\mathrm{K}$. This result provides another evidence that the quench condensed Pb thin film using micro sources is disordered and homogeneous, so that there is no abrupt resistance discontinuity on the curve.

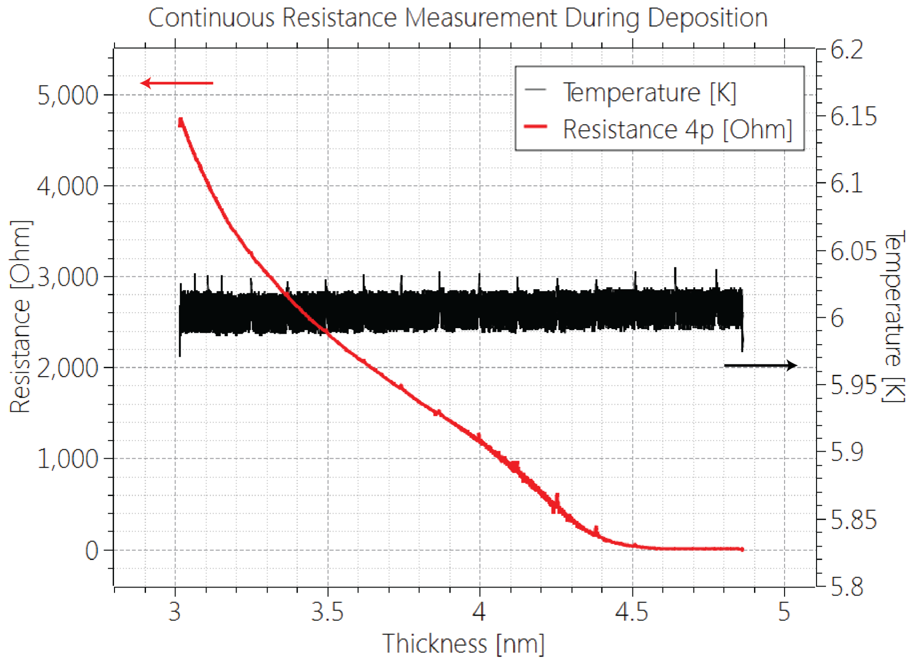

Figure 5·12: The resistance versus thickness curve for adding new Pb atoms using the micro sources to a $3\,\mathrm{nm}$ Pb thin film at $6\,\mathrm{K}$. The plotted substrate temperature is monitored by a thermal-couple thermometer attached to the end of the cold finger. There are periodic spikes in the resistance curve, due to the periodic temperature spikes as they always happen together.

Another effect can be seen on the resistance curve is that there are small periodic resistance spikes during the deposition. This phenomenon is believed to be caused by the temperature spikes of the substrate, due to the cryostat's liquid He pumping cycle. The cryostat is cooled by liquid He cycling inside a loop and a periodic pressure change exists due to the compressor. In order to explicitly show their correlation, the substrate temperature monitored by a thermal-couple thermometer attached to the end of the cold finger is also plotted in Figure 5·12. It is obvious that the periodic temperature spikes and the resistance spikes always emerge simultaneously. The resistance of the thin film on the superconducting transition is very sensitive to the temperature thus a small fluctuation of temperature can bring about a visible resistance fluctuation. The largest resistance spikes appear in the halfway when the thickness is between 3.5 nm and 4.5 nm. This is because that the maximum slope of resistance versus temperature curve appears in the halfway of the superconducting transition, as shown in Figure 5·11.

5.3.2 Annealing of the quenched condensed Pb thin film

The Pb thin film quench condensed at 3 K doesn't show obvious annealing effect up to 10 K, as shown in Figure 5·7, where the up sweep and down sweep curves match well. For higher temperatures, the annealing effect starts to emerge. Shown in Figure 5·13 are the temperature sweep measurements with increasing temperature sweep ranges of a $\sim$ 5 nm Pb thin film initially deposited at 3 K. The film was first brought to 15 K slowly and then back down to 3 K. The close up shown in Figure 5·14 indicates that the normal state resistance starts to decrease right past 10 K and the change is irreversible. The temperature was then cycled to 20 K, 25 K, 30 K, 42 K, and finally 75 K, in sequence. Each time when the film reached a not experienced higher temperature, the normal state resistance started to drop irreversibly. The exception is that a temperature minima occurs around 42 K. After that, the normal resistance even increases a bit with increasing temperature and the annealing effect becomes weak after that.

Comparing to the previous research done on mercury quench condensed thin films (Danilov et al., 1995), one possible explanation might be the existence of local insulat-

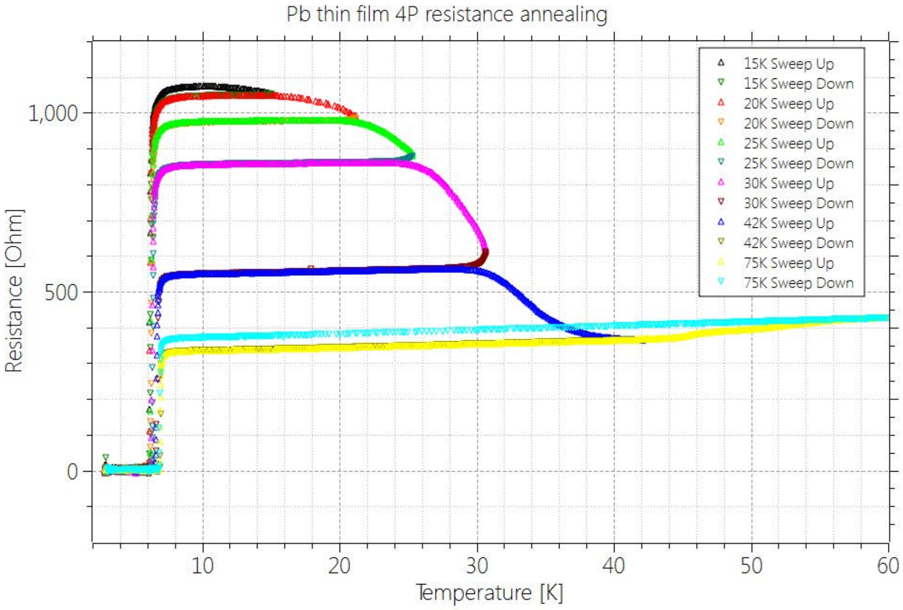

Figure 5·13: The annealing effect of a $\sim 5\,\mathrm{nm}$ Pb thin film initially deposited at 3 K. Each time the film reaches a new higher temperature, the normal state resistance undergoes an irreversible decrease, until over 60 K.

ing amorphous phase inside the Pb thin film. Such insulating phase may be confined in small regions surrounded by metallic lead and is metastable. When the temperature is raised, the additional thermal energy helps to overcome the energy barrier inside small insulating phase regions so the atoms inside the region will undergo a phase transition. Since for an amorphous film the insulating regions are disordered, the energy needed to overcome the barrier for different insulating regions may spread within a large range. This means that the transition of each region may take place at different temperatures thus the overall effect will be a gradual change of resistance. This explanation does not necessarily conflict with the previous assumption for the high uniformity of the Fab on a Chip quench condensed thin films, because even for these thin films the random thermal motion of deposited atoms still exists which can result in microscopic regions with different phases, especially when the film is thin.

After the annealing is completed at 75 K, the resistance of the film drops to around 1/3 of the normal state resistance before annealing, indicating that the ratio of insulating to metallic Pb in a newly quench condensed film is around 2:1. This means that the initial thermal energy of the film deposited at 3 K is sufficient to change one third of all deposited Pb into the metallic state. This proposes an interesting experiment that one can quench condense Pb at different base temperatures with varying rates, and use annealing to estimate the proportion of metallic Pb for each configuration, which can be easily conducted using Fab on a Chip. It is expected that higher base temperature or higher evaporation rate could result in a higher percentage of initial metallic Pb, but new physics could emerge as well.

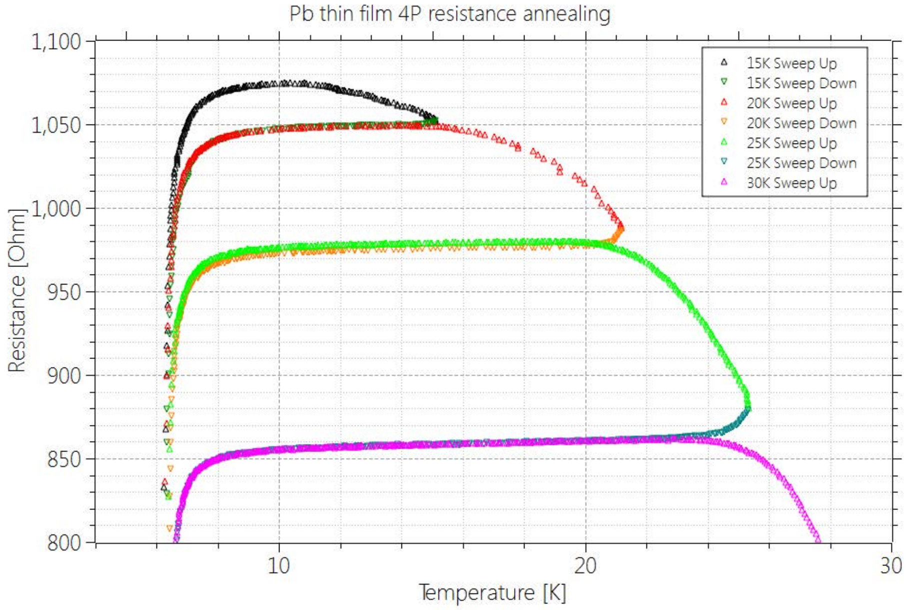

Figure 5·14: The close up shows that irreversible annealing starts right past 10 K.

A minima in the annealing data is observed around 42 K, before which the insulating to metallic phase transition occurs due to annealing. After the minima, insulating to metallic phase transition is completed and the normal state resistance increases slightly. Such a minima has been observed with other metals but usually found at higher temperatures, such as indium at 180 K (Ewert et al., 1976) or thin lead at a temperature between 200 K and 250 K (Granqvist and Claeson, 1974). In those films, the effect is explained by the transition from a disordered film to an ordered crystalline film, where the atoms inside the entire film rearrange to form crystalline structures. This process usually requires a much higher temperature thus the thermal energy to enable atom surface mobility. It is still a question why this happens at a much lower temperature for our quench condensed Pb thin films. Due to the lack of *in-situ* surface topology measurement, it is not clear whether the morphology of the film has changed during the annealing or any balling-up has occurred. The result shows that our film deposited using MEMS is very different from previously quench condensed thin films using conventional approaches. The close up around T_c shown in Figure 5·15 indicates that T_c has shifted from around 6.2 K to almost 7 K during the entire annealing process. This effect observed in a granular film was attributed to a thickness effect (Frydman, 2003), due to the morphology change of grains. In our cases, it is possible that when the insulating state transits into the metallic state, more charge carriers are gained so that it is equivalent to an increase of film thickness.

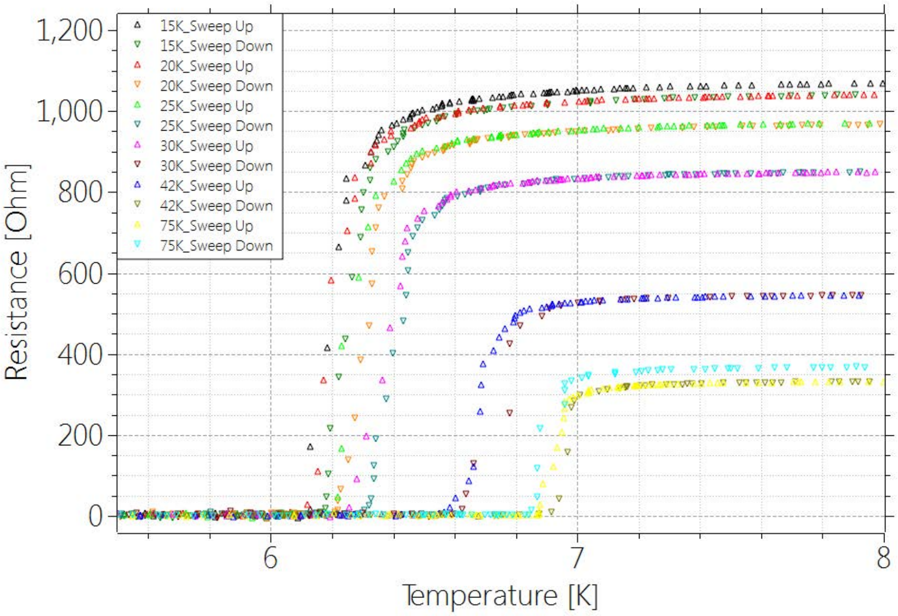

Figure 5·15: The close up around T_c shows that T_c has also shifted due to the annealing

Chapter 6

Conclusion

In this thesis, a novel approach to fabricate nanoscale structures using MEMS devices is discussed. MEMS being manufactured in a macroscopic fab inspires the idea of getting the process further down to fabricate even smaller structures, namely nanostructures, using MEMS. A collection of MEMS-based micron scale tools including lithography tools, novel atomic deposition sources, atomic mass sensors, thermometers, heaters, shutters and interconnect technologies has been developed. By integrating them into a single silicon chip, one build a micro system with the functionality of a semiconductor fab, namely Fab on a Chip. The manufacturing of the devices is based on a commercial MEMS foundry called PolyMUMPs, which is a reliable and reproducible surface micro-machining process.

The patterning tool is crucial for any fabrication systems. Here a microscopic XY stage with precise 2D positioning capability called the writer is utilized for nanostructure patterning. Arbitrary shapes of nanostructures are obtained by moving the writer plate in a pre-designed trace and depositing atoms through an aperture on the plate. Due to its dimensions and the fact that it is actuated using MEMS comb drives, the resolution of this technique can reach sub-nanometer level, while a relatively large working distance is still achievable. Complex patterns such as multi-layer and multi-material structures can be fabricated by having multiple apertures milled using FIB and conducting multiple evaporation runs on the same sample with the help of a ultra-fast shutter. The dynamic response of the writer has also been carefully characterized. A great flexibility is achieved by using the writer to perform nano-patterning.

In order to monitor the ongoing deposition process of Fab on a Chip, MEMS sensors are used. One of the most important MEMS sensors is the mass sensor which works just like a film thickness monitor. The MEMS mass sensor is essentially a parallel plate capacitor with one plate suspended by serpentine springs. Mass loaded on the suspended plate changes its oscillating frequency which can be precisely measured using a phase lock loop. The mass sensor is manufactured using the same semiconductor process as the writer so that it can be conveniently placed beside a writer for better accuracy. Its miniature size provides it a high mass resolution which is required for nanofabrication and even single atom placement.

The material source is an integral part of any fabrication systems. It is crucial that the source can emit precisely controlled atomic flux over a wide range during nanofabrication, so that one can either place a few atoms per square microns, or deposit a few nanometers of overall thickness. This is achieved by having a micro source plate which is suspended by spring heaters to conduct microscopic thermal evaporation. We have shown that due to its miniature dimensions, the source respond to the actuation within a millisecond. Its fast response enables the use of modulated voltage pulses to actuate the source, making it convenient to tune the deposited mass of each emission. It is shown that one can achieve eight orders of magnitude on deposited mass using the source array, indicating that this technology is sufficient for nanostructure fabrication as well as single atom impurity placement, which is of interest for many transport experiments.

One advantage of using MEMS to conduct fabrication is its scale. Being small means high resolution and low heat generation, which are required for experiments on quench condensed superconducting thin films. A target chip with thin film resistance measurement electrodes and mass sensors was manufactured using the PolyMUMPs foundry. By packaging the source and the target die together, a micro evaporation chamber is built to conduct thin film quench condensation and *in-situ* experiments. Measurements show that unlike previously quench condensed thin films using conventional macroscopic sources, the MEMS approach was able to deposit a uniform amorphous thin film on a passivated substrate. Ultra-low but measurable deposition rate due to the pulsed deposition may be the major reason of the homogeneous film. The thermal energy of each deposition step is well depressed therefore the morphology of the thin film is quite different from what conventional methods get.

Future research could focus on the combination of the source and the writer to gain even greater flexibility of nanofabrication. Hence one can precisely control when, where and how many atoms get deposited. Single atom deposition may also be possible given the high resolution of the source, the small FIBed aperture on the writer plate and the fast response of the integrated shutter. Topologically more complex nanoscale circuit could be fabricated in this way for experiments involving quantum effects. By having multiple material loaded on the source, one can conduct alloy thin films research or investigate the influence of impurities on supercondcutors. We show that by conducting nanofabrication in the micron scale, a new regime of nanoscale physics research is achieved.

References

Aksyuk, V., Balakirev, F. F., Boebinger, G. S., Gammel, P. L., Haddon, R. C., and Bishop, D. J. (1998). Micromechanical ”Trampoline” Magnetometers for Use in Large Pulsed Magnetic Fields. *Science*, 280(5364):720–722.

Allan, D. W. (2005). Statistics_of_Atomic_Frequency_Standards. *Proceedings of the IEEE*, 54(2):221 – 230.

Bardeen, J., Cooper, L. N., and Schrieffer, J. R. (1957). Theory of Superconductivity. *Physical Review*, 108(5):1175–1204.

Barnes, J. A. and Allan, D. W. (1990). Variances based on data with dead time between the measurements. *NIST Technical Note*, 1318:TN–296 – TN–335.

Baumert, E., Theillet, P.-O., and Pierron, O. (2011). Fatigue-resistant silicon films coated with nanoscale alumina layers. *Scripta Materialia*, 65(7):596–599.

Bell, D. J., Lu, T. J., Fleck, N. A., and Spearing, S. M. (2005). MEMS actuators and sensors: observations on their performance and selection for purpose. *Journal of Micromechanics and Microengineering*, 15(7):S153.

Bishop, D., Pardo, F., Bolle, C., Giles, R., and Aksyuk, V. (2012). Silicon Micro-Machines for Fun and Profit. *Journal of Low Temperature Physics*, 169(5-6):386–399.

Biswas, A., Bayer, I. S., Biris, A. S., Wang, T., Dervishi, E., and Faupel, F. (2012). Advances in top-down and bottom-up surface nanofabrication: Techniques, applications & future prospects. *Advances in Colloid and Interface Science*, 170(1-2):2–27.

Blatt, J. M. and Thompson, C. J. (1963). Shape Resonances in Superconducting Thin Films. *Physical Review Letters*, 10(8):332–334.

Bogue, R. (2007). MEMS sensors: past, present and future. *Sensor Review*, 27(1):7–13.

Champagne, A. R., Couture, A. J., Kuemmeth, F., and Ralph, D. C. (2003). Nanometer-scale scanning sensors fabricated using stencil lithography. *Applied Physics Letters*, 82(7):1111.

Chan, H. B., Aksyuk, V. a., Kleiman, R. N., Bishop, D. J., and Capasso, F. (2001). Nonlinear micromechanical Casimir oscillator. *Physical review letters*, 87(21):211801.

Chen, K. S. and Ou, K. S. (2007). Command-shaping techniques for electrostatic MEMS actuation: Analysis and simulation. *Journal of Microelectromechanical Systems*, 16(3):537–549.

Chou, S. Y. (1996). Nanoimprint lithography. *Journal of Vacuum Science & Technology B: Microelectronics and Nanometer Structures*, 14(6):4129.

Cooper, L. N. (1961). Superconductivity in the neighborhood of metallic contacts. *Physical Review Letters*, 6(12):689–690.

Cowen, A., Hardy, B., Mahadevan, R., and Wilcenski, S. (2011). *PolyMUMPs Design Handbook*. MEMSCAP Inc.

Danilov, A. V., Kubatkin, S. E., Landau, I. L., Parshin, I. A., and Rinderer, L. (1995). Insulating phase of mercury in thin quench-condensed films. *Physical Review B*, 51(8):5514–5517.

Desai, P. D. (1986). Thermodynamic Properties of Iron and Silicon. *Journal of Physical and Chemical Reference Data*, 15(3):967.

Deshmukh, M. M., Ralph, D. C., Thomas, M., and Silcox, J. (1999). Nanofabrication using a stencil mask. *Applied Physics Letters*, 75(11):1631.

Eaton, W. P. and Smith, J. H. (1997). Micromachined pressure sensors: review and recent developments. *Smart Materials and Structures*, 6:530–539.

Egger, S., Ilie, A., Fu, Y., Chongsathien, J., Kang, D.-J., and Welland, M. E. (2005). Dynamic shadow mask technique: a universal tool for nanoscience. *Nano letters*, 5(1):15–20.

Ekinci, K. L. and Valles, J. M. (1999). Morphology of Quench Condensed Pb Films near the Insulator to Metal Transition. *Physical Review Letters*, 82(7):1518–1521.

Eom, D., Qin, S., Chou, M. Y., and Shih, C. K. (2006). Persistent superconductivity in ultrathin Pb films: A scanning tunneling spectroscopy study. *Physical Review Letters*, 96(2):1–4.

Ewert, S., Comberg, A., and Wühl, H. (1976). Superconductivity of amorphous and disordered crystalline indium films. *Solid State Communications*, 18(7):923–925.

Fedder, G. K. (1994). *Simulation of Microelectromechanical Systems.* PhD thesis, Univeristy of California at Berkley.

Frost, A. A. and Kalkwarf, D. R. (1953). A Semi-Empirical Equation for the Vapor Pressure of Liquids as a Function of Temperature. *The Journal of Chemical Physics*, 21(1953):264.

Frydman, A. (2003). The superconductor insulator transition in systems of ultrasmall grains. *Physica C: Superconductivity*, 391(2):189–195.

Frydman, A. and Dynes, R. C. (2001). Granular superconductors and ferromagnets: a proximity-effect-based analogue. *Philosophical Magazine B-Physics of Condensed Matter Statistical Mechanics Electronic Optical and Magnetic Properties*, 81(9):1153–1165.

Frydman, A., Naaman, O., and Dynes, R. C. (2002). Universal transport in 2D granular superconductors. *Physical Review B*, 66(5):052509.

Gardener, J. A. and Golovchenko, J. A. (2012). Ice-assisted electron beam lithography of graphene. *Nanotechnology*, 23(18):185302.

Geisberger, A., Sarkar, N., Ellis, M., and Skidmore, G. (2003). Electrothermal properties and modeling of polysilicon microthermal actuators. *Journal of Microelectromechanical Systems*, 12(4):513–523.

Gorman, J. J., Kim, Y.-S., Vladár, A. E., and Dagalakis, N. G. (2007). Design of an on-chip microscale nanoassembly system. *International Journal of Nanomanufacturing*, 1(6):710–721.

Grabiec, P., Domański, K., Janus, P., Zaborowski, M., and Jaroszewicz, B. (2005). Microsystem technology as a road from macro to nanoworld. *Bioelectrochemistry*, 66(1-2):23–28.

Granqvist, C. G. and Claeson, T. (1974). Superconductivity in ultrathin films II. Structure in tunneling curves. *Physics of Condensed Matter*, 18(2):99–120.

Grigorescu, a. E. and Hagen, C. W. (2009). Resists for sub-20-nm electron beam lithography with a focus on HSQ: state of the art. *Nanotechnology*, 20(29):292001.

Groner, M. D., Elam, J. W., Fabreguette, F. H., & George, S. M. (2002). Electrical characterization of thin Al2O3 films grown by atomic layer deposition on silicon and various metal substrates. *Thin Solid Films*, 413(1):186–197.

Guha, S., Gusev, E. P., Okorn-Schmidt, H., Copel, M., Ragnarsson, L.-Å., Bojarczuk, N. A., and Ronsheim, P. (2002). High temperature stability of Al[sub 2]O[sub 3] dielectrics on Si: Interfacial metal diffusion and mobility degradation. *Applied Physics Letters*, 81(16):2956.

Han, A., Vlassarev, D., Wang, J., Golovchenko, J. A., and Branton, D. (2010). Ice lithography for nanodevices. *Nano Letters*, 10(12):5056–5059.

Han, H., Imboden, M., Stark, T., del Corro, P. G., Pardo, F., Bolle, C. a., Lally, R. W., and Bishop, D. J. (2015). Programmable solid state atom sources for nanofabrication. *Nanoscale*, 7(24):10735–10744.

Haviland, D., Liu, Y., and Goldman, A. (1989). Onset of superconductivity in the two-dimensional limit. *Physical Review Letters*, 62(18):2180–2183.

He, J. and Ma, E. (2001). Nanoscale phase separation and local icosahedral order in amorphous alloys of immiscible elements. *Physical Review B*, 64(14):144206.

Hołyst, R. and Litniewski, M. (2009). Evaporation into vacuum: Mass flux from momentum flux and the Hertz-Knudsen relation revisited. *The Journal of chemical physics*, 130(7):074707.

Hung, P.-C. and Voloshin, A. S. (2003). In-plane strain measurement by digital image correlation. *Journal of the Brazilian Society of Mechanical Sciences and Engineering*, 25(3):215–221.

Imboden, M., Han, H., Chang, J., Pardo, F., Bolle, C. a., Lowell, E., and Bishop, D. J. (2013). Atomic calligraphy: the direct writing of nanoscale structures using a microelectromechanical system. *Nano letters*, 13(7):3379–84.

Imboden, M., Han, H., Stark, T., Lowell, E., Chang, J., Pardo, F., Bolle, C., del Corro, P. G., and Bishop, D. J. (2014a). Building a Fab on a Chip. *Nanoscale*, 6(10):5049–62.

Imboden, M., Morrison, J., Lowell, E., Han, H., and Bishop, D. J. (2014b). Controlling Levitation and Enhancing Displacement in Electrostatic Comb Drives of MEMS Actuators. *Journal of Microelectromechanical Systems*, 23(5):1063–1072.

Ismail, A. K., Burdess, J. S., Harris, A. J., Suarez, G., Keegan, N., Spoors, J. A., Chang, S. C., McNeil, C. J., and Hedley, J. (2008). The fabrication, characterization and testing of a MEMS circular diaphragm mass sensor. *Journal of Micromechanics and Microengineering*, 18(2):025021.

Ito, T. and Okazaki, S. (2000). Pushing the limits of lithography. *Nature*, 406(August):1027–1031.

Jensen, K., Kim, K., and Zettl, a. (2008). An atomic-resolution nanomechanical mass sensor. *Nature nanotechnology*, 3(9):533–7.

Ji, L., Zhu, Y., Moheimani, S. O. R., and Yuce, M. R. (2010). A micromachined 2DOF nanopositioner with integrated capacitive displacement sensor. In *Proceedings of IEEE Sensors*, pages 1464–1467.

Judy, J. W. (2001). Microelectromechanical systems (MEMS): fabrication, design and applications. *Smart Materials and Structures*, 10(1):1115–1134.

Kamins, T. I., Laderman, S. S., Coulman, D. J., & Turner, J. E. (1986). Interaction Between CVD Tungsten Films and Silicon during Annealing. *Journal of The Electrochemical Society*, 133(7):1438–1442.

Kim, B., Candler, R. N., Hopcroft, M. a., Agarwal, M., Park, W.-T., and Kenny, T. W. (2007). Frequency stability of wafer-scale film encapsulated silicon based MEMS resonators. *Sensors and Actuators A: Physical*, 136(1):125–131.

Laconte, J., Dupont, C., Flandre, D., and Raskin, J. P. (2004). SOI CMOS compatible low-power microheater optimization for the fabrication of smart gas sensors. *IEEE Sensors Journal*, 4(5):670–680.

Lakdawala, H. and Fedder, G. K. (2004). Temperature stabilization of CMOS capacitive accelerometers. *Journal of Micromechanics and Microengineering*, 14(4):559–566.

Lazar, L., Westerholt, K., Zabel, H., Tagirov, L., Goryunov, Y., Garif'yanov, N., and Garifullin, I. (2000). Superconductor/ferromagnet proximity effect in Fe/Pb/Fe trilayers. *Physical Review B*, 61(5):3711–3722.

Lee, J., Chunara, R., Shen, W., Payer, K., Babcock, K., Burg, T. P., and Manalis, S. R. (2011). Suspended microchannel resonators with piezoresistive sensors. *Lab on a chip*, 11(4):645–651.

Leland, R. (2005). Mechanical-thermal noise in MEMS gyroscopes. *IEEE Sensors Journal*, 5(3):493–500.

Liddle, J. A. and Gallatin, G. M. (2011). Lithography, metrology and nanomanufacturing. *Nanoscale*, 3(7):2679–88.

Liu, K., Avouris, P., Bucchignano, J., Martel, R., Sun, S., and Michl, J. (2002). Simple fabrication scheme for sub-10 nm electrode gaps using electron-beam lithography. *Applied Physics Letters*, 80(5):865–867.

Liu, X., Kim, K., and Sun, Y. (2007). A MEMS stage for 3-axis nanopositioning. *Journal of Micromechanics and Microengineering*, 17(9):1796–1802.

Logeeswaran, V. J., Kobayashi, N. P., Islam, M. S., Wu, W., Chaturvedi, P., Fang, N. X., Wang, S. Y., and Williams, R. S. (2009). Ultrasmooth silver thin films deposited with a germanium nucleation layer. *Nano Letters*, 9(1):178–182.

Lu, C., Lemkin, M., and Boser, B. E. (1995). Monolithic surface micromachined accelerometer with digital output. *IEEE Journal of Solid-State Circuits*, 30(12):1367–1373.

Maithripala, D. H. S., Berg, J. M., and Dayawansa, W. P. (2005). Control of an electrostatic microelectromechanical system using static and dynamic output feedback. *Journal of Dynamic Systems Measurement and Control-Transactions of the Asme*, 127(September 2005):443–450.

Mastrangelo, C. H., Yeh, J.-J., and Muller, R. S. (1992). Electrical and optical characteristics of vacuum-sealed polysilicon microlamps. *Electron Devices, IEEE Transactions*, 39(6):1363–1375.

McConnell, A., Uma, S., and Goodson, K. (2001). Thermal conductivity of doped polysilicon layers. *Journal of Microelectromechanical Systems*, 10(3):360–369.

MEMSCAP. PolyMUMPs Run Data.

Meyer, R., Hamann, S., Ehmann, M., König, D., Thienhaus, S., Savan, A., and Ludwig, A. (2011). Small-Scale Deposition of Thin Films and Nanoparticles by Microevaporation Sources. *Journal of Microelectromechanical Systems*, 20(1):21–27.

Miller, D. C., Foster, R. R., Jen, S.-H., Bertrand, J. a., Cunningham, S. J., Morris, A. S., Lee, Y.-C., George, S. M., and Dunn, M. L. (2010). Thermo-mechanical properties of alumina films created using the atomic layer deposition technique. *Sensors and Actuators A: Physical*, 164(1-2):58–67.

Moore, G. E. (1995). Lithography and the Future of Moore's Law. *SPIE's 1995 Symposium on Microlithography*, 2440:2–17.

Morrison, J., Imboden, M., Little, T. D., and Bishop, D. J. (2015). Electrothermally actuated tip-tilt-piston micromirror with integrated varifocal capability. *Optics Express*, 23(7):9555.

Nadal-Guardia, R., Dehé, A., Aigner, R., and Castañer, L. M. (2002). Current drive methods to extend the range of travel of electrostatic microactuators beyond the voltage pull-in point. *Journal of Microelectromechanical Systems*, 11(3):255–263.

Okada, Y. and Tokumaru, Y. (1984). Precise determination of lattice parameter and thermal expansion coefficient of silicon between 300 and 1500 K. *Journal of Applied Physics*, 56(2):314.

Okamoto, H. and Massalski, T. B. (1983). The AuSi (Gold-Silicon) system. *Bulletin of Alloy Phase Diagrams*, 4(2):190–198.

Orr, B. G., Jaeger, H. M., and Goldman, A. M. (1984). Transition-temperature oscillations in thin superconducting films. *Physical Review Letters*, 53(21):2046–2049.

Paskin, A. and Singh, A. D. (1965). Boundary Conditions and Quantum Effects in Thin Superconducting Films. *Physical Review*, 140(6A):A1965–A1967.

Piner, R. D., Zhu, J., Xu, F., and Hong, S. (1999). Dip-Pen Nanolithography. *Science*, 283(January):661–664.

Poran, S., Molina-Ruiz, M., Gérardin, A., Frydman, A., and Bourgeois, O. (2014). Specific heat measurement set-up for quench condensed thin superconducting films. *The Review of Scientific Instruments*, 85(5):053903.

Puretzky, A., Geohegan, D., Jesse, S., Ivanov, I., and Eres, G. (2005). In situ measurements and modeling of carbon nanotube array growth kinetics during chemical vapor deposition. *Applied Physics A*, 81(2):223–240.

Racz, Z., He, J., Srinivasan, S., Zhao, W., Seabaugh, A., Han, K., Ruchhoeft, P., and Wolfe, J. (2004). Nanofabrication using nanotranslated stencil masks and lift off. *Journal of Vacuum Science & Technology B: Microelectronics and Nanometer Structures*, 22(1):74.

Savu, V., Xie, S., and Brugger, J. (2011). 100 Mm Dynamic Stencils Pattern Sub-Micrometre Structures. *Nanoscale*, 3(7):2739–42.

Schmitt, J., Decher, G., Dressick, W. J., Brandow, S. L., Geer, R. E., Shashidhar, R., and Calvert, J. M. (1997). Metal nanoparticle/polymer superlattice films: Fabrication and control of layer structure. *Advanced Materials*, 9(1):61–65.

Strongin, M., Thompson, R. S., Kammerer, O. F., and Crow, J. E. (1970). Destruction of Superconductivity in Disordered Near-Monolayer Films. *Physical Review B*, 1(3):1078–1091.

Sun, L., Wang, J., Rong, W., Li, X., and Bao, H. (2008). A Silicon Integrated Micro Nano-Positioning XY-Stage for Nano-manipulation. *Journal of Micromechanics and Microengineering*, 18(12):125004(1–9).

Sundaramurthy, A., Schuck, P. J., Conley, N. R., Fromm, D. P., Kino, G. S., and Moerner, W. E. (2006). Toward nanometer-scale optical photolithography: Utilizing the near-field of bowtie optical nanoantennas. *Nano Letters*, 6(3):355–360.

Tanaka, M. (2007). An industrial and applied review of new MEMS devices features. *Microelectronic Engineering*, 84(5-8):1341–1344.

Tang, W. C., Lim, M. G., and Howe, R. T. (1992). Electrostatic Comb Drive Levitation and Control Method. *Journal of Microelectromechanical Systems*, 1(4):170–178.

Tanner, D. M. (2009). MEMS reliability: Where are we now? *Microelectronics Reliability*, 49(9-11):937–940.

Thompson, M. J., Li, M., and Horsley, D. A. (2011). Low power 3-axis lorentz force navigation magnetometer. *Proceedings of the IEEE International Conference on Micro Electro Mechanical Systems (MEMS)*, (3):593–596.

Vazquez-Mena, O., Gross, L., Xie, S., Villanueva, L., and Brugger, J. (2014). Resistless nanofabrication by stencil lithography: A review. *Microelectronic Engineering*, 132:236–254.

Villarroya, M., Verd, J., Teva, J., Abadal, G., Forsen, E., Murano, F. P., Uranga, A., Figueras, E., Montserrat, J., Esteve, J., Boisen, A., and Barniol, N. (2006). System on chip mass sensor based on polysilicon cantilevers arrays for multiple detection. *Sensors and Actuators A: Physical*, 132(1):154–164.

Waggoner, P. S. and Craighead, H. G. (2007). Micro- and nanomechanical sensors for environmental, chemical, and biological detection. *Lab on a chip*, 7(10):1238–55.

Watt, F., Bettiol, A. A., Van Kan, J. A., Teo, E. J., and Breese, M. B. H. (2005). Ion Beam Lithography And Nanofabrication: A Review. *International Journal of Nanoscience*, 04(03):269–286.

Woolf, A. E. and Reif, F. (1965). Effect of Magnetic Impurities on the Density of States of Superconductors. *Physical Review*, 137(2A):A557.

Xia, Y., Rogers, J. A., Paul, K. E., and Whitesides, G. M. (1999). Unconventional Methods for Fabricating and Patterning Nanostructures. *Chemical Reviews*, 99.7:1823–1848.

Yao, N. (2007). *Focused ion beam systems: basics and applications*. Cambridge University Press.

Yu, M., Strongin, M., and Paskin, A. (1976). Consistent calculation of boundary effects in thin superconducting films. *Physical Review B*, 14(3):996–1001.

Zhang, H., Chung, S.-w., and Mirkin, C. A. (2003). Fabrication of Sub-50-nm Solid-State Nanostructures on the Basis of Dip-Pen Nanolithography. *Nano Letters*, 3(1):43–45.

Zhang, L., Jiang, H. C., Liu, C., Dong, J. W., and Chow, P. (2007). Annealing of Al 2 O 3 thin films prepared by atomic layer deposition. *Journal of Physics D: Applied Physics*, 40(12):3707–3713.

CURRICULUM VITAE

Han Han

Contact `hh@bu.edu`

Department of Physics
Boston University
590 Commonwealth Avenue
Boston, MA 02215, USA

Education **Boston University** PhD candidate, September 2010 – present.

Thesis advisor: David Bishop.

Zhejiang University, B.S., Pyhsics , September 2006 – June 2010.

Selected Publications

1. Han, H., Imboden, M., Stark, T., del Corro, P. G., Pardo, F., Bolle, C., ... & Bishop, D. J. (2015). Programmable Solid State Atom Sources for Nanofabrication. *Nanoscale*, 7, 10735-10744
2. Imboden, M., Han, H., Stark, T., Lowell, E., Chang, J., Pardo, F., ... & Bishop, D. J. (2014). Building a Fab on a Chip. *Nanoscale*, 6(10), 5049-5062.
3. Imboden, M., Han, H., Chang, J., Pardo, F., Bolle, C. A., Lowell, E., & Bishop, D. J. Atomic Calligraphy: The Direct Writing of Nanoscale Structures using MEMS. *Nano Letters*, 2013, 13 (7), pp 3379-3384.
4. Luo, Y., Han, H., Tan, H., Lin, X., Li, Y., Jiang, S. ... & Li, S. CeNiAsO: An Antiferromagnetic Dense Kondo Lattice. *Journal of Physics: Condensed Matter*, 23(17), 175701.

Selected Talks

1. Han, H., Imboden, M., Del Corro, P., Stark, T., Lally, R., Pardo, F., Bolle, C. A. & Bishop, D. J. Digitally Programmable Micro Evaporation Source for Nanofabrication. *APS March Meeting 2015.* San Antonio, TX. March. 5, 2015
2. Han, H., Imboden, M., Stark, T., & Bishop, D. J. Integrated MEMS mass sensor and atom source for a "Fab on a Chip". *APS March Meeting 2014.* Denver, CO. March. 4, 2014
3. Han, H., Imboden, M., Chang, J., Pardo, F., Bolle, C. A., Lowell, E., & Bishop, D. J. Direct Fabrication of Nanoscale Structures Using MEMS. *2013 MRS Fall Meeting & Exhibit.* Boston, MA. Dec. 4, 2013